Preparation of Titania-based Composites with Controlled Electronic Structures

電子構造を制御したチタニア系複合体の調製

July, 2017

Kanji SAITO

齊藤　寛治

Preparation of Titania-based Composites with Controlled Electronic Structures

電子構造を制御したチタニア系複合体の調製

July, 2017

Waseda University
Graduate School of Creative Science and Engineering
Department of Earth Sciences,
Resources and Environmental Engineering,
Research on Physics and Chemistry of Minerals

Kanji SAITO

齊藤　寬治

CONTENTS

CHAPTER 4.

Room-temperature Rutile TiO$_2$ Nanoparticle Formation on Protonated Layered Titanate for High-performance Heterojunction Creation 69

CHAPTER 5.
Conclusions 99

CHAPTER 1

Introduction

1. Introduction

1.1 Heteroelemental Doping of TiO$_2$ for Visible-light Absorption

1.1.1 Overview of This Section

This section begins with a brief review of heteroelemental doping of silicon semiconductors for enhanced electrical conductivity, after which control of the light-absorption properties of TiO$_2$ by heteroelemental doping is introduced.

1.1.2 Heteroelemental Doping of Silicon Semiconductors

A schematic representation of the electronic structure of a semiconductor is shown in Figure 1-1. The lower band, which is filled with electrons, is called the valence band, and the upper band without electrons is called the conduction band. The energy gap between the top of the valence band (E_v) and the bottom of the conduction band (E_c) is called a band gap (E_g). Semiconductors do not allow currents to flow without thermal energy, since no mobile charge carriers are present in the energy bands. When thermal energy greater than the band gap is input, however, electrons are excited to the conduction band from the valence band, leaving holes in the valence band (so-called "charge separations"), and these acquire mobility that contributes to electrical conductivity.[1-3]
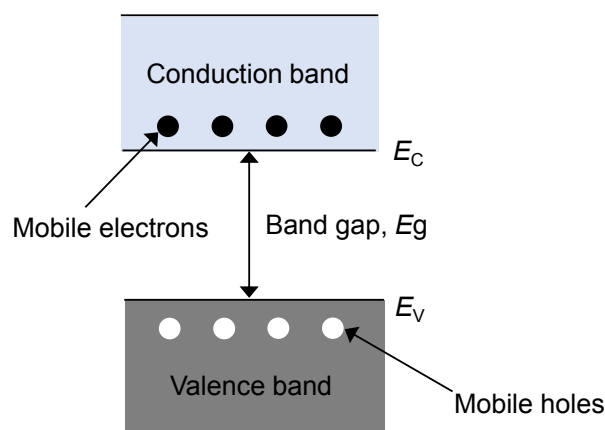
Figure 1-1. Schematic representation of the electronic structure of a semiconductor.

It is known that the electrical conductivity of semiconductors is considerably enhanced by substitutional doping of the semiconductor lattice with carefully chosen impurities, or in other words, heteroelemental doping. The doping of silicon with phosphorous or aluminium is a good example for explaining the mechanism of heteroelemental doping-enhanced electrical conductivity of semiconductors.

Upon formation of four covalent single bonds by a silicon atom, four sp^3 hybrid orbitals are created using their four valence electrons (3s^2, 3p^2), leading to production of tetrahedral structures. In the case of phosphorous doping, the valence electrons of phosphorous are 3s^2, 3p^3, and since only four of these electrons (3s^2, 3p^2) are involved in the creation of sp^3 hybrid orbitals, it can be assumed that the one extra electron is electrostatically associated with the excess positive inner charge of phosphorous (Figure 1-2A, left). The enhanced electrical conductivity of silicon doped with phosphorous is ascribable to this extra electron, which can easily jump to the conduction band to involve electrical conductivity. Atoms that can donate unused electrons to the valence band are called donors, and energy levels created just below the conduction band by donors are called donor levels (Figure 1-2A, right).

Silicon acquires similarly enhanced electrical conductivity when it is doped with aluminium. Since the valence electron configuration of aluminium is 3s^2, 3p^1, a deficit of one electron corresponding to the introduction of one hole to the aluminium occurs (Figure 1-2B, left). The holes introduced *via* aluminium doping easily accept electrons from the valence band to generate holes in the valence band, and these are involved in the electrical conductivity. The energy levels created just above the valence band by acceptors are called acceptor levels (Figure 1-2B, right).
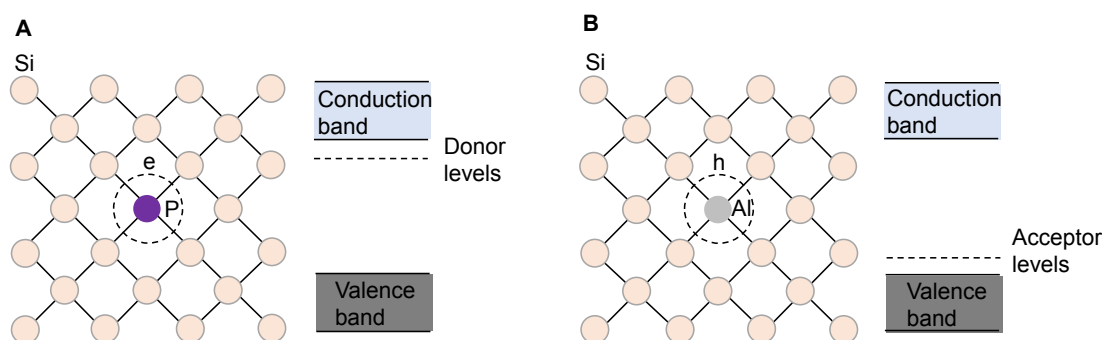
Figure 1-2. (A) Donor impurity in a semiconductor crystal (left) and the associated energy band diagram (right) and (B) acceptor impurity in a semiconductor crystal (left) and the associated energy band diagram (right).

1.1.3   Heteroelemental Doping of TiO$_2$
1.1.3.1 Light Absorption by TiO$_2$

The most intensively investigated semiconductor oxide is TiO$_2$ because of its superior physical and chemical properties.[4-6] TiO$_2$ absorbs light with energy

corresponding to the band gap energy, and a charge separation then occurs. The band gap energy of TiO_2 corresponds to light in the range from UV to near-UV. It is due to these light absorption properties of TiO_2 that it has been used for applications in pigments and photocatalysts.

The band gap energy of TiO_2 is dependent on its crystal phases. TiO_2 has three polymorphs: anatase, rutile and brookite (Figure 1-3).[7,8] The parameters of the different crystal phases are shown in Table 1-1. It should be noted that the number of reports on brookite is limited, since synthesis of brookite in a single phase is difficult compared to synthesis of anatase and rutile.[7,8]

Table 1-1. Parameters of TiO_2 polymorphs.

Crystal phases	Crystal systems	Lattice parameters			Band gap energies
		a	b	c	
Anatase	Tetragonal	5.36	5.36	9.53	3.2
Rutile	Tetragonal	4.59	4.59	2.96	3.0
Brookite	Orthorhombic	9.15	5.44	5.14	3.2
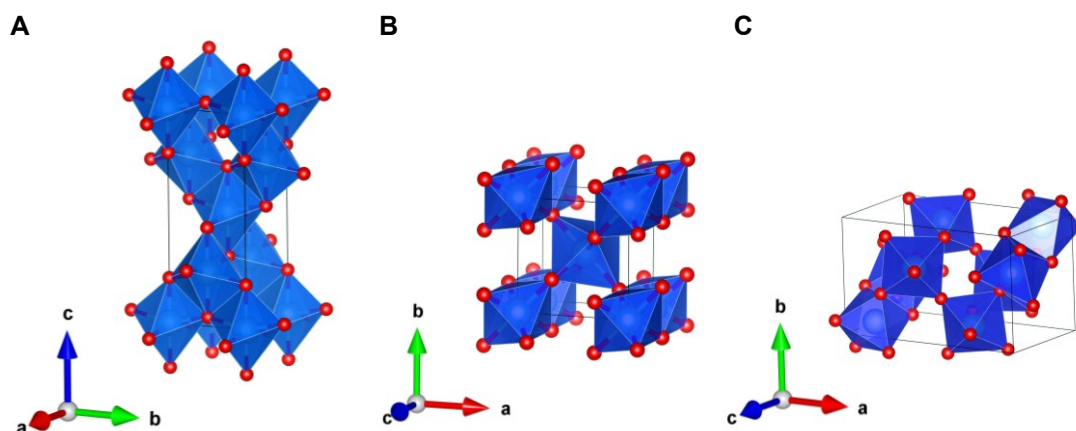
Figure 1-3. Crystal structures of (A) anatase, (B) rutile and (C) brookite.

1.1.3.2 Doping of TiO_2 with 3d Transition Metals

Although TiO_2 absorbs UV to near-UV light, visible-light absorption is developed by substitutional doping of the TiO_2 lattice at the Ti site with carefully chosen 3d transition metals. It is common for 3d metals such as V, Cr and Fe to create localized levels between the TiO_2 band gaps, and for electrons to be excited from the valence band to the localized level or from the localized level to the conduction band,

resulting in visible-light absorption.[9]

In the case of V, the visible-light absorption is ascribable to electron photoexcitation from the valence band to the V $_{t2g}$ level (Figure 1-4A). The visible-light absorption of Fe- and Cr-doped TiO_2 is ascribable to electron photoexcitation from the Fe $_{t2g}$ level to the conduction band (Figure 1-4B), and to electron photoexcitation from the valence band to the Cr $_{t2g}$ level and from the Cr $_{t2g}$ level to the valence band, respectively (Figure 1-4C).[9]
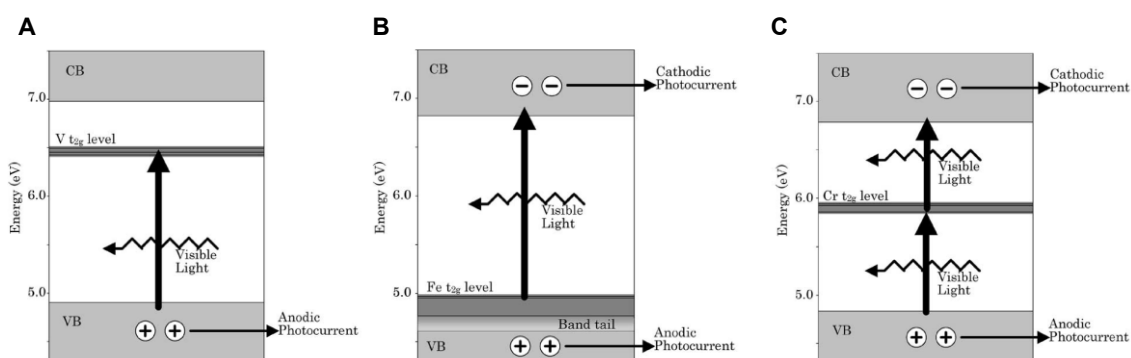

Figure 1-4. Schematic diagram illustrating the photoexcitation process under visible light of (A) V-, (B) Fe- and (C) Cr-doped TiO_2. Reprinted from Ref. [9] with permission.

1.1.3.3 Doping of TiO_2 with Nitrogen

Likewise, doping with non-metal elements such as N, C, P and F has also been studied to control the light-absorption properties of TiO_2.[10-13] Among these, nitrogen doping has been studied extensively to develop visible-light absorption by TiO_2. It is common for the absorption edge of TiO_2 to be extended to around 2.4 eV when anatase or rutile is interstitially doped with nitrogen to form an NO_x species. This is ascribable to the fact that the antibonding state of the NO_x species creates a localized level ~ 0.7 eV above the valence band of TiO_2 (Figure 1-5) to excite electrons from the localized state to the conduction band. On the other hand, when nitrogen is substituted for doping of TiO_2 at the oxygen site, an N 2p level is created slightly (~ 0.1 eV) above the valence band of anatase, while in the case of rutile, an N 2p level is created slightly (~ 0.05 eV) below the valence band. Visible-light absorption is therefore, not developed in the case of substitutional doping of TiO_2.[14,15]
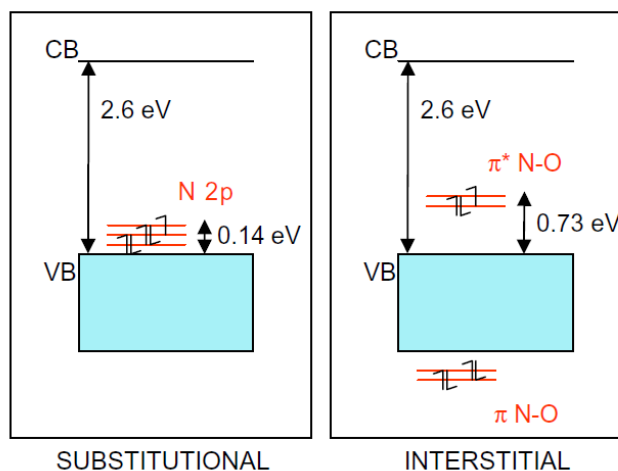
Figure 1-5. Electronic structures for substitutional and interstitial models of nitrogen-doped TiO_2. Reprinted from Ref. [14] with permission.

1.1.3.4 Co-doping with a 3d Transition Metal and Nitrogen

Co-doping with a 3d transition metal and nitrogen has also been conducted, but the number of reports is limited compared to that for mono-doping. The merit of co-doping is its ability to suppress the formation of vacancies which are formed for purpose of charge compensation in mono-doped systems. Enhancement of visible-light absorption due to electron photoexcitation between the localized level created by nitrogen and that created by the 3d transition metal is, moreover, also to be expected. Previous reports on co-doping with 3d transition metals and nitrogen that shows enhanced visible-light absorption compared to mono-doping systems are listed in Table 1-2.[16-25]

Table 1-2. Co-doped TiO$_2$ with 3d transition metals and nitrogen.

| Dopant | | Introduction | Introduction | Crystal structure | References |
metal	non-metal	method of metal	method of N	of host TiO$_2$	
Nb	nitrogen	polymerized complex method	NH$_3$ annealing	anatase/rutile	Sakatani et al. J. Mater. Res. (2004)
	nitrogen	sol-gel method	sol-gel method	anatase	Lim et al. J. Catal. (2014)
	nitrogen	sol-gel method	NH$_3$ annealing	anatase	Breault et al. J. Phys. Chem. C (2013)
Fe	nitrogen	polymerized complex method	NH$_3$ annealing	anatase/rutile	Sakatani et al. J. Mater. Res. (2004)
	nitrogen	sol-gel method	sol-gel method	anatase/brookite	Hao, et al. Microporous Mesoporous Mater. (2009)
V	nitrogen	sol-gel method	sol-gel method	anatase	Jaiswal et al. Appl. Catal. B Environ. (2012)
	nitrogen	sol-gel method	stirring in aqueous TEA solution	anatase	Gu et al. Catal. Commun. (2008)
Cu	nitrogen	sol-gel method	sol-gel method	anatase	Song et al. Commun. Am. Cer. Soc. (2008)
Cr	nitrogen	sol-gel method	sol-gel method	anatase	Chen et al. J. Mol. Struct. (2011)
Mn	nitrogen	sol-gel method	sol-gel method	anatase	Zhao et al. J. Solid State Chem. (2016)
Ni	nitrogen	sol-gel method	sol-gel method	anatase	Zhang et al. Appl. Surf. Sci. (2008)

1.2 Creation of TiO$_2$-based Heterojunctions for Enhanced Photocatalytic Activity

1.2.1   Overview of This Section

This section will begin with a brief outline of *p-n* junction, which is a representative semiconductor-semiconductor heterojunction.[1-3] It will then describe the mechanism of TiO$_2$ photocatalysts, and follow this with details such as the mechanism of enhanced charge separation efficiency and the subsequent enhanced photocatalytic activity present synthetic procedures of TiO$_2$-based herterojunctions.

1.2.2   *p-n* Junction

When a heterojunction between *n*- and *p*-type semiconductors, a so-called "*p-n* junction", is created, electrical behavior different from that of the separate components emerges. In the junction region, electrons are diffused from the *n*-type region to the *p*-type region, and holes are diffused in the opposite directions, respectively. As a result of this charge diffusion, electrons and holes are combined to create a depletion region, in which neither electrons nor holes exist. In the depletion region, negatively charged acceptor atoms are left in the *p*-type region and positively charged donor atoms are left in the *p*-type region, respectively, and these charges create diffusion potential. The Fermi levels of two components must exhibit an equal thermal equilibrium, with their energy levels shifted in the vertical direction with respect to each other, resulting in bending of the band structure (Figure 1-6). Due to this bending of the band structure, electrons and holes are quickly separated in the depletion region.
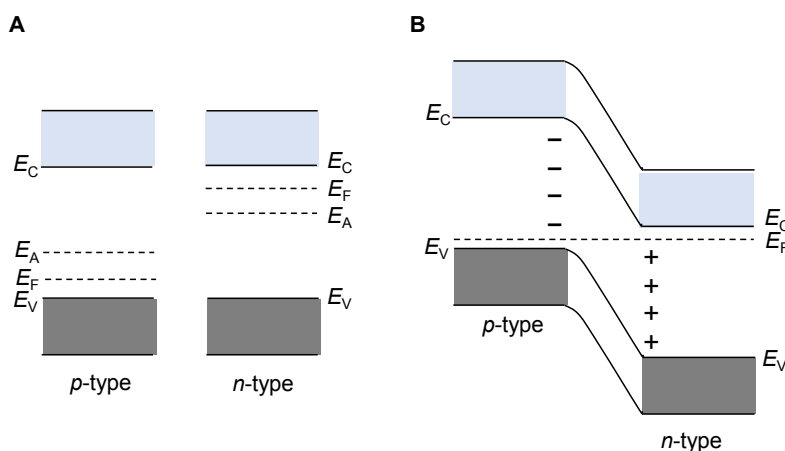

Figure 1-6. Schematic representation of (A) *n*- and *p*-type semiconductors with no junction region and (B) a *p-n* junction in thermal equilibrium.

The *p-n* junction shows totally different electrical conductivity depending on the direction of electric current. When the *p*-type is connected to the positive electrode, the Fermi level changes to enhance diffusion of electrons from the *n*-type region to the *p*-type region and diffusion of holes from the *p*-type region to the *n*-type region, and the *p-n* junction shows electrical conductivity (Figure 7A). This arrangement is called a forward bias. On the other hand, when the *p*-type is connected to the negative electrode, the Fermi level changes to suppress charge diffusion (Figure 7B). This arrangement is called a reverse bias.[1-3]
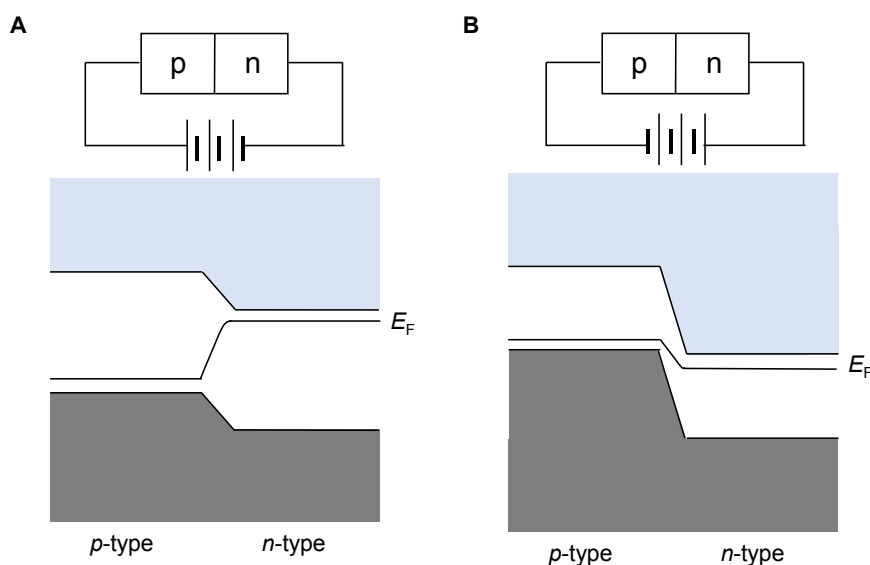

Figure 1-7. Schematic representation of a *p-n* junction under (A) forward and (B) reverse biases.

1.2.3   TiO$_2$-based Heterojunctions

1.2.3.1 Photocatalytic Reaction of TiO$_2$

While photoexcited electrons and generated holes are easily recombined after light-induced charge separation, when photoexcited electrons or created holes are moved to adsorbed reactants on the outer particle surface of semiconductors, the adsorbed reactants are reduced or oxidized by photoexcited electrons or created holes, respectively (Figure 1-8). TiO$_2$ is one of the most promising semiconductor photocatalysts because of its low cost, stability and non-toxicity, and efforts have thus been made to enhance the photocatalytic activity of TiO$_2$ mainly by increasing its surface area and enhancing its charge separation efficiency, since these largely affect the photocatalytic activity of semiconductor photocatalysts. Creation of heterojunctions

between TiO$_2$ nanoparticles and metal nanoparticles or other types of TiO$_2$ nanoparticles is known to be an effective methodology for enhancing their charge separation efficiency.
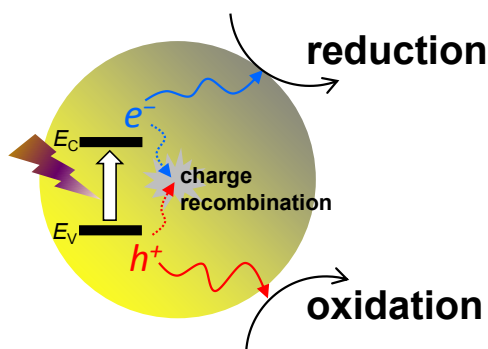

Figure 1-8. Schematic of charge separation induced by light irradiation and subsequent photocatalytic reactions.

1.2.3.2 TiO$_2$-Metal Heterojunction

Creation of heterojunctions between TiO$_2$ and metals such as Pt is one of the most promising strategies for enhancing photocatalytic activity, since electron-hole recombination in TiO$_2$ can be suppressed due to electron diffusion from TiO$_2$ to the metals (Figure 1-9). When *n*-type semiconductors including TiO$_2$ are connected to metals, whose work function (ϕ_m) is larger than that of the *n*-type semiconductors (ϕ_S), electrons are diffused from the semiconductors to the metals, resulting in an equal Fermi level of thermal equilibrium. As a result of the electron diffusion, the metal acquires an excess negative charge, while positively charged donor atoms are left in the semiconductor. As a result, a depletion region, in which no charges exist, is created in the semiconductor, and the conduction band of the semiconductor bends upward toward the surface (Figure 1-10). The barrier created between the semiconductor and metal is called a Schottky barrier, and the height of the barrier (ϕ_b) is given by the below equation:

$$\phi_b = \phi_m - E_\chi$$

where E_χ represents the electron affinity measured from the energy gap between the conduction band edge and the vacuum level of the semiconductor. The enhanced charge

separation efficiency and subsequent enhanced photocatalytic activity of the TiO_2-metal heterojunction can be explained by diffusion of photoecxited electrons from the TiO_2 to the metals due to creation of a Schottky barrier.[26]
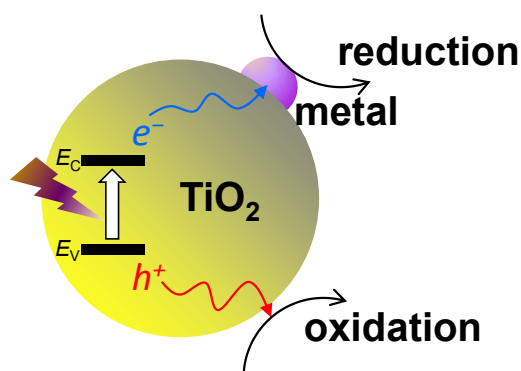

Figure 1-9. Scheme for charge diffusion from TiO_2 to metal.
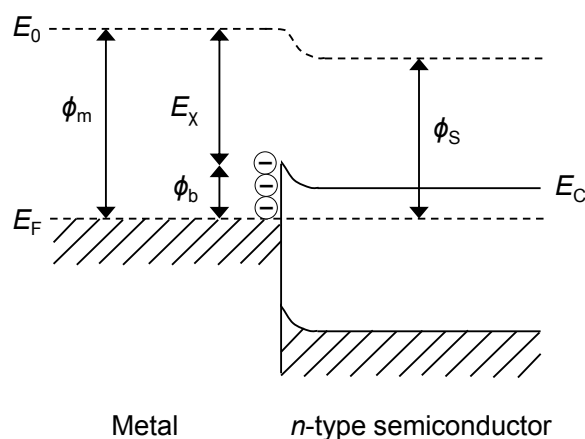
Figure 1-10. Schematic of a Schottky barrier.

1.2.3.3 TiO$_2$-TiO$_2$ Heterojunction

In addition to TiO_2-metal heterojunctions, it is also well known that the photocatalytic activity of TiO_2 is enhanced by creating heterojunctions between different types of TiO_2, and combinations of anatase and rutile have been investigated especially. In order to reveal the mechanism of the enhanced photocatayltic activity of TiO_2 with an anatase-rutile heterojunction, Kawahara *et al.* prepared patterned anatase/rutile TiO_2 film, which decomposed CH_3CHO more efficiently than sole anatase or rutile film, and investigated the locations of Ag nanoparticles deposited on the

patterned film *via* photoreduction of aqueous Ag^+ species.[27] Ag nanoparticles were deposited on rutile particles at the anatase/rutile interfaces, and electron transfer from anatase to rutile was thus indicated (Figure 1-11). The electron transfer was ascribable to the fact that the conduction band potential of anatase is about 0.2 eV higher than that of rutile[28] and the energy barrier should suppress an opposite electron transfer. The enhanced photocatayltic activity of TiO_2 with anatase-rutile heterojunction was therefore ascribable to the enhanced charge separation efficiency of anatase *via* electron transfer from anatase to rutile (Figure 1-12).
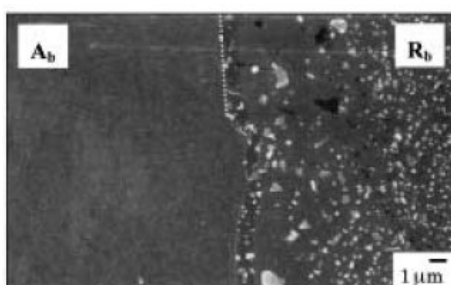
Figure 1-11. SEM image of the boundary region of anatase and rutile after Ag photodeposition. "A" and "R" denote anatase and rutile, respectively. Reprinted from Ref. [27] with permission.
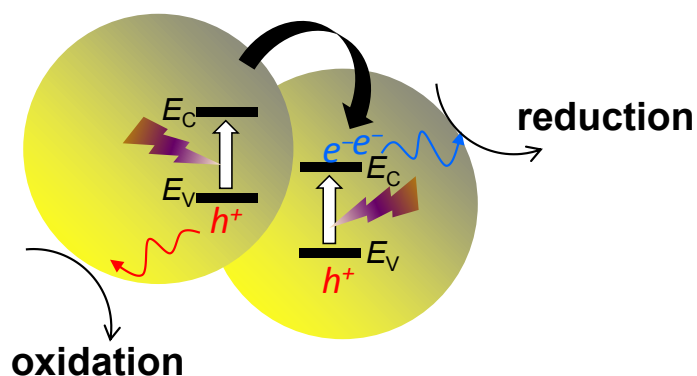
Figure 1-12. Schematic of charge transfer between anatase and rutile.

1.2.3.4 Synthetic Procedures for TiO_2-TiO_2 Heterojunction Creation

1.2.3.4.1   Calcination of Anatase

In this section, representative studies on the creation of TiO_2-TiO_2 heterojunctions are presented. Li *et al.* deposited amorphous titania by impregnation of rutile nanoparticles with a solution of titanium tetraisopropoxide in 2-propanol and

subsequent drying, and the amorphous titania was transformed into anatase by calcination at different temperatures for anatase-rutile hererojunction creation.[29] The anatase/rutile ratios on the outer particle surface were controlled by changing the time period and temperature (Figure 1-13), and the highest activity for H_2 evolution from water containing methanol was observed only when anatase and rutile co-existed on the outer particle surface. This result indicated that the charge separation efficiency of TiO_2 was enhanced *via* charge transfer between anatase and rutile.
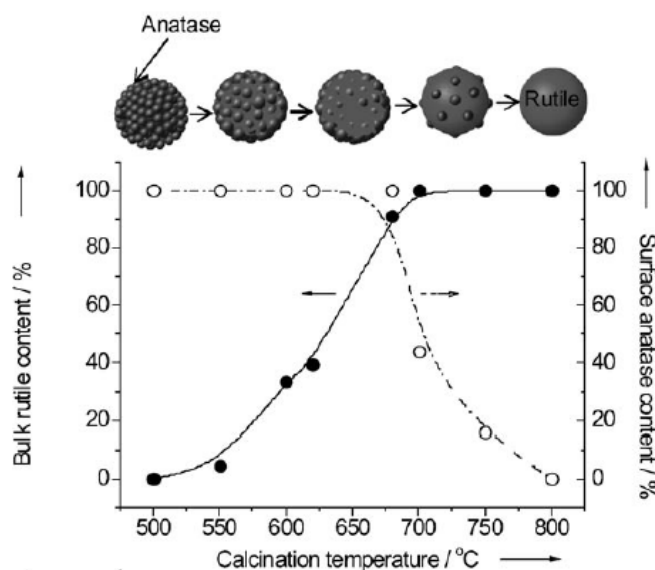
Figure 1-13. Dependence of bulk rutile content (filled circles, solid line) and surface anatase content (open circles, broken line) on the calcination temperature. Reprinted from Ref. [29] with permission.

1.2.3.4.2 Dissolution-Reprecipitation of Anatase

Kawahara *et al.* prepared anatase-rutile heterojunctions *via* a dissolution-reprecipitation process of rutile TiO_2 using an aqueous H_2SO_4 solution.[30] Rutile TiO_2 nanoparticles were partially decomposed into Ti^{4+}, amorphous titania was deposited on the outer particle surface of the rutile nanoparticles, and the amorphous titania was transformed to anatase by subsequent annealing. The obtained particles with anatase-rutile heterojunctions showed higher photocatalytic activity compared to the original rutile or a simple anatase/rutile mixture, indicating enhanced charge separation by electron transfer *via* the heterojunctions.

1.2.3.4.3   Coating Method

Kawahara *et al.* prepared patterned anatase/rutile TiO_2 film on quartz substrates by the coating method.[27] A $Ti(OC_4H_9)_4$ solution containing 1-phenyl-1,3-butanedione ($BzCH_2Ac$) was hydrolyzed, and a quartz substrate, on which rutile film was deposited, was dipped in this solution. The dried gel film was irradiated with UV-light through a photomask. $BzCH_2Ac$ forms a chelate complex with Ti^{4+} and absorbs about 360 nm of light to induce low solubility of the gel for ethanol, such that only the gel under the photomask was leached out by ethanol treatment. The gel film exhibited 0.2 mm wide stripes and spacing of 0.2 mm (Figure 1-14). This patterned amorphous TiO_2 was transformed to anatase by calcination at 500 ^{o}C, producing patterned anatase/rutile TiO_2 film.
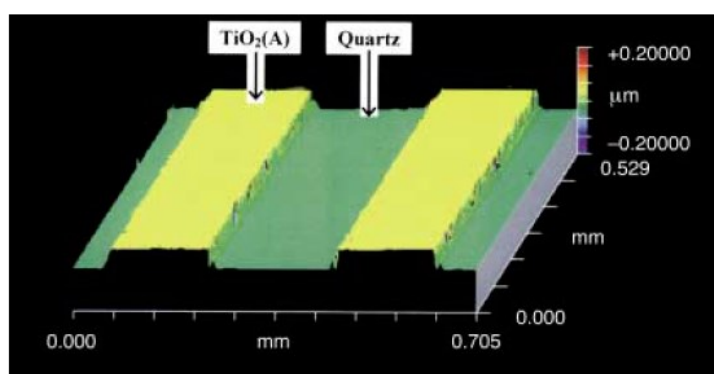
Figure 1-14. Three-dimensional surface-structure photograph of patterned anatase/rutile film. Reprinted from Ref. [27] with permission.

1.3 Objectives of This Thesis

As described in the above discussion, light absorption by TiO_2 can be controlled by heteroelemental doping to create localized levels between the band gaps. On the other hand, when a heterojunction is created between different types of TiO_2, charge transfer occurs *via* the heterojunction, resulting in enhanced charge separation efficiency and subsequent enhanced photocatalytic activity.

In this thesis, control of light absorption by TiO_2 *via* heteroelemental doping is attempted through co-doping with Nb and N. As mentioned above, the number of reports on co-doping of TiO_2 is limited compared to those on mono-doping. Moreover, co-doping of TiO_2 has been conducted by rather complicated processes such as the

sol-gel method. One objective of this thesis is to propose a facile methodology for preparation of co-doped TiO_2 and control of light absorption by TiO_2 *via* creation of localized levels between band gaps.

In this study, however, attachment of TiO_2 particles to the outer particle surface of layered titanate is described as a route to enhancing charge separation and subsequent enhanced photocatalytic activity *via* creation of heterojunction. Layered titanates have been utilized in conjunction with TiO_2 to create TiO_2-based heterojunctions, since they are exfoliatable *via* intercalation reactions and can then be restacked with TiO_2 nanoparticles, resulting in large interfaces for efficient charge transfer. Creation of heterojunctions between layered titanates and TiO_2 requires multi step intercalation reactions and strict conditions. The other objective of this thesis is to suggest a facile methodology for creating layered titanate-TiO_2 heterojunctions that show enhanced charge separation.

In chapter 2, preparation of TiO_2 with different Nb contents which were subsequently annealed under a NH_3 flow is described. Nb-doped TiO_2 with different Nb contents was prepared by liquid-feed flame spray pyrolysis (LF-FSP), which is a promising tool for producing mixed-metal oxide nanopowders in which elemental mixing is often at the atomic level. The effect of Nb-doping and the NH_3 annealing on the light-absorption properties of TiO_2 are discussed.

In chapters 3 and 4, creation of heterojunctions between TiO_2 and layered tiatanates and charge transfer *via* the heterojunctions are introduced.

In chapter 3, creation of heterojunctions between protonated layered titanate and TiO_2 by mixing them in water at room temperature under ambient pressure is described. Formation of the protonated layered titanate/TiO_2 composite is investigated by monitoring the aggregation size in water and observing the agglomerate after water evaporation. The photocatalytic activity of the composite for oxidative decomposition of formic acid is investigated to discuss possible enhanced charge separation efficiency as a result of charge transfer *via* the heterojunctions. Charge transfer *via* the heterojunctions is also discussed. Finally, the photocatalytic activity of the composite for hydrogen evolution from water is investigated.

In chapter 4, a methodology for creating protonated layered titanate-TiO_2 heterojunctions on the outer particle surface of the protonated layered titanate by treating layered potassium titanate with diluted HCl and then drying it at room

temperature under reduced pressure is described. In order to investigate photoexcited electron transfer from the protonated layered titanate to TiO_2 *via* heterojunctions, hydrogen evolution under light with energy larger than the band gap energy of the protonated titanate was investigated. In order to investigate photoexcited electron transfer from rutile to the protonated titanate *via* the heterojunctions, meanwhile, light that can excite only rutile was irradiated. Hole transfer between them was not investigated based on the results in chapter 3.

Chapter 5 shows the conclusions of this thesis.

1.4 References

[1]   Solid-State Physics; Ibach, H. and Luth, H.; Springer: New York, 1991.

[2]   Understandibg Solids, The science of Materials; Tilley, R. J. D.; Wiley: New Delhi, India, 2004.

[3]   Solid State Physics; Ashcroft, N. W. and Mermin, N. D.; CENGAGE Learning: India, 1976.

[4]   Fujishima, A.; Zhang, X.; Tryk, D. A. TiO_2 Photocatalysis and Related Surface Phenomena. *Surf. Sci. Rep.* **2008**, *63*, 515–582.

[5]   Chen, X.; Mao, S. S. Titanium Dioxide Nanomaterials: Synthesis, Properties, Modifications, and Applications. *Chem. Rev.* **2007**, *107*, 2891-2959.

[6]   Pfaff, G.; Reynders, P. Angle-Dependent Optical Effects Deriving from Submicron Structures of Films and Pigments. *Chem. Rev.* **1999**, *99*, 1963–1982.

[7]   Mo, S.-D.; Ching, W. Y. Electronic and Optical Properties of Three Phases of Titanium Oxide: Rutile, Anatase, and Brookite. *Phys. Rev.* **1995**, *51*, 13023-13032.

[8]   Landmann, M.; Rauls, E.; Schmidt, W. G. The Electronic Structure and Optical Response of Rutile, Anatase and Brookite TiO_2. *J. Phys. Condens. Matter* **2012**, *24*, 195503.

[9]   Umebayashi, T.; Yamaki, T.; Itoh, H.; Asai, K. Analysis of Electronic Structures of 3d Transition Metal-Doped TiO_2 Based on Band Calculations. *J. Phys. Chem. Solids* **2002**, *63*, 1909–1920.

[10]   Yu, J. C.; Yu, J.; Ho, W.; Jiang, Z.; Zhang, L. Effects of F-doping on The Photocatalytic Activity and Microstructures of Nanocrystalline TiO_2 Powders. *Chem. Mater.* **2002**, 14, 3808–3816.

[11] Irie, H.; Watanabe, Y.; Hashimoto, K. Carbon-Doped Anatase TiO$_2$ Powders as a Visible-Light Sensitive Photocatalyst. *Chem. Lett.* **2003**, *32*, 772–773.

[12] Ohno, T.; Mitsui, T.; Matsumura, M. Photocatalytic Activity of S-doped TiO$_2$ Photocatalyst under Visible Light. **2003**, *32*, 364–365.

[13] Irie, H.; Watanabe, Y.; Hashimoto, K. Nitrogen-Concentration Dependence on Photocatalytic Activity of TiO$_{2-x}$N$_x$ powders. *J. Phys. Chem. B* **2003**, *107*, 5483–5486.

[14] Valentin, C. D.; Finazzi, E.; Pacchioni, G.; Selloni, A.; Livraghi, S.; Paganini, M. C.; Giamello, E. N-doped TiO$_2$: Theory and Experiment. *Chem. Phys.* **2007**, *339*, 44–56.

[15] Valentin, C. D.; Pacchioni, G.; Selloni, A. Origin of the Different Photoactivity of N-Doped Anatase and Rutile TiO$_2$. *Phys. Rev. B - Condens. Matter Mater. Phys.* **2004**, *70*, 085116.

[16] Breault, T. M.; Bartlett, B. M. Composition Dependence of TiO$_2$:(Nb,N)-X Compounds on the Rate of Photocatalytic Methylene Blue Dye Degradation. *J. Phys. Chem. C* **2013**, *117*, 8611–8618.

[17] Liu, L.; Chen, S.; Sun, W.; Xin, J. Enhancing the Visible Light Absorption via Combinational Doping of TiO$_2$ with Nitrogen (N) and Chromium (Cr). *J. Mol. Struct.* **2011**, *1001*, 23–28.

[18] Song, K.; Zhou, J.; Bao, J.; Feng, Y. Photocatalytic Activity of (Copper, Nitrogen)-Codoped Titanium Dioxide Nanoparticles. *J. Am. Ceram. Soc.* **2008**, *91*, 1369–1371.

[19] Jaiswal, R.; Patel, N.; Kothari, D. C.; Miotello, A. Improved Visible Light Photocatalytic Activity of TiO$_2$ co-doped with Vanadium and Nitrogen. *Appl. Catal. B Environ.* **2012**, *126*, 47–54.

[20] Gu, D.-E.; Yang, B.-C.; Hu, Y.-D. V and N Co-Doped Nanocrystal Anatase TiO$_2$ Photocatalysts with Enhanced Photocatalytic Activity under Visible Light Irradiation. *Catal. Commun.* **2008**, *9*, 1472–1476.

[21] Sakatani, Y.; Ando, H.; Okusako, K.; Koike, H.; Nunoshige, J.; Takata, T.; Kondo, J. N.; Hara, M.; Domen, K. Metal Ion and N co-doped TiO$_2$ as a Visible-Light Photocatalyst. *J. Mater. Res.* **2004**, *19*, 2100–2108.

[22] Zhang, X.; Liu, Q. Visible-Light-Induced Degradation of Formaldehyde over Titania Photocatalyst Co-Doped with Nitrogen and Nickel. *Appl. Surf. Sci.* **2008**,

254, 4780–4785.

[23] Hao, H.; Zhang, J. The Study of Iron (III) and Nitrogen co-doped Mesoporous TiO$_2$ Photocatalysts: Synthesis, Characterization and Activity. *Microporous Mesoporous Mater.* **2009**, *121*, 52–57.

[24] Zhao, Y. F.; Li, C.; Lu, S.; Liu, R. X.; Hu, J. Y.; Gong, Y. Y.; Niu, L. Y. Electronic, Optical and Photocatalytic Behavior of Mn, N Doped and co-doped TiO$_2$: Experiment and Simulation. *J. Solid State Chem.* **2016**, *235*, 160–168.

[25] Lim, J.; Murugan, P.; Lakshminarasimhan, N.; Kim, J. Y.; Lee, J. S.; Lee, S.-H.; Choi, W. Synergic Photocatalytic Effects of Nitrogen and Niobium co-doping in TiO$_2$ for the Redox Conversion of Aquatic Pollutants under Visible Light. *J. Catal.* **2014**, *310*, 91–99.

[26] Linsebigler, A. L.; Lu, G.; Yates, J. T. Jr. Photocatalysis on TiO$_2$ Surfaces: Principles, Mechanisms, and Selected Results. *Chem. Rev.* **1995**, *95*, 735–758.

[27] Kawahara, T.; Konishi, Y.; Tada, H.; Tohge, N.; Nishii, J.; Ito, S. A Patterned TiO$_2$ (Anatase)/TiO$_2$ (Rutile) Bilayer-Type Photocatalyst: Effect of the Anatase/Rutile Junction on the Photocatalytic Activity. *Angew. Chem., Int. Ed.* **2002**, *41*, 2811–2813.

[28] Scaife, D. E. Oxide Semiconductors in Photoelectrochemical Conversion of Solar Energy. *Solar Energy* **1980**, *25*, 41-54.

[29] Zhang, J.; Xu, Q.; Feng, Z.; Li, M.; Li, C. Importance of the Relationship between Surface Phases and Photocatalytic Activity of TiO$_2$. *Angew. Chem., Int. Ed.* **2008**, *47*, 1766–1769.

[30] Kawahara, T.; Ozawa, T.; Iwasaki, M.; Tada, H.; Ito, S. Photocatalytic Activity of Rutile-Anatase Coupled TiO$_2$ Particles Prepared by a Dissolution-Reprecipitation Method. *J. Colloid Interface Sci.* **2003**, *267*, 377–381.

CHAPTER 2

Nb-doping of TiO$_2$ by Liquid-feed Flame Spray Pyrolysis and Subsequent Ammonia Annealing for Tunable Visible-light Absorption

2. Nb-doping of TiO₂ by Liquid-feed Flame Spray Pyrolysis and Subsequent Ammonia Annealing for Tunable Visible-light Absorption

2-1. Introduction

Titanium dioxide (TiO$_2$) is widely used in applications including pigments,[1] photocatalysts,[2,3] dye-sensitized solar cells (DSSC),[4,5] sensors,[6] transparent conducting oxides (TCO)[7] and Li ion battery anodes,[8,9] due to its superior physical/(electro)chemical properties and low cost. In order to improve their properties, combining of different TiO$_2$ polymorphs (*e.g.* anatase and rutile)[10-15] and doping of TiO$_2$ at the Ti site with metal elements such as Cr, Co, Ni and Pt are common strategies.[16-19] Among the reported doping strategies, niobium (Nb) dopant effectively improves the performance of photocatalysts,[20] DSSC,[21] TCO[22] and Li ion battery anodes.[23]

Gas-phase pyrolysis methods such as flame spray pyrolysis (FSP) and liquid-feed flame spray pyrolysis (LF-FSP) have been used to prepare mixed-metal oxide,[24] and have been applied for doping of elements including Nb into TiO$_2$.[25-29] Titanium alkoxide and niobium chloride have previously been used as Ti and Nb precursors, respectively, but the possibility that differences in their thermal decomposition behavior induce phase segregation cannot be excluded.

Likewise, TiO$_2$ doping with F, C, S and N have also been studied.[30-33] In particular, N-doping has been investigated extensively to generate visible-light absorption in TiO$_2$, which, when undoped, absorbs light with a wavelength longer than *ca.* 400 nm very poorly because of its wide band gap (~ 3.2 eV and ~ 3.0 eV for anatase and rutile, respectively).[2]

In this study, Nb-doped TiO$_2$ nanopowders with different Nb contents were prepared by LF-FSP using chelated metal alkoxides as Ti and Nb precursors, since enhanced Nb solubility was expected due to their very similar thermal decomposition behaviors. The obtained Nb-doped TiO$_2$ with different Nb contents was subsequently annealed under NH$_3$, to correlate the Nb doping concentration and color of NH$_3$ annealed Nb-doped TiO$_2$ nanopowders. The origin of the developed colors is discussed based on light absorption properties.

2-2. Experimental

Reagents

Ammonium niobate oxalate hydrate [$NH_4Nb(C_2O_4)_2O \cdot xH_2O$] and triethanolamine [$(HOCH_2CH_2)_3N$] were purchased from Sigma-Aldrich. Titanium isopropoxide [$Ti(O^iPr)_4$] was purchased from Fischer Scientific.

Precursor preparation

Titanatrane {$N(OCH_2CH_2)_3Ti[OCH_2CH_2N(CH_2CH_2OH)_2]$}

Titanatrane was prepared as previously reported.[27,35] $Ti(O^iPr)_4$ was reacted with $N(CH_2CH_2OH)_3$ at a 1:2 molar ratio under an N_2 flow. $N(CH_2CH_2OH)_3$ was added dropwise using an addition funnel while the mixture was stirred constantly over a 4 h period. The resulting titanatrane dissolved in an isopropanol byproduct, had a TGA-determined ceramic yield of 14.3 %.

Niobatrane [$N(OCH_2CH_2)_3Nb[(OCH_2CH_2)_2NCH_2CH_2OH]$]

Niobatrane was synthesized by reacting niobium hydroxide [$Nb(OH)_5$, 59 g, 0.33 mole], which was prepared by adding aqueous ammonia to an aqueous solution of ammonium niobate oxalate hydrate, with triethanolamine [$(HOCH_2CH_2)_3N$, 98 g, 0.66 mole] using ethylene glycol [$HOCH_2CH_2OH$, 20 ml] as a solvent in a 500-ml round-bottomed flask equipped with a distill head at 190 °C in an N_2 atmosphere. Once a transparent orange liquid was obtained, most of the ethylene glycol was distilled off, and the reactor was cooled down. The resulting niobatrane had a TGA-determined ceramic yield of 9.5 %.

Powder synthesis

Nb-doped TiO_2 nanopowders were prepared by liquid-feed flame spray pyrolysis (LF-FSP). Titanatrane and niobatrane were dissolved in ethanol at selected relative concentrations of Nb (0, 0.1, 0.5, 1, 5 and 10 mol% with respect to Ti) to give a 3 wt% ceramic yield solution. The resulting solution was subsequently aerosolized with oxygen into a quartz chamber, where it was combusted in an oxygen-rich environment. Produced powders were collected downstream in rod-in-tube electrostatic precipitators (ESP) operated at 10 kV. Details of the LF-FSP process, including the apparatus, particle formation mechanism, and chelated metal alkoxides precursor studies, can be

found elsewhere.[24,36-40] The collected nanopowders were then annealed at 600 °C under an NH_3 flow (140 mL/min) for 3 h.

Characterization

The X-ray powder diffraction (XRD) patterns were recorded on a Rigaku rotating anode goniometer operating at 40 kV and 100 mA with monochromated Cu Kα radiation (0.1541 nm). For lattice parameter calculation, the powders were mixed with silicon powder as an internal standard. The JADE program 2010 was used to refine lattice constants, and to determine the presence of crystallographic phases and their weight fractions. Specific surface areas and corresponding average particle sizes were determined by the Brunauer-Emmett-Teller (BET) multipoint method from the nitrogen adsorption isotherms measured using a Micromeritics ASAP 2020 sorption analyzer. Prior to measurement, samples were evacuated at 150 °C for 8 h. BET-derived average particle sizes (d) were obtained using the equation below, where SSA and ρ are the specific surface area and the density, respectively.

$$d = \frac{6}{(\text{SSA}) \times \rho}$$

Scanning electron microscopic (SEM) images were obtained with an FEI NOVA NanoLab. Thermogravimetric analysis (TGA)/differential scanning calorimetry (DSC) curves were recorded on a Q600 simultaneous TGA/DSC (TA instruments). Raman spectra were obtained with a Renishaw in Via reflex spectrometer using a 532 nm laser. X-ray photoelectron spectroscopy (XPS) analyses were performed using a JEOL JPS-9010 spectrophotometer. The binding energies were calibrated with reference to the C 1s signal at 285.0 eV. Inductively coupled plasma atomic emission spectrometry (ICP-AES) was performed on an Agilent 5100 instrument. The samples were dissolved for the ICP-AES measurement as follows: The sample (10 mg) was dispersed in an H_2SO_4/HNO_3 mixture (8 mL, 1/1 in V/V) containing $(NH_4)_2SO_4$ (2 g) in a 100-mL glass conical beaker and the dispersion was heated at 200 °C for 30 min. The temperature was then raised by 50 °C every 30 min, and the final temperature was 350 °C. After cooling to room temperature, HCl (9 M, 20 mL) and a small amount of water were added and then heated at 160 °C for 15 min. UV-vis spectra were obtained with a JASCO V-750 spectrophotometer equipped with an integrating sphere (ISV-722 attachment).

2-3. Results and Discussion

2-3-1. Preparation and Characterization of TiO₂ Nanopowders with Selected Nb Contents.

Table 2-1 shows Nb doping contents determined by ICP-AES. The Nb contents in the samples were in good agreement with the nominal values.

Table 2-1. Nb contents in the samples determined by ICP-AES.

Nb content / mol%	
Theoretical content	Measured content
0	N. D.
0.1	0.1
0.5	0.5
1	0.9
5	4.9
10	9.8

Figure 2-1 shows XRD patterns of the samples with different Nb contents. In the XRD pattern of the undoped sample, the diffraction peaks at 2θ (CuKα) = 25.2°, 36.9°, 37.7°, 38.5°, 48.0°, 53.8°, 55.0°, 62.1°, 62.6° and 68.7° were indexed to (101), (103), (004), (112), (200), (105), (211), (213), (204) and (116) planes of anatase, respectively, while those at 2θ (CuKα) = 27.4°, 36.1°, 41.2°, 44.0°, 54.3° and 56.6° were indexed to (110), (101), (111), (210), (211) and (220) planes of rutile, respectively. In the XRD patterns of the Nb-doped samples, the diffraction peaks appeared at similar positions to those of the undoped sample and no diffraction peaks attributable to Nb compounds were observed regardless of the Nb content, indicating that they remained as binary mixtures of anatase and rutile.

In order to discuss the effect of metal precursor species on the solubility limit of Nb in TiO₂, the results of XRD analyses were compared with those of Nb-doped TiO₂

prepared by FSP in previous reports.[27-29] The reaction temperatures were 700-1200 $^{\circ}$C for FSP and 1500-2000 $^{\circ}$C for LF-FSP, respectively.[24] Based on these facts, the solubility limit of Nb in TiO_2 was determined to be around 15 mol% judging from the phase diagram.[41,42] It should be noted, however, that FSP/LF-FSP is a non-equilibrium process,[28] and it is thus difficult to predict the actual solubility limit of Nb in TiO_2 based on the phase diagram. When $NbCl_5$ was used as the Nb precursor, Nb_2O_5 was segregated from TiO_2 with 10 mol% Nb content, while TiO_2 was obtained with no Nb_2O_5 with < 10 mol% Nb content.[28] In this study, however, no Nb_2O_5 was obtained, even with 10 mol% Nb content as we expected, indicating that the Nb solubility was enhanced.
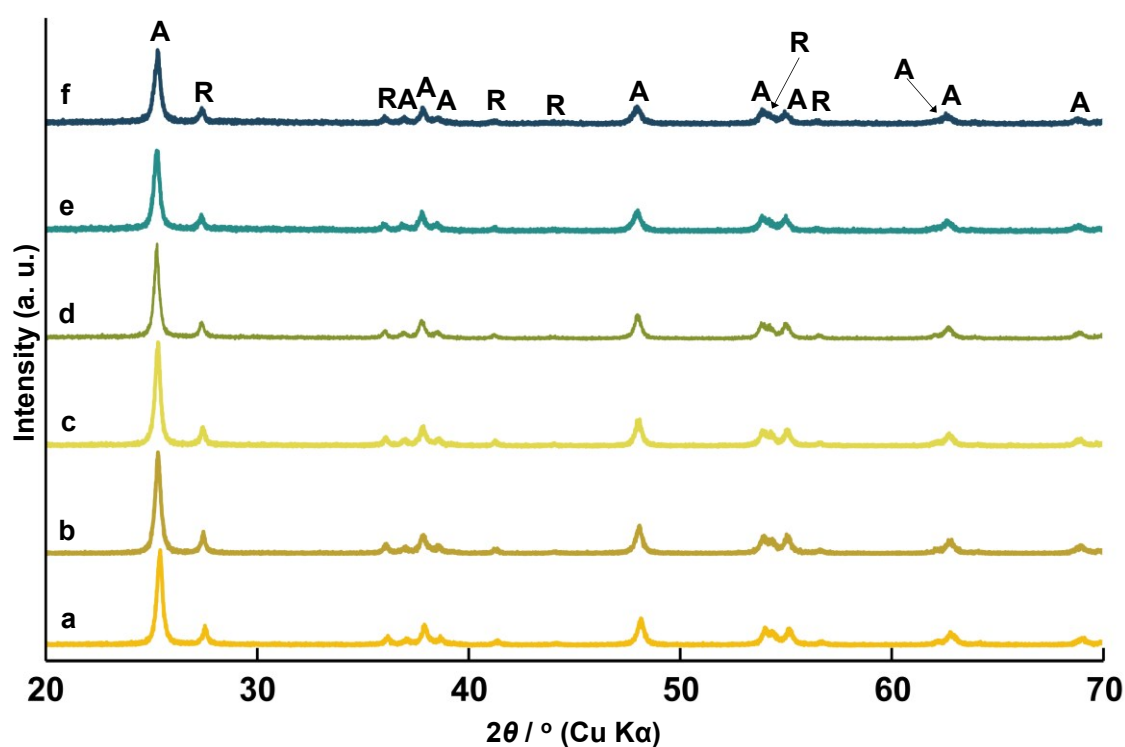

Figure 2-1. XRD patterns of a) undoped and Nb-doped TiO_2 powders with different Nb contents: b) 0.1, c) 0.5, d) 1, e) 5 and f) 10 mol%. "A" and "R" denote anatase and rutile, respectively.

Figure 2-2 shows the TGA/DSC curves of titanatrane and niobatrane, which were used as the Ti and Nb precursors, respectively. They showed very similar decomposition behaviors, and the use of these precursors for preparation of Nb-doped TiO_2 is thus likely to be effective in preventing phase segregation. On the other hand,

24

according to the literature,[43] $NbCl_5$ decomposes to form Nb_2O_5 at > 900 $^{\circ}C$, which seems to be higher than the decomposition temperature of metal alkoxide. The segregation of Nb_2O_5 from TiO_2 with a smaller Nb content[28] is therefore likely to be ascribable to the different thermal decomposition behavior of $NbCl_5$.
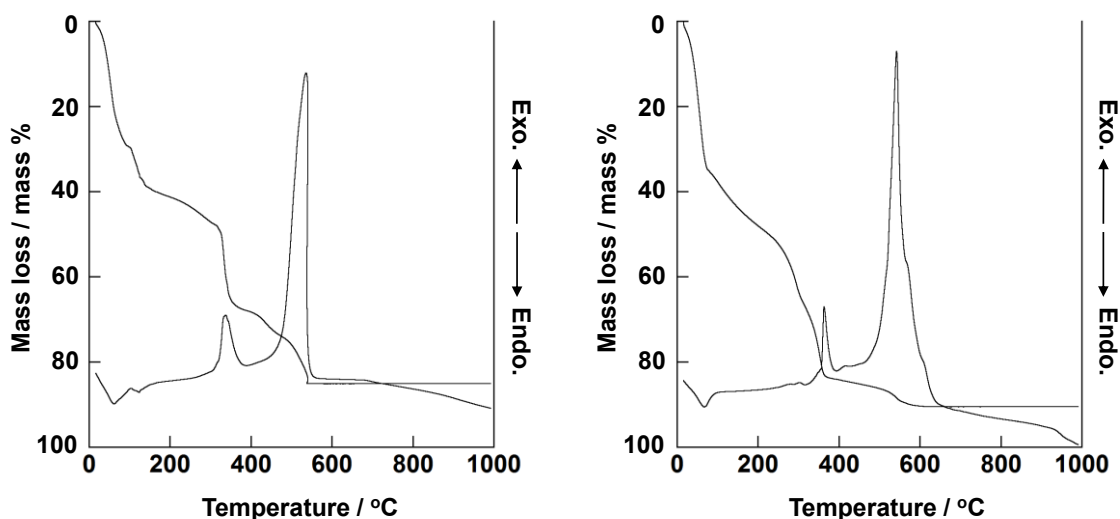

Figure 2-2. TGA/DSC curves of (A) titanatrane and (B) niobatrane.

Raman spectra (Figure 2-3) exhibited six Raman bands regardless of the Nb content. The Raman bands at 141, 192, 394, 514, 636 cm^{-1} were assigned to E_g, E_g, A_{1g}, B_{1g}, E_g modes of anatase, respectively, and the band at 445 cm^{-1} was assigned to an E_g mode of rutile.[44,45] No additional bands were observed. These results indicate that all samples remain unchanged as binary mixtures of anatase and rutile, in good agreement with the XRD results. Table 2-2 summarizes phase composition (wt%) of the samples determined by the Rietveld refinement[46] using reference files (PDF# 98-000-0081 and PDF# 98-000-0375 for anatase and rutile, respectively). Regardless of the Nb content, the main component of the samples was anatase (~ 80 wt%) and the rest (~ 20 wt%) was rutile.

The anatase/rutile phase compositions were compared with those in previous reports on Nb-doped TiO_2 with different Nb contents prepared by FSP. In the previous reports, the Nb-doped TiO_2 prepared by FSP consisted of anatase and rutile with lower Nb contents, while the rutile content decreased with increases in the Nb content.[27,29] In this study, however, no such trend was observed.
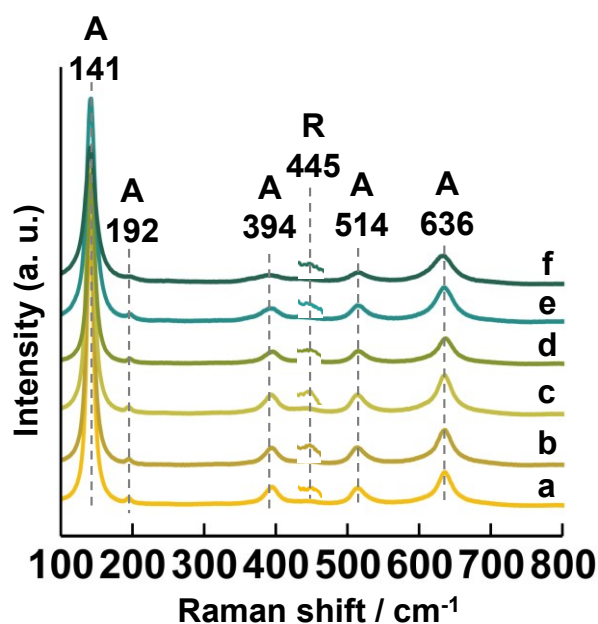
Figure 2-3. Raman spectra of a) undoped and Nb-doped TiO_2 powders with different Nb contents: b) 0.1, c) 0.5, d) 1, e) 5 and f) 10 mol%. "A" and "R" denote anatase and rutile, respectively.

Table 2-2. Phase composition of undoped and Nb-doped TiO_2 powders with different Nb contents.

Nb contents / mol%	Phase compositions / wt%	
	Anatase	Rutile
0	81	19
0.1	81	19
0.5	82	18
1	81	19
5	84	16
10	83	17

Figure 2-4 provides the variation in unit cell volumes for anatase and rutile vs. Nb content. For both anatase and rutile, unit cell volumes increased with increases in

Nb content. Considering that ionic radii of Nb^{5+} (0.069 nm) and Nb^{4+} (0.074 nm) are both larger than that of Ti^{4+}(0.068 nm),[47] the increase in the unit cell volume with increases in the Nb content suggests that Nb substitutes on the Ti^{4+} sites of both anatase and rutile. Successful Nb-doping has been reported previously.[20-23,27-29] No linear correlation between unit cell volume and Nb content was observed, which is possibly due to Ti^{4+} vacancies formed as a result of Nb doping (this point will be discussed later).[48]
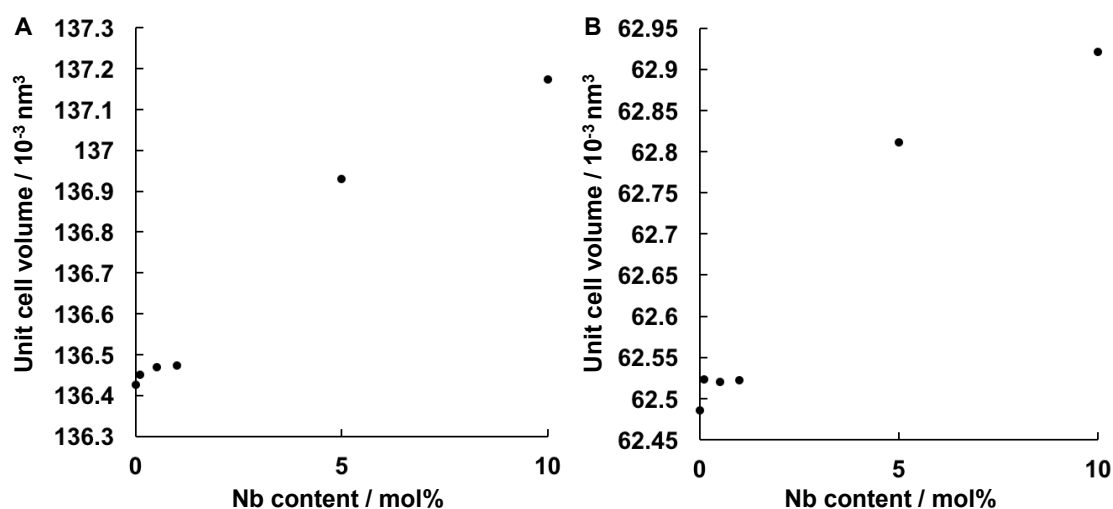

Figure 2-4. XRD-defined unit cell volume (10^{-3} nm^3) as a function of Nb contents in A) anatase and B) rutile.

Figure 2-5 shows SEM images of Nb-doped TiO_2 nanopowders with different Nb contents. All samples consisted of spherical particles with average particle sizes (APSs) of 20-50 nm. Table 2-3 lists BET-derived SSAs and corresponding APSs. The APSs of Nb-doped TiO_2 nanopowders with 0.1, 0.5, 1, 5 and 10 mol% Nb content were 27, 30, 28, 26 and 27 nm, respectively, consistent with particle size ranges estimated from SEMs (Figure 2-6). These results indicate that Nb content has essentially no effect on particle size and morphology in Nb-doped TiO_2 nanopowders.

The average particle sizes in this study were compared with those of Nb-doped TiO_2 prepared by FSP using $NbCl_5$ as an Nb precursor,[28] and the sizes were closely similar despite the difference in precursor species.

Table 2-3. BET-derived specific surface areas and average particle sizes of Nb-doped TiO$_2$ powders with different Nb contents.

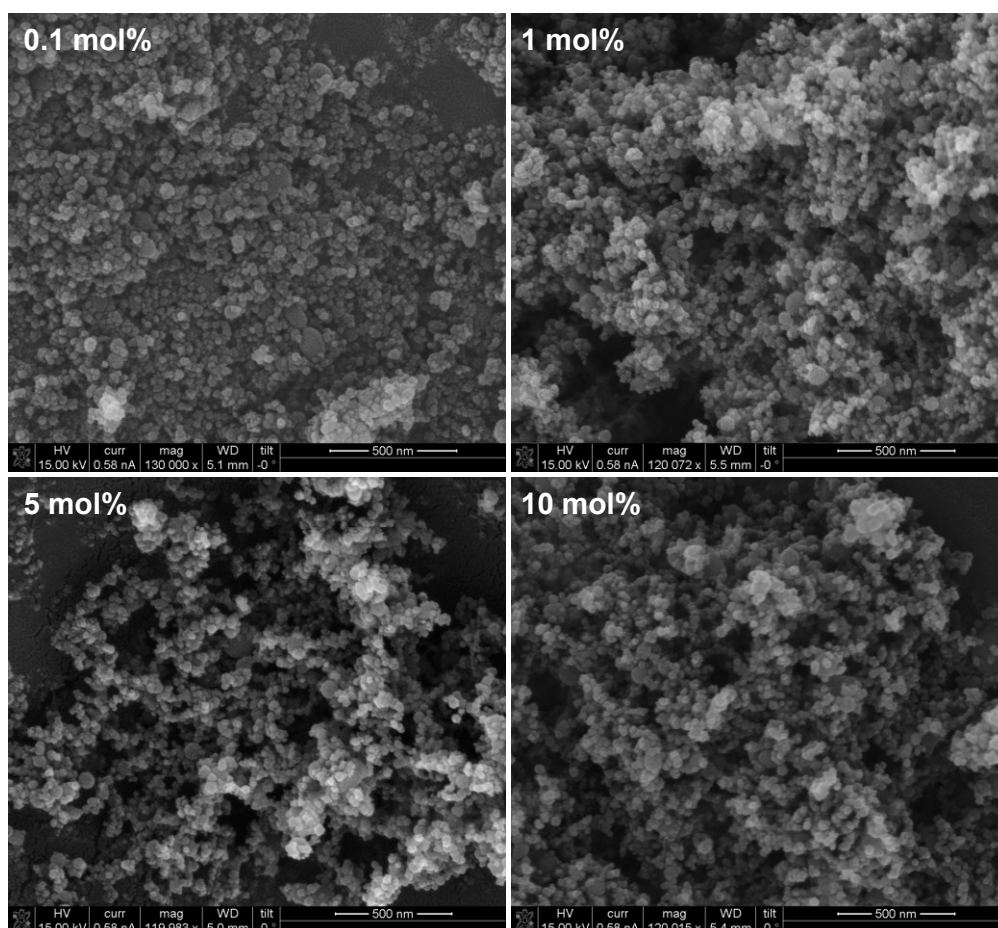| Nb content / mol%	SSAs (m^2 g^{-1})	APSs (nm)
0.1	51	27
0.5	51	30
1	54	28
5	59	26
10	56	27

Figure 2-5. SEM images of Nb-doped TiO$_2$ powders with 0.1, 1, 5 and 10 mol% Nb contents.
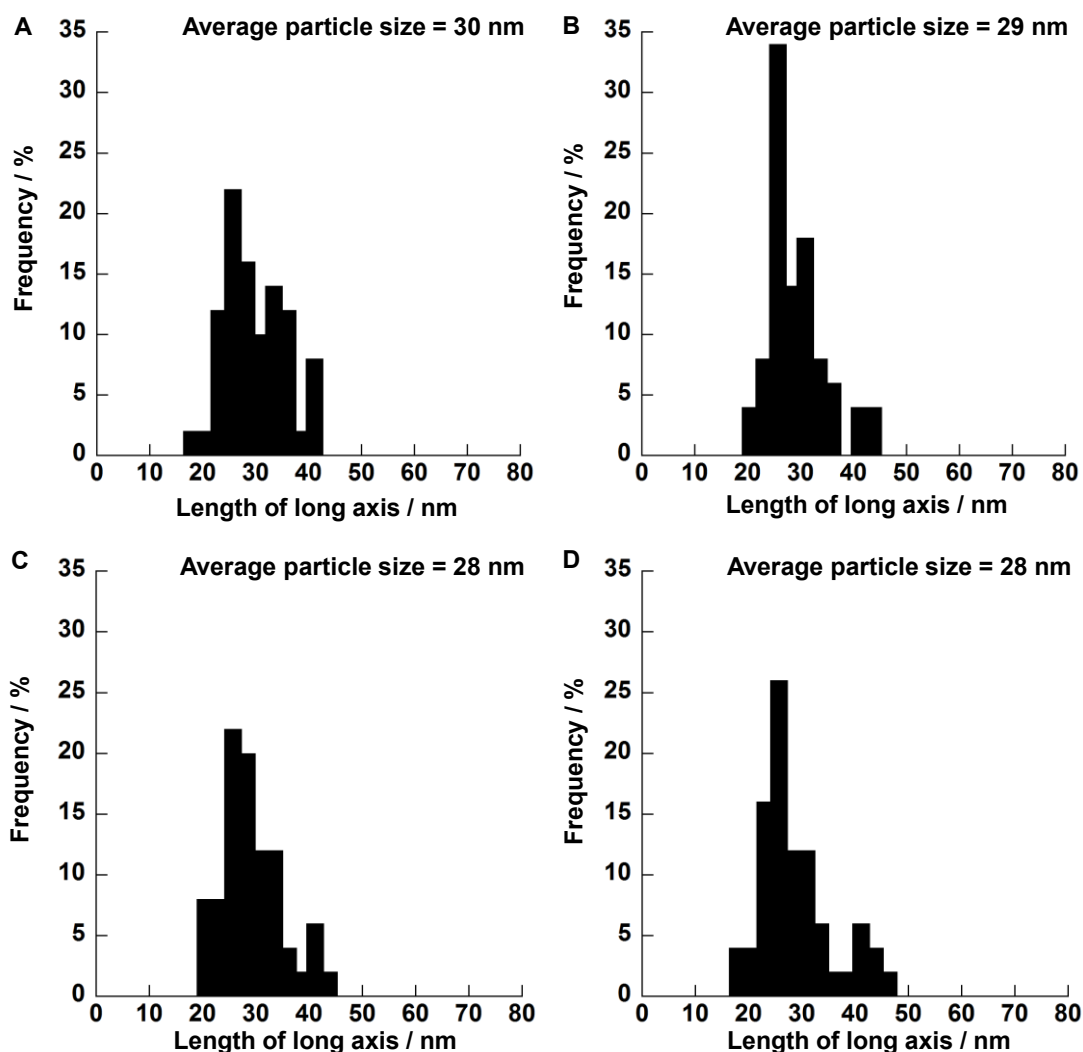
Figure 2-6. Size distribution and average particles sizes determined by SEM images of Nb-doped TiO_2 with different Nb contents: (A) 0.1, (B) 1, (C) 5 and (D) 10 mol%.

Figure 2-7 A shows XPS spectra of the Nb 3d region of undoped and Nb-doped TiO_2 powders. While no peak was identified in the XPS spectra of undoped and Nb-doped TiO_2 powders with < 1 mol% Nb contents, two peaks at 209.7 eV and 206.8 eV were observed in the XPS spectra of Nb-doped TiO_2 powders with $\geq$ 1 mol% Nb contents. These peaks are ascribable to Nb^{5+} $3d_{3/2}$ and Nb^{5+} $3d_{5/2}$, respectively.[49] These peaks are not detected in the spectra of TiO_2 powders with 0.1 and 0.5 mol% Nb contents, likely due to the Nb content being below the detection limit. As shown in Figure 2-5 B, Ti 2p XPS spectra show two peaks at 464.4 eV and 458.6 eV from Ti^{4+} $2p_{1/2}$ and Ti^{4+} $2p_{3/2}$, respectively.[50] These results indicate that Ti was present as Ti^{4+} and Nb as Nb^{5+}.
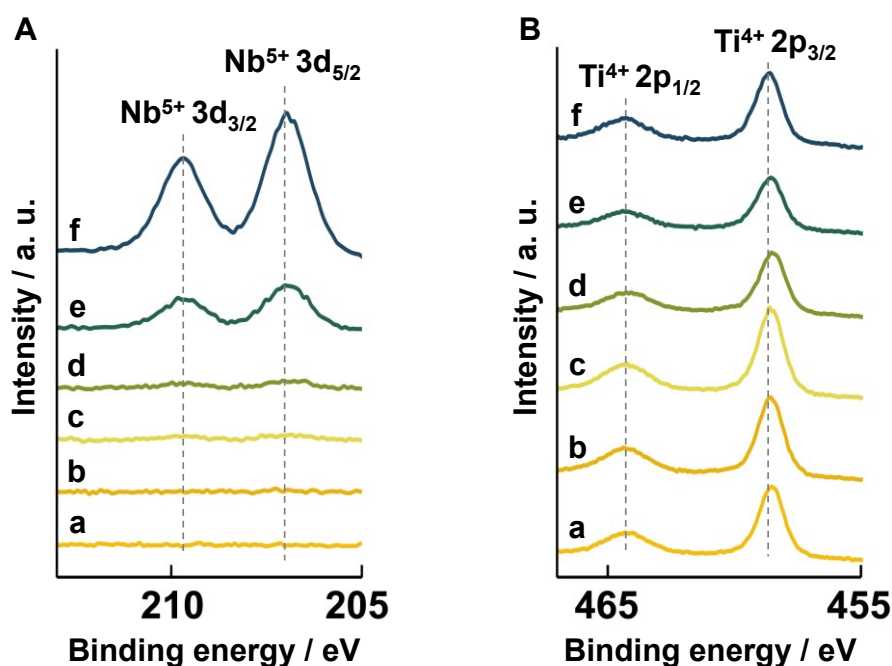
Figure 2-7. XPS spectra of (A) Nb and (B) Ti in a) undoped and Nb-doped TiO_2 powders with different Nb contents: b) 0.1, c) 0.5, d) 1, e) 5 and f) 10 mol%.

Photographs of undoped and Nb-doped TiO_2 nanopowders are presented in Figure 2-8 A. Both samples were white regardless of the Nb content. Given that Nb was doped as Nb^{5+}, as indicated by XPS, two possible routes to compensate for Nb^{5+} excess charge can be considered; one is creation of one Ti^{4+} vacancy per four Nb^{5+} introduced and the other is the reduction of Ti^{4+} to Ti^{3+}. According to a previous report,[51] when Ti^{3+} forms *via* Nb^{5+} doping of TiO_2, the sample absorbed visible light (*ca.* 520 nm – *ca.* 560 nm) *via* creation of a Ti^{3+} level in the band gap, resulting in yellow powders. In the present system, however, no evidence for visible-light absorption in these regions is observed from the diffused-reflectance UV-vis spectra of Nb-doped TiO_2 (Figure 2-8 B), indicating that the excess positive charge accompanied by Nb^{5+} is compensated by Ti^{4+} vacancy formation. Strict oxidative conditions of the LF-FSP synthesis also supports this argument.[51] On the other hand, according to a previous report,[51] peroxo species that exhibit visible-light absorption (- *ca.* 520 nm) formed on the surfaces of Nb-doped TiO_2 in compensation for the excess Nb^{5+} positive charge, accompanied by a yellow coloration. A similar material was also synthesized under strict oxidative conditions (1073 K in air) similar to the present study. However, the peroxo species were not detected in the LF-FSP synthesized Nb-doped TiO_2 based on the diffused-reflectance

UV-vis spectra.

Figure 2-8 B shows the diffused-reflectance UV-vis spectra of undoped and Nb-doped TiO_2 powders. All samples showed UV-light absorption and absorption edges at *ca.* 410 nm (*ca.* 3.0 eV) corresponding to the band gap energy of rutile (3.0 eV). This result is ascribable to the fact that the samples contained rutile, whose band gap energy of 3.0 eV is smaller than that of anatase (3.2 eV).[2] Regardless of the Nb content, the band gap energies of Nb-doped TiO_2 nanopowders were very similar to that of undoped TiO_2 nanopowder, indicating that the band gap of rutile was not narrowed by Nb-doping, a result consistent with the absence of the low-valence species. This result is consistent with that for Nb-doped TiO_2 with different Nb contents prepared by FSP using niobium chloride as an Nb precursor.[28]
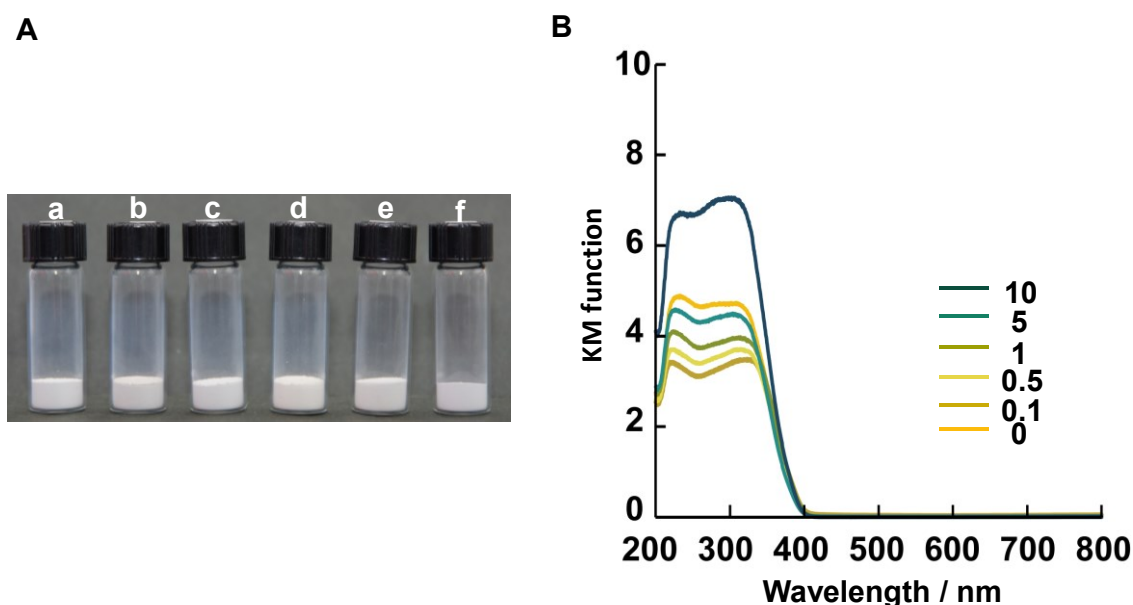

Figure 2-8. (A) Photographic images of a) undoped and Nb-doped TiO_2 with different Nb contents: b) 0.1, c) 0.5, d) 1, e) 5 and f) 10 mol%. (B) Diffused-reflectance UV-vis spectra of undoped and Nb-doped TiO_2 powders with different Nb contents.

2-3-2. N-doping into Nb-doped TiO_2 Nanopowders.

The Nb contents in Nb-doped TiO_2 nanopowders after NH_3 annealing remained unchanged (Table 2-4). As shown in the XRD patterns (Figure 2-9), the diffraction peaks were observed at similar positions to those of the samples before NH_3 annealing, and no new peaks were observed, indicating that the anatase and rutile structures were maintained after the NH_3 annealing in all samples. In the Raman spectra of the samples

(Figure 2-10), the five Raman bands ascribed to anatase were observed in all samples, while 445 cm^{-1} band from rutile was observed only in samples with $\leq$ 1 mol% Nb contents. The Raman band observed at 141 cm^{-1} in the undoped TiO$_2$ spectrum shifted to a higher wavenumber in the spectra of Nb-doped TiO$_2$, and this will be discussed later.

Table 2-4. Nb contents in undoped and Nb-doped TiO$_2$ powders after NH$_3$ annealing determined by ICP-AES.

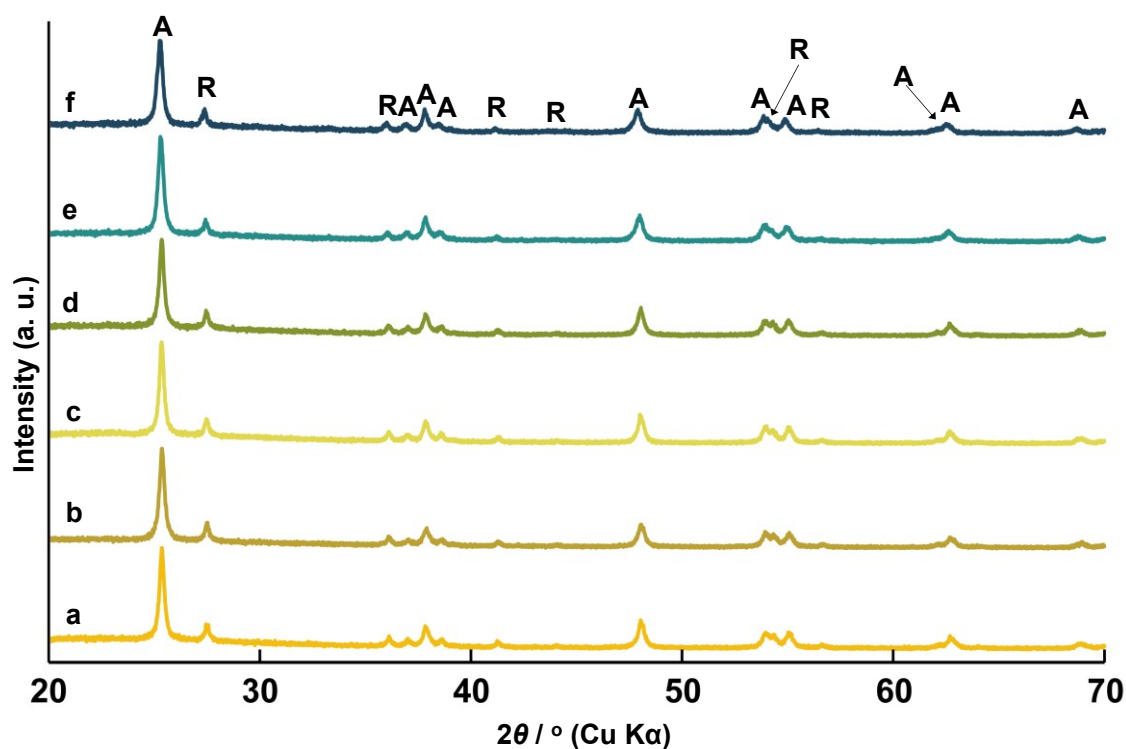| Nb content / mol%	
Initial content	Measured content
0	N. D.
0.1	0.1
0.5	0.5
1	0.9
5	5.0
10	9.7

Figure 2-9. XRD patterns of a) TiO$_2$ powder with no Nb content and Nb-doped TiO$_2$ powders with different Nb contents: b) 0.1, c) 0.5, d) 1, e) 5 and f) 10 mol% after NH$_3$ annealing . "A" and "R" denote anatase and rutile, respectively.
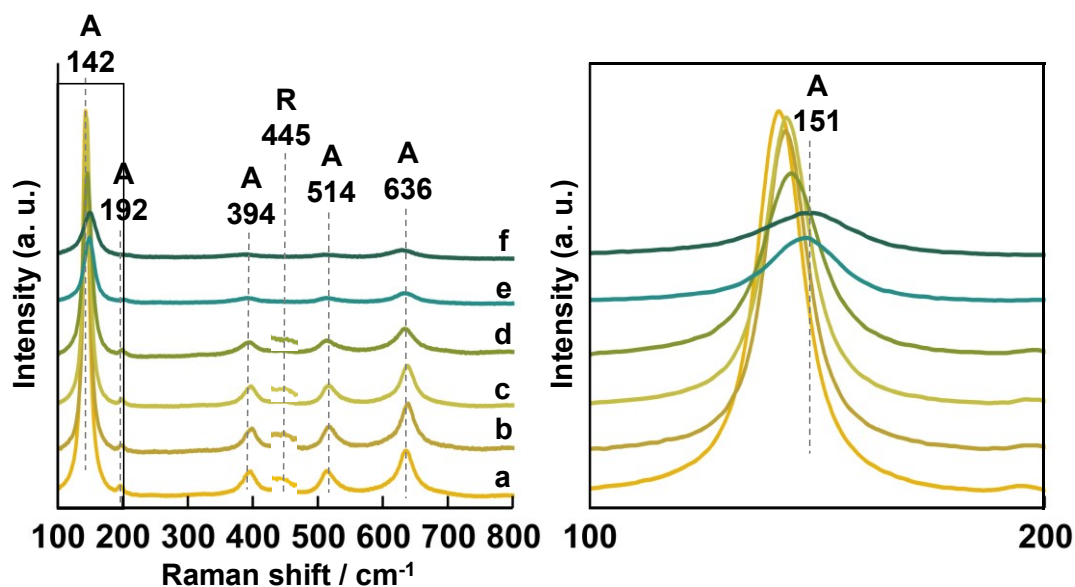

Figure 2-10. Raman spectra of a) TiO$_2$ powder with no Nb content and Nb-doped TiO$_2$ powders with different Nb contents: b) 0.1, c) 0.5, d) 1, e) 5 and f) 10 mol% after NH$_3$ annealing. "A" and "R" denote anatase and rutile, respectively.

Figure 2-11 shows the XPS spectra of the Nb 3d (Figure 2-11 A), Ti 2p (Figure 2-11 B) and N 1s (Figure 2-11 C) regions of TiO_2 nanopowder with no doping and Nb-doped TiO_2 nanopowders with different Nb contents after NH_3 annealing. Two peaks at 209.7 eV and 206.8 eV were observed in the Nb 3d XPS spectra of Nb-doped TiO_2 nanopowders with $\geq$ 1 mol% Nb contents. These binding energy values were the same as those of the samples before NH_3 annealing (Figure 2-11 A). These peaks are assigned to Nb^{5+} $3d_{3/2}$ and Nb^{5+} $3d_{5/2}$, respectively.[49] The Ti 2p XPS spectra showed two peaks at 464.4 eV and 458.6 eV, which are the same as those of the samples before NH_3 annealing (see Figure 2-11 B). These peaks are assigned to Ti^{4+} $2p_{1/2}$ and Ti^{4+} $2p_{3/2}$, respectively.[50] The N 1s XPS spectra (Figure 2-11 C) showed a new peak at 396 eV in the samples with $\geq$ 1 mol% Nb contents, and the peak intensity increased with increases in the Nb content, while no peak was observed in the samples with < 1 mol% Nb contents. This peak is ascribable to N-Ti bonding,[52] which was formed *via* substitutional N-doping into the TiO_2 lattice at oxygen sites, indicating that the amount of the substitutionally doped nitrogen likely increased with the Nb content. On the other hand, no N-O bonding (400 eV) peak, formed *via* interstitial N-doping,[52] was observed.
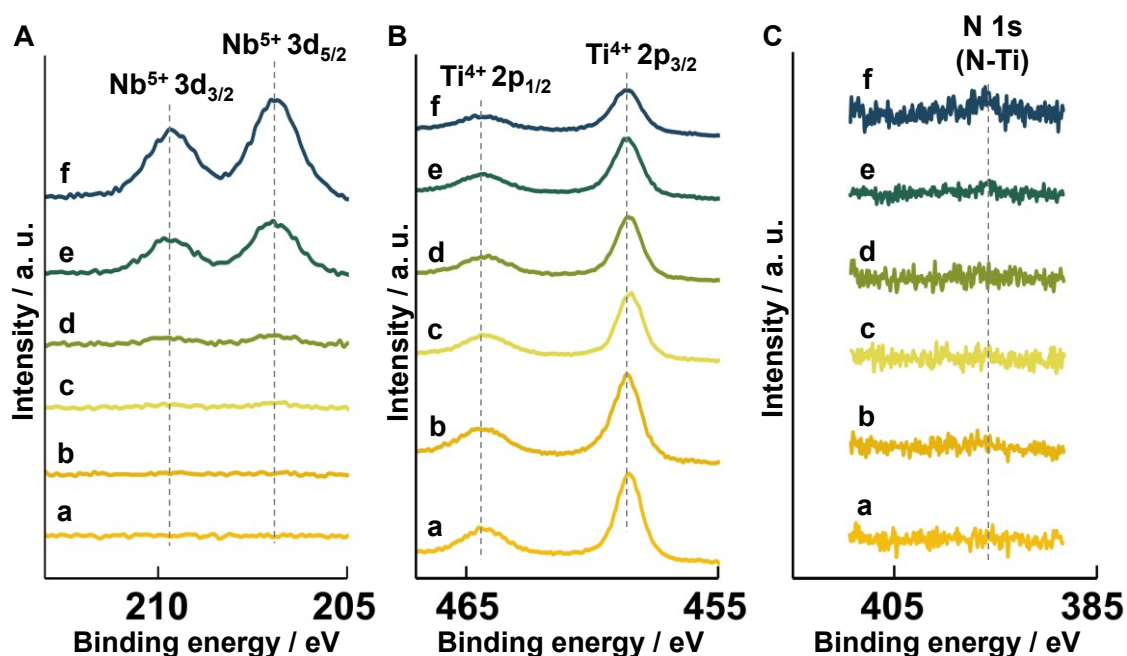

Figure 2-11. XPS spectra of (A) Nb, (B) Ti and (C) N in a) TiO_2 powder with no Nb content and Nb-doped TiO_2 powders with different Nb contents: b) 0.1, c) 0.5, d) 1, e) 5 and f) 10 mol% after the NH_3 annealing.

The Raman band at 141 cm^{-1}, observed in the spectrum of undoped TiO_2 nanopowder shifts to 142 cm^{-1} after NH_3 annealing and shifts further to higher wavenumbers with increases in the Nb content (Figure 2-9). An earlier report has ascribed this shift to oxygen vacancy formation in the anatase phase.[53] The formation of oxygen vacancies *via* NH_3 annealing can arise by two mechanisms: one is substitutional N-doping into the TiO_2 lattice at oxygen sites, and the other is reduction by H_2, which forms by decomposition of NH_3 at the annealing temperature.

When nitrogen is substitutionally doped into the TiO_2 lattice at oxygen sites, compensation of excess negative charge due to O^{2-} substitution by N^{3-} can occur by generating O^{2-} vacancies, and substitutional doping of nitrogen, as indicated by XPS analysis, thus likely involves oxygen vacancy formation. Alternatively, according to previous reports,[33,54] TiO_2 can be reduced by H_2 to form oxygen vacancies when TiO_2 powder is annealed under NH_3 at > *ca.* 550 °C. Based on this mechanism, since the Nb-doped TiO_2 nanopowders were annealed under reducing conditions, low-valent metal species such as Ti^{3+} or Nb^{4+} and oxygen vacancies are likely formed. Oxygen vacancy formation by similar mechanisms can be expected for rutile.

As shown in Figure 2-12 A, all samples became colored after NH_3 annealing, and the color changed from yellow to dark green with increases in the Nb content. Figure 2-11 B shows the diffused-reflectance UV-vis spectra of the samples after NH_3 annealing. UV-light absorption (- *ca.* 410 nm) (region I) and visible-light absorption (*ca.* 410 - *ca.* 520 nm) (region II) was observed in all samples, while visible-light absorption (*ca.* 520 nm -) (region III) was observed only in samples with ≥ 0.5 mol% Nb contents. The yellow color is due to absorption in visible light in region II (*ca.* 410 nm - *ca.*520 nm). The color became dark green with increases in the Nb content as a result of enhanced visible-light absorption in region III (≥ *ca.* 520 nm).

The light absorption edge in region I *ca.* 410 nm (*ca.* 3.0 eV) in all samples regardless of the Nb content, was the same as that before NH_3 annealing, indicating that the band gap of rutile is not narrowed *via* NH_3 annealing. Development of visible-light absorption in region II is common in interstitially N-doped TiO_2 which creates localized levels in the TiO_2 band gap,[33,54,55] while substitutional N-doping does not develop visible-light absorption.[55] Thus, the visible-light absorption in region II indicates that interstitial N-doping occurred regardless of the Nb content, although its presence was

not confirmed by XPS analysis. Which phase, anatase, rutile, or both, was involved for interstitial N-doping cannot be discussed.

Light absorption in region III was observed only for $\geq$ 0.5 mol% Nb contents, and is likely due to formation of Ti^{3+} *via* reduction of Ti^{4+} by H_2 to create a donor level below the conduction band of TiO_2.[34,54,56] Enhanced light absorption in region III with increased Nb content can be correlated with increases in the number of Ti^{3+} formed, as discussed above. Possible Nb^{4+} formation can be excluded from the mechanism of light absorption in region III, since it does not develop visible-light absorption in TiO_2.[57,58]

Bartlett *et al.* prepared Nb-doped TiO_2 with different Nb contents by the sol-gel method, which was subsequently annealed under NH_3 flow at 500 ^{o}C, but no enhancement of visible-light absorption in region III was observed regardless of the Nb content.[59] According to the previous report,[33,60] NH_3 decomposes into H_2 at above ~ 550 ^{o}C, and the absence of absorption in region III in the previous report is thus ascribable to the fact that NH_3 was not decomposed into H_2.
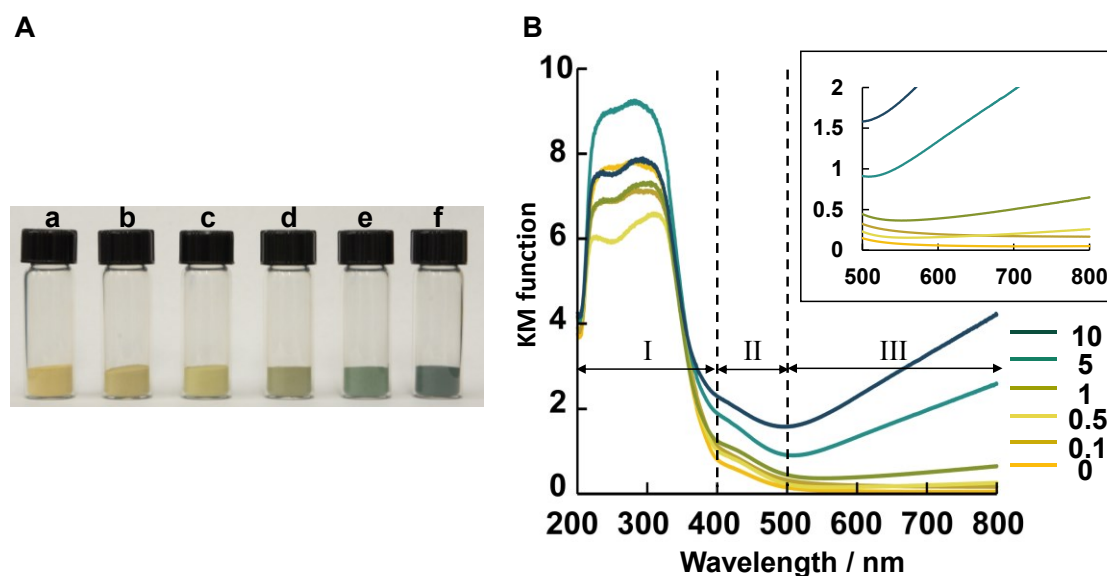

Fig. 2-12. (A) Photographic images of a) TiO_2 powder with no Nb content and TiO_2 with different Nb content: b) 0.1, c) 0.5, d) 1, e) 5 and f) 10 mol% after the NH_3 annealing. (B) Diffused-reflectance UV-vis spectra of undoped and Nb-doped TiO_2 powders with

different Nb contents after the NH_3 annealing. The inset shows the expanded version of the spectra in region III.

2-4. Conclusions

Nb-doped TiO_2 nanopowders with different Nb contents were synthesized by Liquid-feed Flame Spray Pyrolysis (LF-FSP) and subsequently annealed under NH_3 flow to develop and tune the visible-light absorption of TiO_2. Nb-doped TiO_2 nanopowders with different Nb contents were prepared by controlling the mixing ratios of chelated metal alkoxides precursors (titanatrane and niobatrane for Ti and Nb, respectively). The use of chelated metal alkoxides as Ti and Nb precursors was likely to be favorable to improving the Nb solubility limit in TiO_2. Nb-doping into TiO_2 nanopowders was demonstrated by compositional and crystal structural analyses. After the NH_3 annealing, white Nb-doped TiO_2 nanopowders became colored. This color change was attributable to interstitial N-doping, which was demonstrated by diffused-reflectance UV-vis spectroscopy. The color of the Nb-doped TiO_2 nanopowders after NH_3 annealing was varied from yellow to dark green depending on the Nb contents. This phenomenon is likely due to the localized levels created by interstitial N-doping and Nb-doping-induced Ti^{3+} level creation *via* reduction by H_2, which was formed as a result of NH_3 decomposition. Visible-light absorption by the interstitial N-doping, which corresponds to yellow coloration of TiO_2, was developed regardless of the Nb content, while that by Ti^{3+} level, which corresponds to blue coloration, was developed only in the samples with ≥ 0.5 mol% Nb contents, and the color of the samples thus varied from yellow to dark green depending on the Nb content. The methodology demonstrated in the present study to develop and tune the visible-light absorption of TiO_2 *via* synthesis of Nb-doped TiO_2 with different Nb contents by LF-FSP and subsequent NH_3 annealing has the potential to be applied in designing high-performance TiO_2 materials concerned with visible-light absorption, such as photocatalysts or pigments.

2-5. References

[1]   Pfaff, G.; Reynders, P. Angle-Dependent Optical Effects Deriving from Submicron Structures of Films and Pigments. *Chem. Rev.* **1999**, *99*, 1963–1982.

[2]   Fujishima, A.; Zhang, X.; Tryk, D. A. TiO_2 Photocatalysis and Related Surface Phenomena. *Surf. Sci. Rep.* **2008**, *63*, 515–582.

[3]   Chen, X.; Mao, S. S. Titanium Dioxide Nanomaterials : Synthesis , Properties, Modifications, and Applications. *Chem. Rev.* **2007**, *107*, 2891-2959.

[4]   O'Reagan, B.; Grätzel, M. A Low-cost, High-efficiency Solar Cell Based on Dye-Sensitized Colloidal TiO$_2$ Films. *Nature*, **1991**, *353*, 737-740.

[5]   Hagfeldt, A.; Boschloo, L.; Sun, L.; Kloo, L.; Pettersson, H. Dye-Sensitized Solar Cells. *Chem. Rev.* **2010**, *110*, 6595-6663.

[6]   Fine, G. F.; Cavanagh, L. M.; Afonja, A.; Binions, R. Metal Oxide Semi-Conductor Gas Sensors in Environmental Monitoring. *Sensors* **2010**, *10*, 5469–5502.

[7]   Hitosugi, T.; Yamada, N.; Nakao, S.; Hirose, Y.; Hasegawa, T. Properties of TiO$_2$-Based Transparent Conducting Oxides. *Phys. Status Solidi* **2010**, *207*, 1529–1537.

[8]   Macklin, W. J.; Neat, R. J. Performance of Titanium Dioxide-Based Cathodes in a Lithium Polymer Electrolyte Cell. *Solid State Ionics* **1992**, *53–56*, 694–700.

[9]   Zhu, G. N.; Wang, Y. G.; Xia, Y. Y. Ti-Based Compounds as Anode Materials for Li-Ion Batteries. *Energy Environ. Sci.* **2012**, *5*, 6652–6667.

[10]   Hurum, D. C.; Agrios, A. G.; Gray, K. A.; Rajh, T.; Thurnauer, M. C. Explaining the Enhanced Photocatalytic Activity of Degussa P25 Mixed-Phase TiO$_2$ Using EPR. **2003**, *107*, 4545–4549.

[11]   Kawahara, T.; Konishi, Y.; Tada, H.; Tohge, N.; Nishii, J.; Ito, S. A Patterned TiO$_2$ (Anatase)/TiO$_2$ (Rutile) Bilayer-Type Photocatalyst: Effect of the Anatase/Rutile Junction on the Photocatalytic Activity. *Angew. Chem.*, *Int. Ed.* **2002**, *41*, 2811–2813.

[12]   Zhang, J.; Xu, Q.; Feng, Z.; Li, M.; Li, C. Importance of the Relationship between Surface Phases and Photocatalytic Activity of TiO$_2$. *Angew. Chem.*, *Int. Ed.* **2008**, *47*, 1766–1769.

[13]   Li, G.; Rochter, C. P.; Milot, R. L.; Cai, L.; Schmuttenmaer, C. A.; Crabtree, R. H.; Brudvig, G. W.; Batista, V. S. Synergetic Effect between Anatase and Rutile TiO$_2$ Nanoparticles in Dye-Sensitized Solar Cells. *Dalton Trans.* **2009**, 10078–10085.

[14]   Savage, N.; Chwieroth, B.; Ginwalla, A.; Patton, B. R.; Akbar, S. A.; Dutta, P. K. Composite n-p Semiconducting Titanium Oxides as Gas Sensors. *Sensors Actuators B* Chemical **2001**, *79*, 17–27.

[15] Shen, J.; Wang, H.; Zhou, Y.; Ye, N.; Li, G.; Wang, L. Anatase/Rutile TiO$_2$ Nanocomposite Microspheres with Hierarchically Porous Structures for High-Performance Lithium-Ion Batteries. *RSC Adv.* **2012**, *2*, 9173-9178.

[16] Yamashita, H.; Ichihashi, Y.; Takeuchi, M.; Kishiguchi, S.; Anpo, M. Characterization of Metal Ion-Implanted Titanium Oxide Photocatalysts Operating under Visible Light Irradiation. *J. Synchrotron Radiat.* **1999**, *6*, 451–452.

[17] Iwasaki, M.; Hara, M.; Kawada, H.; Tada, H.; Ito, S. Cobalt Ion-Doped TiO$_2$ Photocatalyst Response to Visible Light. *J. Colloid Interface Sci.* **2000**, *224*, 202–204.

[18] Umebayashi, T.; Yamaki, T.; Itoh, H.; Asai, K. Analysis of Electronic Structures of 3d Transition Metal-Doped TiO$_2$ Based on Band Calculations. *J. Phys. Chem. Solids* **2002**, *63*, 1909–1920.

[19] Choi, J.; Park, H.; Hoffmann, M. R. Effects of Single Metal-Ion Doping on the Visible-Light Photoreactivity of TiO$_2$. *J. Phys. Chem. C* **2010**, *114*, 783–792.

[20] Das, C.; Roy, P.; Yang, M.; Jha, H.; Schmuki, P. Nb Doped TiO$_2$ Nanotubes for Enhanced Photoelectrochemical Water-Splitting. *Nanoscale* **2011**, *3*, 3094–3096.

[21] Lü, X.; Mou, X.; Wu, J.; Zhang, D.; Zhang, L.; Huang, F.; Xu, F.; Huang, S. Improved-Performance Dye-Sensitized Solar Cells Using Nb-Doped TiO$_2$ Electrodes: Efficient Electron Injection and Transfer. *Adv. Funct. Mater.* **2010**, *20*, 509–515.

[22] Furubayashi, Y.; Hitosugi, T.; Yamamoto, Y.; Inaba, K.; Kinoda, G.; Hirose, Y.; Shimada, T.; Hasegawa, T. A Transparent Metal: Nb-Doped Anatase TiO$_2$. *Appl. Phys. Lett.* **2005**, *86*, 252101.

[23] Fehse, M.; Cavaliere, S.; Lippens, P. E.; Savych, I.; Iadecola, A.; Monconduit, L.; Jones, D. J.; Rozière, J.; Fischer, F.; Tessier, C.; Stievano, L. Nb-Doped TiO$_2$ Nanofibers for Lithium Ion Batteries. *J. Phys. Chem. B* **2013**, *117*, 13827–13835.

[24] Laine, R. M. Liquid Feed-Flame Spray Pyrolysis (LF-FSP) in the Synthesis of Single- and Mixed-Metal Oxide Nanopowders. Ceramics Science and Technology, ed. R. Riedel and I. W. Chen, Wiley, Weinheim, 2011, vol. 3, ch. 4, pp. 97-116.

[25] Paulauskas, I. E.; Modeshia, D. R.; Ali, T. T.; El-Mossalamy, E. H.; Obaid, A. Y.; Basahel, S. N.; Al-Ghamdi, A. A.; Sartain, F. K. Photocatalytic Activity of Doped

and Undoped Titanium Dioxide Nanoparticles Synthesised by Flame Spray Pyrolysis. *Platin. Met. Rev.* **2013**, *57*, 32–43.

[26] Inturi, S. N. R.; Suidan, M.; Smirniotis, P. G. Influence of Synthesis Method on Leaching of the Cr-TiO$_2$ Catalyst for Visible Light Liquid Phase Photocatalysis and Their Stability. *Appl. Catal. B Environ.* **2016**, *180*, 351–361.

[27] Teleki, A.; Bjelobrk, N.; Pratsinis, S. E. Flame-Made Nb- and Cu-Doped TiO$_2$ Sensors for CO and Ethanol. *Sensors Actuators, B Chem.* **2008**, *130*, 449–457.

[28] Michalow, K. A.; Flak, D.; Heel, A.; Parlinska-Wojtan, M.; Rekas, M.; Graule, T. Effect of Nb Doping on Structural, Optical and Photocatalytic Properties of Flame-Made TiO$_2$ Nanopowder. *Environ. Sci. Pollut. Res.* **2012**, *19*, 3696–3708.

[29] Phanichphant, S.; Liewhiran, C.; Wetchakun, K.; Wisitsoraat, A.; Tuantranont, A. Flame-Made Nb-Doped TiO$_2$ Ethanol and Acetone Sensors. *Sensors* **2011**, *11* , 472–484.

[30] Yu, J. C.; Yu, J.; Ho, W.; Jiang, Z.; Zhang, L. Effects of F-doping on The Photocatalytic Activity and Microstructures of Nanocrystalline TiO$_2$ Powders. *Chem. Mater.* **2002**, 14, 3808–3816.

[31] Irie, H.; Watanabe, Y.; Hashimoto, K. Carbon-Doped Anatase TiO$_2$ Powders as a Visible-Light Sensitive Photocatalyst. *Chem. Lett.* **2003**, *32*, 772–773.

[32] Ohno, T.; Mitsui, T.; Matsumura, M. Photocatalytic Activity of S-doped TiO$_2$ Photocatalyst under Visible Light. **2003**, *32*, 364–365.

[33] Irie, H.; Watanabe, Y.; Hashimoto, K. Nitrogen-Concentration Dependence on Photocatalytic Activity of TiO$_{2-x}$N$_x$ powders. *J. Phys. Chem. B* **2003**, *107*, 5483–5486.

[34] Yi, E.; Wang, W.; Mohanty, S.; Kieffer, J.; Tamaki, R.; Laine, R. M. Materials That Can Replace Liquid Electrolytes in Li Batteries: Superionic Conductivities in Li$_{1.7}$Al$_{0.3}$Ti$_{1.7}$Si$_{0.4}$P$_{2.6}$O$_{12}$. Processing Combustion Synthesized Nanopowders to Free Standing Thin Films. *J. Power Sources* **2014**, *269*, 577–588.

[35] Bickmore, C. R.; Waldner, K. F.; Baranwal, R.; Hinklin, T.; Treadwell, D. R.; Laine, R. M. Ultrafine Titania by Flame Spray Pyrolysis of a Titanatrane Complex. *J. Eur. Ceram. Soc.* **1998**, *18*, 287–297.

[36] Bickmore, C. R.; Waldner, K. F.; Treadwell, D. R.; Laine, R. M. Ultrafine Spinel Powders by Flame Spray Pyrolysis of a Magnesium Aluminum Double Alkoxide. *J. Am. Ceram. Soc.* **1996**, *79*, 1419–1423.

[37] Sutorik, A.; Neo, S. Synthesis of Ultrafine β ″-Alumina Powders via Flame Spray Pyrolysis of Polymeric Precursors. *J. Am. Ceram. Soc.* **1998**, *81*, 1477–1486.

[38] Baranwal, R.; Villar, M. P.; Garcia, R.; Laine, R. M. Flame Spray Pyrolysis of Precursors as a Route to Nano-Mullite Powder : Powder Characterization and Sintering Behavior. *J. Am. Ceram. Soc.* **2001**, *84*, 951–961.

[39] Marchal, J.; Johns, T.; Baranwal, R.; Hinklin, T.; Laine, R. M. Yttrium Aluminum Garnet Nanopowders by Liquid-Feed Flame Spray Pyrolysis (LF-FSP) of Metalloorganic Precursors. *Chem. Mater.* **2004**, *16*, 822–831.

[40] Yi, E.; Wang, W.; Kieffer, J.; Laine, R. M. Flame Made Nanoparticles Permit Processing of Dense, Flexible, Li^+ Conducting Ceramic Electrolyte Thin Films of Cubic- $Li_7La_3Zr_2O_{12}$ (c-LLZO). *J. Mater. Chem. A* **2016**, *4*, 12947–12954.

[41] Roth, R. S. Thermal Stability of Long Range Order in Oxides. *Prog. Solid State Chem.* **1980**, *13*, 159–192.

[42] Griffith, K. J.; Senyshyn, A.; Grey, C. P. Structural Stability from Crystallographic Shear in TiO_2–Nb_2O_5 Phases: Cation Ordering and Lithiation Behavior of $TiNb_{24}O_{62}$. *Inorg. Chem.* **2017**, *56*, 4002-4010.

[43] Saeki, Y.; Matsushima, T. Decompositions of Niobium Pentachloride and Tantalum Pentachloride with Oxygen. *Denki Kagaku oyobi Kogyo Butsuri Kagaku* **1964**, *32*, 667-671.

[44] Ohsaka, T.; Izumi, F.; Fujiki, Y. Raman Spectrum of Anatase, TiO_2. *J. Raman Spectrosc.* **1978**, *7*, 321–324.

[45] Balachandran, U.; Eror, N. G. Raman Spectra of Titanium Dioxide. *J. Solid State Chem.* **1982**, *42*, 276–282.

[46] Rietveld, H. M. A Profile Refinement Method for Nuclear and Magnetic Structures. *J. Appl. Cryst.* **1969**, *2*, 65-71.

[47] Shannon, R. D. Revised Effective Ionic Radii and Systematic Studies of Interatomic Distances in Halides and Chalcogenides. *Acta Cryst.* **1976**. *A32*, 751-767.

[48] Ruiz, A. M.; Dezanneau, G.; Arbiol, J.; Cornet, A.; Morante, J. R. Insights into The Structural and Chemical Modifications of Nb Additive on TiO_2 Nanoparticles. *Chem. Mater.* **2004**, *16*, 862–871.

[49] Özer, N.; Rubin, M. D.; Lampert, C. M. Optical and Electrochemical Characteristics of Niobium Oxide Films Prepared by Sol-Gel Process and

Magnetron Sputtering A Comparison. *Sol. Energy Mater. Sol. Cells* **1996**, *40*, 285–296.

[50] Bert, I.; Mohai, M.; Sullivan, J. L.; Saied, S. O. Surface Characterisation of Plasma-Nitrided Titanium: an XPS Study. *Appl. Surf. Sci.* **1995**, *84*, 357–371.

[51] Kong, L.; Wang, C.; Zheng, H.; Zhang, X.; Liu, Y. Defect-Induced Yellow Color in Nb-doped TiO_2 and Its Impact on Visible-Light Photocatalysis. *J. Phys. Chem. C* **2015**, *119*, 16623–16632.

[52] Asahi, R.; Morikawa, T.; Ohwaki, T.; Aoki, K.; Taga, Y. Visible-Light Photocatalysis in Nitrogen-Doped Titanium Oxides. *Science* **2001**, *293*, 269–271.

[53] Li, J.-G.; Büchel, R.; Isobe, M.; Mori, T.; Ishigaki, T. Cobalt-Doped TiO_2 Nanocrystallites: Radio-Frequency Thermal Plasma Processing, Phase Structure, and Magnetic Properties. *J. Phys. Chem. C* **2009**, *113*, 8009–8015.

[54] Petala, A.; Tsikritzis, D.; Kollia, M.; Ladas, S.; Kennou, S.; Kondarides, D. I. Synthesis and Characterization of N-Doped TiO_2 Photocatalysts with Tunable Response to Solar Radiation. *Appl. Surf. Sci.* **2014**, *305*, 281–291.

[55] Valentin, C. D.; Finazzi, E.; Pacchioni, G.; Selloni, A.; Livraghi, S.; Paganini, M. C.; Giamello, E. N-Doped TiO_2: Theory and Experiment. *Chem. Phys.* **2007**, *339*, 44–56.

[56] Valentin, C. D.; Pacchioni, G.; Selloni, A. Reduced and n-type Doped TiO_2: Nature of Ti^{3+} species. *J. Phys. Chem. C*, 2009, *113*, 20543–20552.

[57] Claverie, J.; Verniolle, J.; Campet, G.; Doumerc, J. P.; Hagenmuller, P. Visible-light Response of Ni^{2+} and Nb^{4+} doped-polycristalline TiO_2 Anodes. *Mater. Res. Bull.* **1981**, *16*, 1019–1025.

[58] Liu, M.; Qiu, X.; Hashimoto, K.; Miyauchi, M. Cu(II) Nanocluster-Grafted, Nb-Doped TiO_2 as an Efficient Visible-Light-Sensitive Photocatalyst Based on Energy-Level Matching Between Surface and Bulk States. *J. Mater. Chem. A* **2014**, *2*, 13571-13579.

[59] Breault, T. M.; Bartlett, B. M. Composition Dependence of TiO_2:(Nb,N)-X Compounds on the Rate of Photocatalytic Methylene Blue Dye Degradation. *J. Phys. Chem. C* **2013**, *117*, 8611–8618.

[60] Shin, C. H.; Bugli, G.; Djega-Mariadassou, G. Preparation and Characterization of Titanium Oxynitrides with High Specific Surface Areas. *J. Solid State Chem.* **1991**, *95*, 145-155.

CHAPTER 3

High-performance Heterojunction Creation by Simple Integration of Protonated Layered Titanate with TiO$_2$ Nanoparticles

3. High-performance Heterojunction Created by Simple Integration of Protonated Layered Titanate with TiO₂ Nanoparticles

3-1. Introduction

Development of highly active solid photocatalysts has been extensively investigated for efficient use of solar energy for fuel production, fine chemical synthesis and removal of hazardous organic compounds.[1-5] Extensive efforts have been directed to modifying existing photocatalysts and synthesizing new ones in consideration of an increase in their surface areas and enhancement of their charge separation efficiency, since these factors largely affect the activities of photocatalyst particles. Layered inorganic semiconductors such as layered titanates and niobates have been utilized as scaffolds for designing highly efficient photocatalysts, because they possess an interlayer space that is expandable *via* intercalation reactions and can therefore provide huge nanospaces for reactants and functional units for semiconductor-based heterojunction creation.[6-8] A representative example is the enhanced photocatalytic activity observed for photocatalysts with heterojunctions created *via* layer-by-layer assembly of two kinds of layered semiconductor nanosheets resulting from enhanced charge-separation efficiency due to efficient coupling based on their 2D structures.[9,10] In addition, with tuning of their interlayer structures, they show such unique and useful phenomena as substrate- or product- selective photocatalytic reactions[11-15] that are difficult to achieve with conventional semiconducting particles. Unmodified layered inorganic semiconductors, however, show negligible photocatalytic activity;[11,13] as a result, the obtained photocatalysts with heterojunctions show photocatalytic activity lower than that of such commercial photocatalysts as P25 TiO₂ which is often used as a benchmark photocatalyst. Achieving remarkable enhancement of the photocatalytic activity of layered inorganic semiconductors more easily and inexpensively without intercalation reactions is thus a challenging issue.[16]

Herein, a new methodology for remarkably enhancing the photocatalytic activity of layered inorganic semiconductors by making unique use of P25 is

reported. A lepidocrocite-type layered titanate ($A_xTi_{2-y}M_yO_4$: A, interlayer alkali metal cation; M, metal or vacancy) was selected to enhance the photocatalytic activity, since lepidocrocite-type layered titanates have widely been investigated due to their superior intercalation abilities.[17] P25 is one of the most active photocatalysts; therefore, the modification of P25 with co-catalysts has been conducted to synthesize photocatalysts with high activity levels.[16,18,19] It is demonstrated that simple (particle-level) mixing of a layered titanate and a much smaller amount of P25 (as a kind of co-catalyst) produces a composite showing considerably higher photocatalytic activity than P25 for different reactions as a result of a transfer of photoexcited electrons from the layered titanate to P25 *via* a heterojunction and retardation of the charge recombination, without intercalation reactions. A high level (apparent quantum yield of 73% at 320 nm) of photocatalytic activity for H_2 evolution from an aqueous methanol solution is achieved when the P25 component is replaced with Pt-loaded P25, although an unusually small amount of Pt is used in the composite.

3-2. Experimental

Reagents and materials

K_2CO_3 (>99.95 %), Li_2CO_3 (>99.95 %), HCl (35.0-37.0 %) and methanol (>99.5 %) were purchased from Kanto Chemical Co., Inc. Formic acid (99.0 %), Nitro Blue Tetrazolium Chloride (NBT) and $H_2PtCl_6 \cdot 6H_2O$ (99.9 %) were purchased from Wako Pure Chemical Industry, Ltd. WO_3 (> 99.0 %) was purchased from Kishida Chemical Co., Ltd. P25 (>95.0 %) was supplied by Nippon Aerosil Co., Ltd. All reagents and materials were used as received.

Characterization

X-ray diffraction (XRD) patterns of the samples were collected using a powder X-ray diffractometer (Smart Lab, RIGAKU) with Cu Kα radiation at 40 kV and 30 mA. The crystal morphology was observed with a field-emission scanning electron microscope (FE-SEM) (JEOL JEM-6500F). Agglomerate size distribution was determined by dynamic light scattering (DLS) using a Nanotrac Wave (Microtrac Bel Corp.) Transmission electron microscopic (TEM) images were obtained with a JEOL

JEM-6500F equipped with an energy dispersive X-ray spectroscopy (EDS) analyzer. Inductivity-coupled plasma atomic emission spectroscopy (ICP-AES) was performed on an Agilent 710-ES. Each sample (6.0 mg) was decomposed for measurement with 12 M H_2SO_4 (5.0 mL) at 200 ^{o}C for 3 h. UV-vis spectra were obtained with a JASCO V-750 spectrophotometer.

Preparation of HTO

$H_{1.07}Ti_{1.73}\square_{0.27}O_4$ (referred to as "HTO", equivalent to $H_{1.07}Ti_{1.73}O_4$; $\square$ denotes a defect) was prepared by a solid-state reaction and subsequent acid treatment. $K_{0.8}Ti_{1.73}Li_{0.27}O_4$ (KTLO) was prepared according to the previous report[20] by solid-state reaction from K_2CO_3, Li_2CO_3 and TiO_2 (at the molar ratio of 2.4:0.8:10.4). The starting materials were mixed using a planetary ball mill (Planet M2-3, Gokin Planetaring) and the mixture was calcined in air at 600 ^{o}C for 30 min, and then calcined for another 20 h after grinding. KTLO (400 mg) was dispersed in 0.1 M HCl (200 mL) and the dispersion was shaken (160 rpm, 12h). The reaction was conducted three times. The solid was separated by centrifugation (3500 rpm, 20-60 min), washed with deionized water, and dried under reduced pressure at room temperature.

Photocatalytic oxidative decomposition of formic acid

Oxidative decomposition of formic acid[21,22] was performed in a stainless-steel container (75 mL) equipped with a Pyrex window as follows: the sample (layered titanate or both layered titanate and additive powders) was added in an O_2-saturated aqueous solution (5 mL) containing 5 vol% of formic acid, and the suspension was sonicated for 1 min and then irradiated using a solar simulator (San-Ei Electric, λ >300 nm, 1000 Wm^{-2} (1 solar)) under stirring. The gas in the glass tube was collected with a gas-tight syringe and quantified using a Barrier Ionization Discharge (BID) gas chromatograph (ShimadzuBID-2010 plus) equipped with a Micropacked ST column. Argon gas was used as a carrier gas.

Quantitative analysis of O_2^-

O_2^- yields of the photocatalysts were quantified according to the previous report.[23] HTO (15 mg), P25 (2 mg) or an HTO/P25 mixture (13 mg/2 mg) was dispersed in an aqueous 2-propanol solution (5 mL, 4 vol%, O_2 saturated), to which NBT had been added at a concentration of 1 mM, by sonication. The suspension was irradiated with a 350-W mercury lamp (USHIO Inc.) (>300 nm) for 3 min. This reaction was conducted in a glass tube. After irradiation, the photocatalyst was removed by centrifugation (45000 rpm, 15 min), and the supernatant was analyzed by UV-vis spectrometer (Shimadzu UV-3100PC). NBT reacts with O_2^-, generated by a reaction between O_2 and photoexcited electrons of a photocatalyst, at a molar ratio of 1:4 to form insoluble Formazan deposits on the photocatalyst, as shown in Figure 3-1.[23] Therefore, by quantifying the amount of NBT recovered from the aqueous dispersion, the amount of generated O_2^- can be quantified.
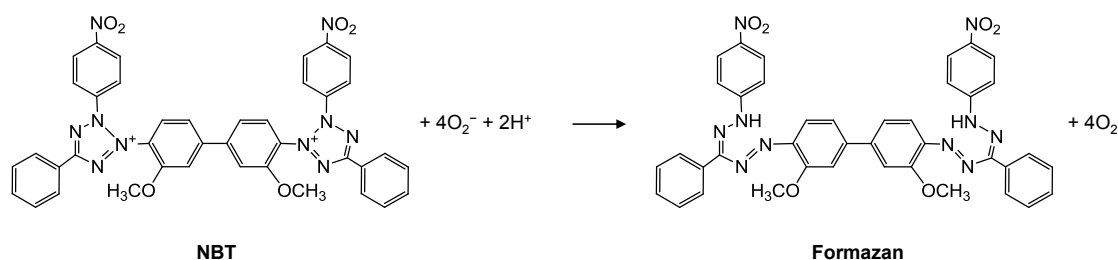
Figure 3-1. Reaction between NBT and O_2^-.

Determination of the oxidation site in a HTO/P25 composite

The oxidation site in an HTO/P25 composite was determined according to the previous report.[24] The HTO/P25 mixture (15 mg) was dispersed in a 0.1 M $Pb(NO_3)_2$ aqueous solution (5 mL, O_2 saturated) by sonication in a glass tube. The pH of the dispersion was adjusted to 1.0 by adding HNO_3. After photoirradiation (>300 nm) for 24 hours, the solid was separated by centrifugation (3500 rpm, 20 min) and dried under reduced pressure at room temperature. The sample (1 mg) was dispersed in ethanol (1 mL) by sonication, and a carbon-coated TEM grid (Ouken-Shoji, 200-A mesh) was dipped in the dispersion followed by drying at room temperature for TEM-EDS observation.

Preparation of Pt-loaded photocatalysts

Pt-loaded photocatalysts were prepared according to the method used in the previous report.[25] The sample was suspended in an aqueous methanol solution (5 mL, 1/1 in V/V) in a Pyrex glass tube (34 mL), and $H_2PtCl_6 \cdot 6H_2O$ (Pt/sample = 0.5 wt%) was added to the suspension. The resulting suspension was sonicated for 1 min and then deaerated by argon bubbling. The glass tube was sealed with a rubber septum and irradiated with an ultra-high-pressure mercury lamp (350 W, Ushio Inc.) under stirring for 10 min. The solid was separated by centrifugation (3500 rpm, 20 min), washed with water, and dried under reduced pressure at room temperature.

Photocatalytic H_2 evolution

Photocatalytic H_2 evolution from water was performed in a Pyrex glass tube (34 mL) as follows: the sample (layered titanate or both layered titanate and additive powders) was added to an aqueous methanol solution (5 mL, 1/1 in V/V), and the suspension was sonicated for 1 min and then deaerated by argon bubbling.[25] The glass tube was sealed with a rubber septum and irradiated with a solar simulator (San-Ei Electric, λ >300 nm, 1000 Wm^{-2} (1 solar)) under stirring. For apparent quantum yield (AQY) calculation,[2] the glass tube was irradiated with a monochromated light (320 nm) for 3 h using a 500-W Xe lamp (Ushio Inc.) and SM-25 monochrometer (Bunkoukeiki). The gas in the glass tube was collected with a gas-tight syringe and quantified using a TCD gas chromatograph (Shimadzu GC-8A) equipped with SHINCARBON-ST 50-80 columns. Argon gas was used as a carrier gas. The H_2 concentrations were calibrated with an authentic sample. The number of incident photons was determined using an S1337-1010BQ silicon photodiode (Bunkoukeiki). AQY was defined by the following equation[2]:

$$AQY\ (\%) = \frac{\text{Number of reacted electrons}}{\text{Number of incident photons}} \times 100\ \%$$

$$= \frac{\text{Number of evolved } H_2 \text{ molecules} \times 2}{\text{Number of incident photons}} \times 100 \%$$

3-3. Results and Discussion

3-3-1. Preparation of a Layered Titanate

XRD patterns of the sample after the solid-state reactions are shown in Figure 3-2 A. The diffraction peaks at 2θ (CuKα) = 11.3°, 22.6°, 24.0°, 29.0°, 32.2°, 34.6°, 38.2°, 42.3°, 46.4°, 47.5° and 49.0° were indexed to the (020), (040), (110), (130), (021), (060), (041), (131), (061), (200) and (151) planes of KTLO, respectively.[26] Figure 3-2 B shows XRD patterns of the sample obtained after acid treatment of KTLO. The diffraction peaks at 2θ (CuKα) = 9.4°, 18.8°, 23.8°, 27.5°, 28.7°, 33.2°, 38.7°, 45.8°, 47.8° and 48.8° were indexed to the (020), (040), (110), (130), (060), (031), (041), (051), (071), (200) and (151) planes of HTO, respectively.[26] The increase in (020) d-spacing from 0.78 nm to 0.92 nm is ascribable to the fact that interlayer K^+ was replaced by H^+, since H^+ is hydrated more efficiently than K^+ to expand the interlayer space.[26]

The acid-treated KTLO did not contain K and Li, as confirmed by ICP-AES analysis (data not shown). This is ascribable to the fact that almost all the interlayer K ions and framework Li ions were extracted during the acid treatment. The structural and compositional analyses thus revealed the formation of HTO by acid treatment of KTLO.

Figure 3-3 shows SEM images of the samples. KTLO consisted of rounded rectangular particles (70–100 nm) with smooth surfaces (Figure 3-3 A). The HTO appears similar to KTLO, with some particle fragments on the edges of the particles (Figure 3-3 B).
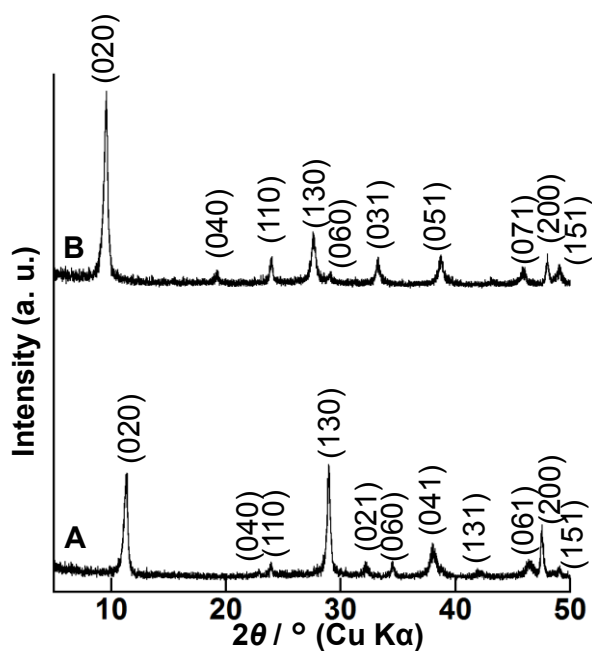
Figure 3-2. The XRD patterns of (A) KTLO and (B) HTO.
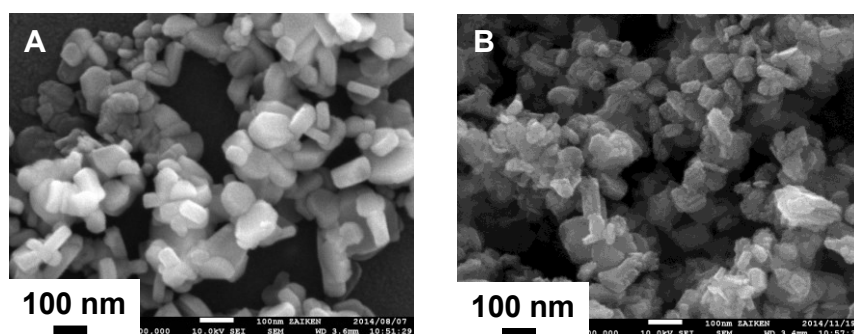
Figure 3-3. The SEM images of (A) KTLO and (B) HTO.

3-3-2. Mixing of HTO with P25

Figure 3-4 shows the agglomerate size distribution of HTO, P25 and the HTO/P25 mixture in water determined by DLS analysis. HTO and P25 showed peaks with a size of *ca.* 1.3 μm and *ca.* 0.3 μm, respectively. They were assigned to aggregated particles, since the primary particle sizes of HTO and P25 were *ca.* 100-200 nm and *ca.* 20-50 nm, respectively. The HTO/P25 mixture showed a peak with a size of 2.2 μm, which was much larger than those of HTO and P25.

In the TEM image of the HTO/P25 mixture after the evaporation of water, it was found that HTO and P25 possessed particle interfaces (Figure 3-5). These results indicate that HTO and P25 particles can contact each other when mixed in water to create heterojunctions.
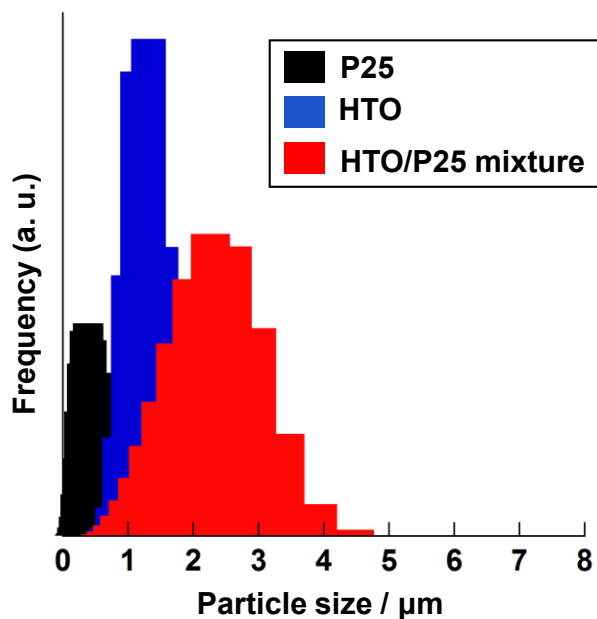
Figure 3-4. Agglomerate size distribution determined by DLS of P25 (13 mg), HTO (2 mg) and HTO/P25 mixture (13 mg/2 mg) suspended in water (5 mL).
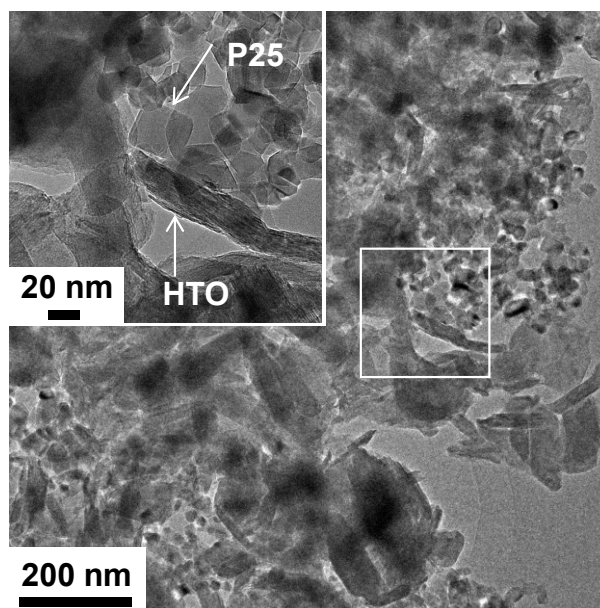
Figure 3-5. TEM image of the HTO/P25 mixture (13 mg/2 mg) suspended in water (5 mL) after evaporation of water.

3-3-3. Enhanced Photocatalytic Formic Acid Oxidation and the Mechanism

As shown in Figure 3-6, P25 decomposed formic acid photocatalytically to generate CO_2, as reported previously.[27] HTO was completely inactive for the reaction. On the other hand, the HTO/P25 composite showed about five times higher activity than P25.

Figure 3-7 shows the photocatalytic activity of HTO/P25 composite with different HTO/P25 mixing ratios. The HTO/P25 composite (13 mg/2 mg) showed the highest photocatalytic activity, and the mixing ratio was thus optimized at 13 mg/2mg.

P25 is one of the most active photocatalysts for the decomposition of organic compounds, and only a limited number of TiO_2 materials have shown photocatalytic activity considerably higher than that of P25.[25,28,29] The photocatalytic activity of the HTO/P25 composite was comparable to that of hydrothermally treated P25,[30] which, to the best of my knowledge, shows the best photocatalytic activity for oxidative decomposition of formic acid among unmodified TiO_2 photocatalysts. The photocatalytic activity of the HTO/P25 composite, moreover, was higher than that of Pt@HTO, an HTO with its outer

particle surface modified with 0.5 wt% Pt nanoparticle, one of the most efficient co-catalysts (Figure 3-6). All the results indicate the merits of using P25 as an additive for simple, low-cost development of high photocatalytic activity in HTO and many other layered inorganic semiconductors with electronic band structures similar to that of HTO.[31]
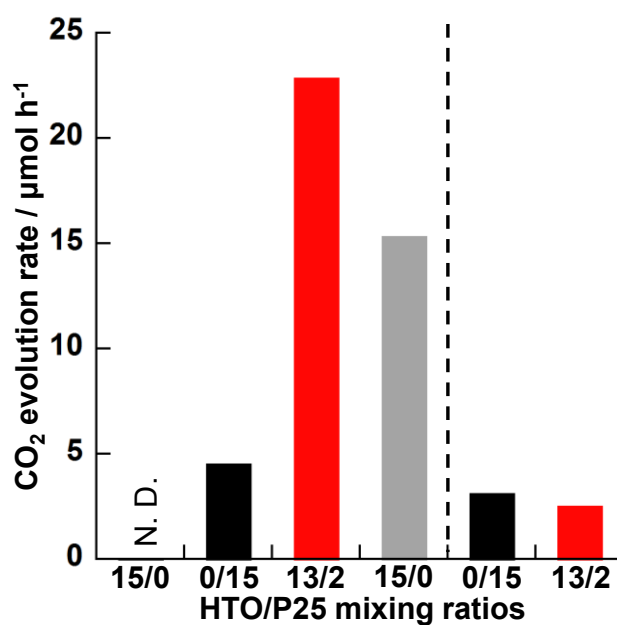
Figure 3-6. CO_2 evolution rates at different HTO/P25 (mg/mg) mixing ratios under simulated solar light (left) $\lambda > 300$ nm and (right) $\lambda > 370$ nm. The gray bar indicates the CO_2 evolution rates for Pt@HTO.
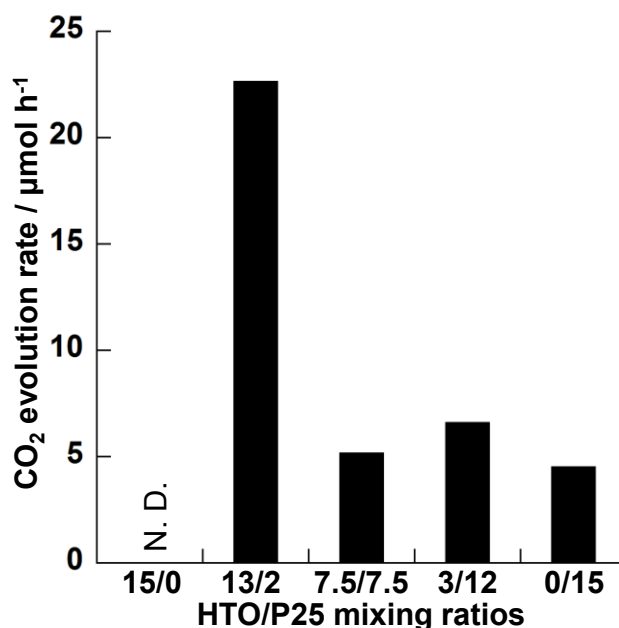
Figure 3-7. CO_2 evolution rates at different HTO/P25 (mg/mg) mixing ratios under simulated solar light (>300 nm).

To discuss the mechanism of the high photocatalytic activity of the HTO/P25 composites, a photocatalytic reaction under simulated solar light with a wavelength of $\lambda > 370$ nm, at which HTO is not excited but P25 is (Figure 3-8), was conducted first. As shown in Figure 3-6, the photocatalytic activity of the mixture was similar to that of P25 under these conditions. In light of the fact that formic acid is decomposed directly by photogenerated holes in TiO_2 (or the decomposition is initiated by the holes) in the presence of molecular O_2,[32] this result indicates that under full-spectrum solar light irradiation, electron transfer from P25 to HTO *via* heterojunction scarcely occurs to enhance the photocatalytic activity of P25. It is thus suggested that HTO, which is inactive without P25 because the photogenerated electron-hole pairs are easily recombined (possibly due to its low crystallinity and/or low O_2 reduction ability, as discussed later), shows extremely enhanced activity as a result of a charge transfer from HTO to P25 to retard the charge recombination on HTO. In the previous report,[13] although a lepidocrocite-type layered titanate showed scarcely any photocatalytic activity for the decomposition of alcohols to H_2, it did show

54

photocatalytic activity after modification of the outer particle surface with Pt. This observation supports our hypothesis.
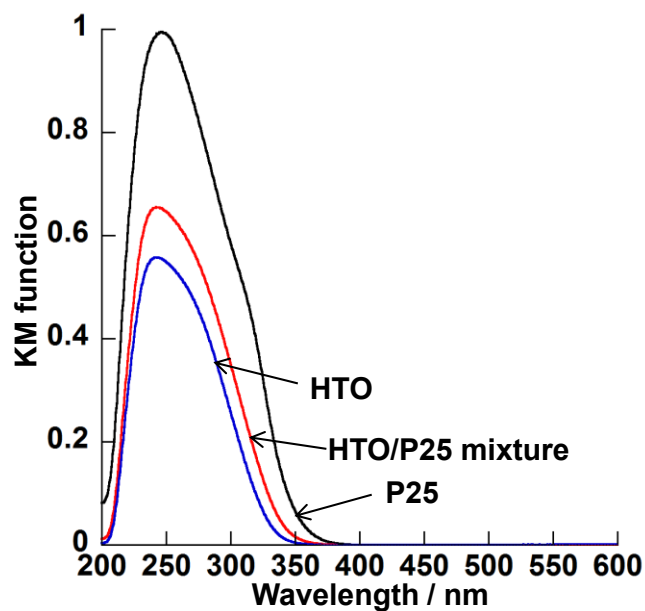
Figure 3-8. Diffused-reflectance UV-vis spectra of samples.

Considering the electronic band structures of HTO and P25 (Figure 3-9),[33,34] both electron and hole transfer from photoexcited HTO to P25 are thermodynamically favorable, and P25 can thus enhance the charge separation of HTO.
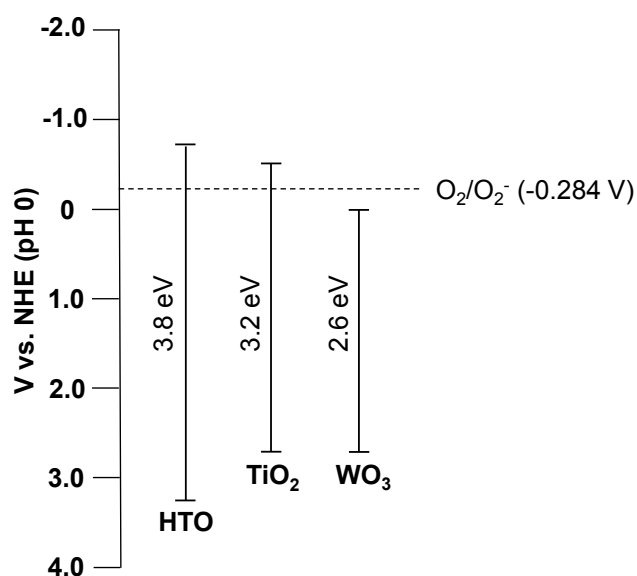
Figure 3-9. Electronic band structures of semiconductors used in this study determined on the basis of Ref. 1, 33 and 34.

To investigate photoexcited electron transfer *via* heterojunction, the O_2^- yield was monitored by a method proposed by Matsumura, *et al.*,[23] who had quantified the O_2^- yield of TiO_2 using NBT, which reacts with O_2^-, generated by a reaction between O_2 and photoexcited electrons of a photocatalyst, to form insoluble Formazan deposits on TiO_2. As shown in Figure 3-10, in the case of P25 and the HTO/P25 composite, the color of the dispersion changed visibly from yellow to purple, indicating the formation of O_2^- which reacted with NBT to form Formazan.[23] On the other hand, the color of the HTO dispersion did not change *via* UV-light irradiation, indicating that HTO did not generate O_2^-. Figure 3-11 shows the absorption spectra of an 1 mM NBT aqueous solution and those after UV-light irradiation with different samples. Absorbance of an aqueous NBT solution decreased *via* UV-light irradiation in the case of P25 and the HTO/P25 composite, and absorbance was lower for the HTO/P25 composite than for P25. Considering that the color of the dispersion changed from yellow to purple, this result indicates that both P25 and the HTO/P25 composite generated O_2^- and that the amount of O_2^- generated by the HTO/P25 composite was larger than that generated by P25. The constant absorbance of HTO further indicates that O_2^- was not generated by HTO. The O_2^- generation rates of different samples calculated using the absorbance are shown in Figure 3-12. The HTO/P25 composite

generated an approximately three times higher amount of O_2^- than P25 alone. This result confirms that photoexcited electrons are transferred from HTO to P25, and that the O_2 on the surface of P25 is subsequently reduced. The fact that efficient charge separation occurred in P25 *via* inter-particle electron transfer between rutile and anatase[30,35] suggests remarkably enhanced charge separation efficiency on the HTO/P25 composite. Since the optical spectrum of light used in quantitative analysis of O_2^- is different from that used in photocatalytic oxidative decomposition of formic acid, the number of photoecxited electrons calculated from the generated O_2^- is not comparable to that of holes calculated from the evolved CO_2.
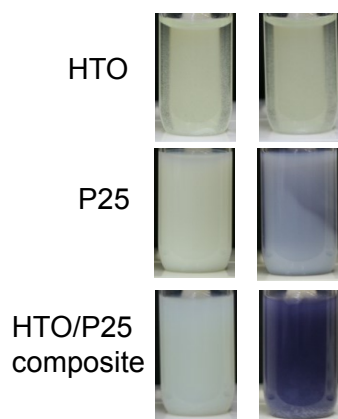
Figure 3-10. Photographic images of dispersions of different samples (left) before and (right) after UV-light irradiation.
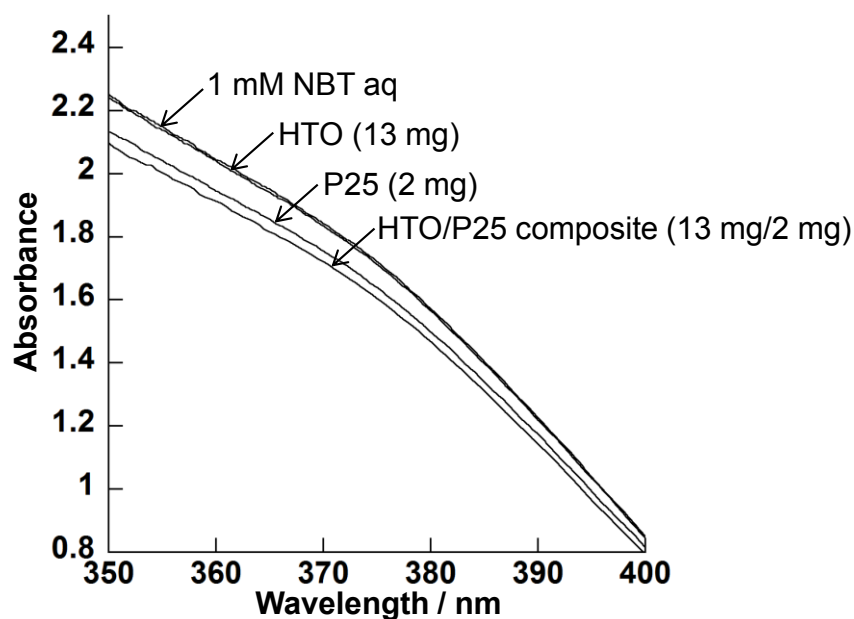
Figure 3-11. UV-vis absorption spectra of 1 mM NBT aqueous solution and supernatant following removal of different samples after UV-light irradiation.
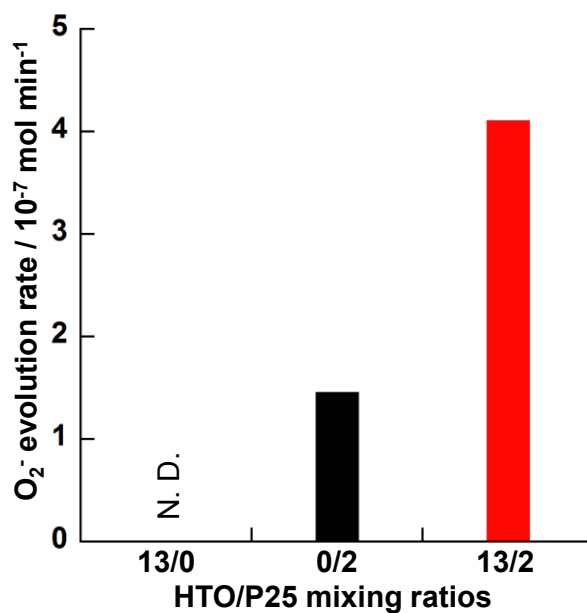
Figure 3-12. O_2^- evolution rates at different HTO/P25 (mg/mg) mixing ratios.

To further confirm the photoexcited electron transfer from HTO to P25 *via* heterojunctions, the photocatalytic activity of the HTO/WO_3 mixture, in which transfer of both photogenerated electrons and holes from HTO to WO_3 is possible judging from the electronic band structures of HTO and WO_3 (Figure 3-9), was examined. The HTO/WO_3 mixture showed much lower photocatalytic activity

compared to the HTO/P25 composite (Figure 3-13). If the main reason for the high photocatalytic activity of the HTO/P25 composite was hole transfer between them, high photocatalytic activity should also be observed for the HTO/WO$_3$ mixture. A poor O$_2$ reduction ability of WO$_3$, due to the fact that the conduction band potential of WO$_3$ is more positive than the potential for single-electron reduction of O$_2$,[1,36] cannot be excluded as a mechanism for the unenhanced photocatalytic activity of HTO upon mixing with WO$_3$.
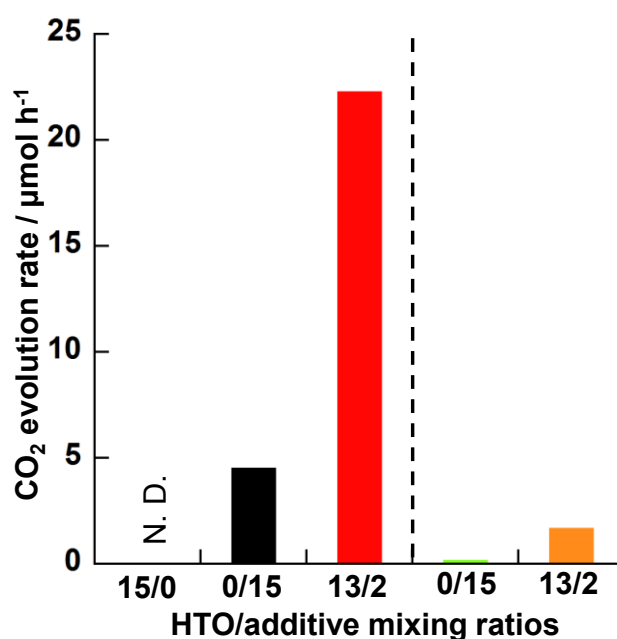
Figure 3-13. CO$_2$ evolution rates at different (left) HTO/P25 (mg/mg) mixing ratios and (right) HTO/WO$_3$ (mg/mg) mixing ratios.

Possible transfer of photogenerated holes from HTO to P25, resulting in retardation of the charge recombination on HTO and enhancement of the photocatalytic activity, was also studied. It is known that PbO$_2$ is deposited on photocatalyst particles from Pb^{2+} by oxidation with photogenerated holes, and this phenomenon has been used to determine the oxidation sites of photocatalyst particles.[24] Figure 3-14 shows XRD patterns of the HTO/P25 composite (13 mg/2 mg) before and after UV-light irradiation. In the XRD pattern of the sample before UV-light irradiation, the diffraction peaks at 2θ (CuKα) = 10.1° and 27.4° were indexed to the (020) and (130) planes of HTO, and those at 2θ (CuKα) =

25.2°, 37.7° and 48.0° were indexed to the (101), (004) and (200) planes of anatase, the main component of P25. On the other hand, in the XRD pattern of the sample after UV-light irradiation, the diffraction peaks at 2θ (CuKα) = 19.5°, 22.5° and 38.5° were indexed to the (111), (200) and (222) planes of $Pb(NO_3)_2$, and those at 2θ (CuKα) = 32.1° and 49.4° were indexed to the (101) and (200) planes of PbO_2. Although peaks due to PbO_2 were observed in the XRD pattern of the HTO/P25 composite after UV-light irradiation, PbO_2 nanoparticles were not observed on P25 particles adjacent to HTO particles in the TEM image (Figure 3-15). No further formation of PbO_2 on the P25 component was confirmed by the TEM elemental mapping, as shown in Figure 3-16. These results indicate that Pb^{2+} was not oxidized on P25 but was oxidized in the interlayer space of HTO, confirming that hole transfer from HTO to P25 *via* heterojunction had not occurred (the possibility that quite small PbO_2 particles formed on the outer surface of HTO particles cannot be ruled out).
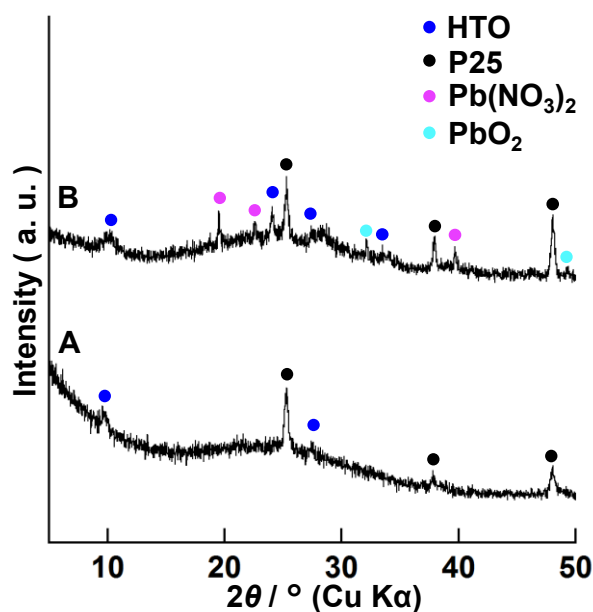
Figure 3-14. XRD patterns of HTO/P25 mixture (13 mg/2 mg) (A) before and (B) after UV-light irradiation in $Pb(NO_3)_2$ aqueous solution.
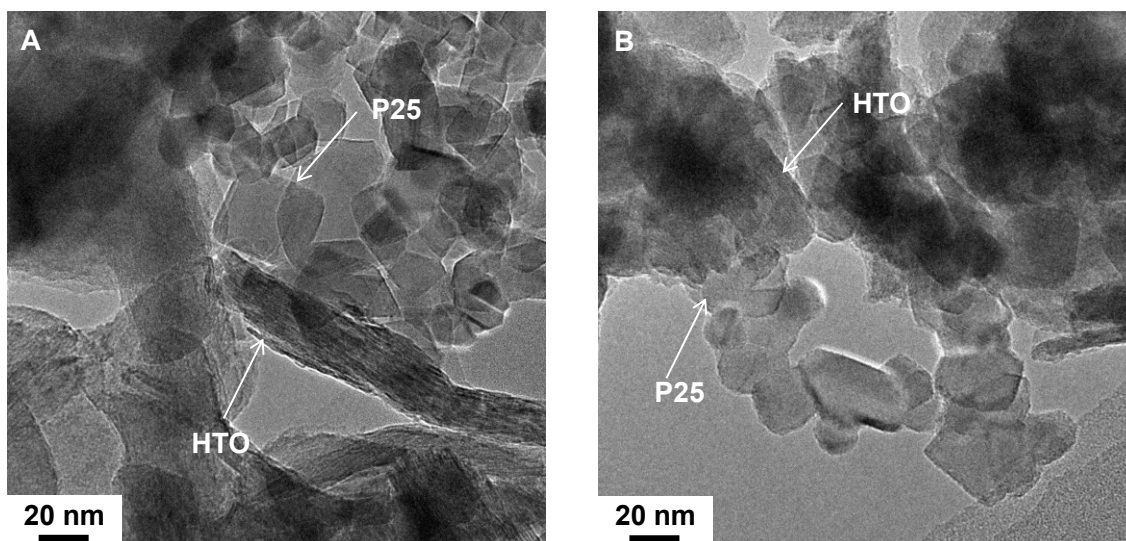
Figure 3-15. TEM images of HTO/P25 mixture (13 mg/2 mg) (A) before and (B) after UV-light irradiation in a Pb(NO$_3$)$_2$ aqueous solution.
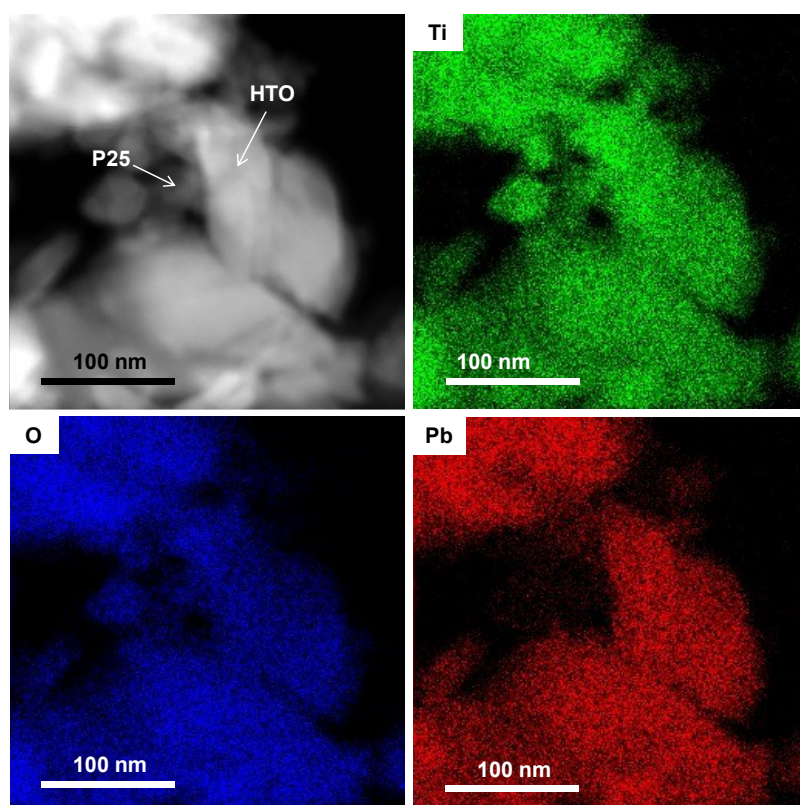
Figure 3-16. TEM image and the corresponding elemental mappings of HTO/P25 mixture (13 mg/2 mg) after UV-light irradiation in a Pb(NO$_3$)$_2$ aqueous solution.

Accordingly, the photocatalytic activity developed in HTO, in which photogenerated electrons and created holes are likely to be recombined easily (Figure 3-17 A), is ascribable to photoexcited electron transfer from HTO to P25 and subsequent enhancement of the charge separation efficiency of HTO (Figure 3-17 B).
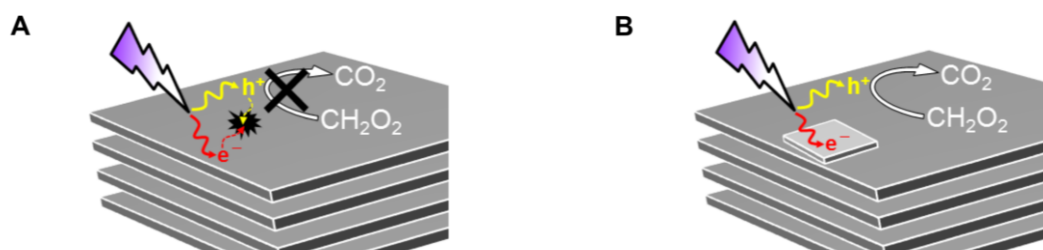
Figure 3-17. Scheme for photocatalytic reactions on (A) HTO and (B) the HTO/P25 composite.

3-3-4. Photocatalytic H_2 Evolution from an Aqueous Methanol Solution

Based on the above mechanism, it was assumed that the photocatalytic activity of HTO for reduction reactions can also be enhanced upon mixing with P25 particles. Therefore, the photocatalytic activity of the HTO/P25 composite for H_2 evolution from water, one of the most desired reactions for fuel production, was demonstrated. As shown in Figure 3-18 A, H_2 evolved linearly with irradiation time in all the samples except for P25, a result consistent with the previous report, which showed negligible activity of P25 under similar conditions.[25] Upon mixing with P25 particles, the photocatalytic activity of HTO was considerably enhanced (*ca.* 600 %), as expected (Figure 3-18 B). The AQY of the composite at 320 nm was 23 %. When P25 was replaced with 0.5 wt% of Pt nanoparticle-modified P25 (Pt@P25), the activity was further enhanced by up to 3100 % and the AQY reached 73 % at 320 nm (at 3 h irradiation in Figure 3-19). This enhanced activity was ascribable to enhanced charge separation due to integration with P25 resembling to photocatalytic formic acid oxidation on the HTO/P25 composite, in addition to the presence of a Pt co-catalyst for H_2 evolution. It should be noted that the photocatalytic activity of the HTO/Pt@P25 composite was even higher than that of Pt@P25 with the same amount of catalyst

(15 mg), although the amount of Pt contained in the HTO/Pt@P25 system was only 0.06 wt%, which was much smaller than that (0.5 wt%) contained in the Pt@P25 sole system. Intercalation of appropriate visible light sensitizers into the HTO component might allow more efficient utilization of solar energy.
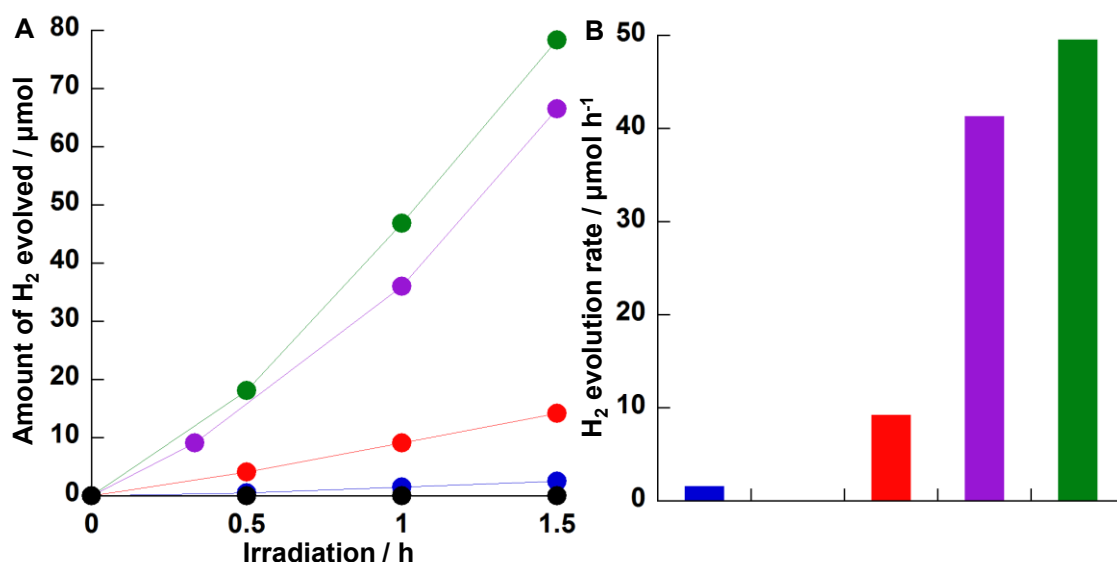

Figure 3-18. (A) The time courses of H_2 evolution from an aqueous methanol solution (5 mL, 1/1 in V/V) and (B) H_2 evolution rate of HTO (blue), P25 (black), HTO/P25 mixture (13 mg/2 mg) (red), Pt@P25 (purple) and HTO/Pt@P25 mixture (13 mg/2 mg) (green) under simulated solar light (>300 nm).
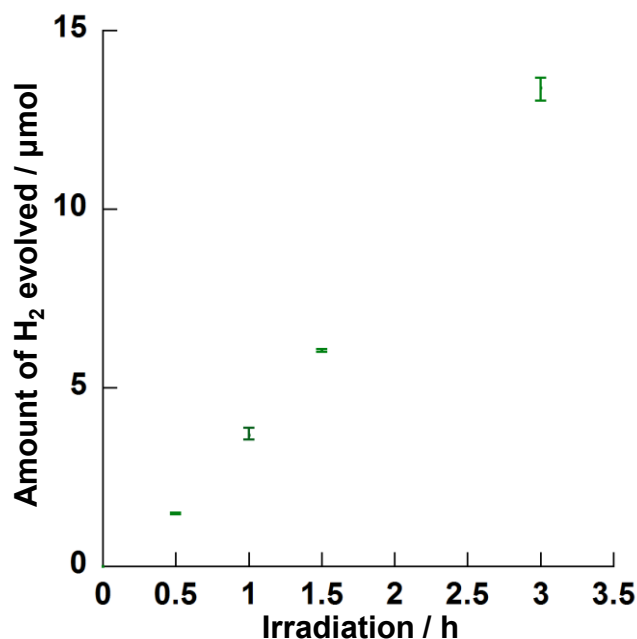
Figure 3-19. The time course of H$_2$ evolution from an aqueous methanol solution (5 mL, 1/1 in V/V) of HTO/Pt@P25 composite (13 mg/2 mg) under monochromated light irradiation (320 nm).

3-4. Conclusions

The remarkably enhanced photocatalytic activity of a composite of lepidocrocite-type layered titanate particles and a much smaller amount of P25 TiO$_2$ particles, prepared by simple mixing of these particle in reaction media, enhanced photocatalytic reactions such as oxidative decomposition of formic acid in water and H$_2$ evolution from an aqueous methanol solution. The enhancement was ascribable to heterojunction creation for efficient charge separation *via* transfer of photogenerated electrons from the titanate to P25. The AQY at 320 nm was up to 73 % when an unusually small amount of the Pt co-catalyst was used. This simple, low-cost and efficient methodology can be applied to other layered inorganic semiconductors and their intercalation compounds, making their applications in photocatalysis more effective and realistic.

3-5. References

[1]   Fujishima, A.; Zhang, X.; Tryk, D. A. TiO$_2$ Photocatalysis and Related Surface Phenomena. *Surf. Sci. Rep.* **2008**, *63*, 515–582.

[2]   Kudo, A.; Miseki, Y. Heterogeneous Photocatalyst Materials for Water Splitting. *Chem. Soc. Rev.* **2009**, *38*, 253–278.

[3]   Shiraishi, Y.; Hirai, T. Selective Organic Transformations on Titanium Oxide-Based Photocatalysts. *Photochem. Photobiol.* **2008**, *9*, 157–170.

[4]   Vivero-Escoto, J. L.; Chiang, Y.-D.; Wu, K. C.-W.; Yamauchi, Y. Recent Progress in Mesoporous Titania Materials: Adjusting Morphology for Innovative Applications. *Sci. Technol. Adv. Mater.* **2012**, *1*, 13003.

[5]   Liao, Y.-T.; Huang, C.-W.; Liao, C.-H.; Wu, J. C.-S.; Wu, K. C.-W. Synthesis of Mesoporous Titania Thin Films (MTTFs) with Two Different Structures as Photocatalysts for Generating Hydrogen from Water Splitting. *Appl. Energy* **2012**, *100*, 75–80.

[6]   Youngblood, W. J.; Lee, S.-H. A.; Maeda, K.; Mallouk, T. E. Visible Light Water Splitting Using Dye-Sensitized Oxide Semiconductors. *Acc. Chem. Res.* **2009**, *42*, 1966–1973.

[7]   Gunjakar, J. L.; Kim, I. Y.; Lee, J. M.; Jo, Y. K.; Hwang, S.-J. Exploration of Nanostructured Functional Materials Based on Hybridization of Inorganic 2D Nanosheets. *J. Phys. Chem. C* **2014**, *118*, 3847–3863.

[8]   Okada, T.; Ide, Y.; Ogawa, M. Organic-Inorganic Hybrids Based on Ultrathin Oxide Layers: Designed Nanostructures for Molecular Recognition. *Chem. - Asian J.* **2012**, *7*, 1980–1992.

[9]   Ida, S.; Takashiba, A.; Koga, S.; Hagiwara, H.; Ishihara, T. Potential Gradient and Photocatalytic Activity of Ultrathin p-n Junction Surface Prepared with Two-Dimensional Semiconducting Nanocrystals. *J. Am. Chem. Soc.* **2014**, *136*, 1872-1878.

[10]   Mochizuki, D.; Kumagai, K.; Maitani, M. M.; Wada, Y. Alternate Layered Nanostructures of Metal Oxides by a Click Reaction. *Angew. Chem., Int. Ed.* **2012**, *51*, 5452–5455.

[11]   Ide, Y.; Nakasato, Y.; Ogawa, M. Molecular Recognitive Photocatalysis Driven by the Selective Adsorption on Layered Titanates. *J. Am. Chem. Soc.* **2010**, *132*,

3601–3604.

[12] Ide, Y.; Matsuoka, M.; Ogawa, M. Efficient Visible-Light-Induced Photocatalytic Activity on Gold-Nanoparticle-Supported Layered Titanate. *J. Am. Chem. Soc.* **2010**, *132*, 16762–16764.

[13] Ohtani, B.; Ikeda, S.; Nakayama, H.; Nishimoto, S. Shape- and Size-Selective Photocatalytic Reactions by Layered Titanic Acid Powder Suspended in Deaerated Aqueous Alcohol Solutions. *Phys. Chem. Chem. Phys.* **2000**, *2*, 5308–5313.

[14] Abe, R.; Shinmei, K.; Koumura, N.; Hara, K.; Ohtani, B. Visible-Light-Induced Water Splitting Based on Two-Step Photoexcitation between Dye-Sensitized Layered Niobate and Tungsten Oxide Photocatalysts in the Presence of a Triiodide/iodide Shuttle Redox Mediator. *J. Am. Chem. Soc.* **2013**, *135*, 16872–16884.

[15] Salim, S.; Huq, M.; Mallouk, T. E. Visible Light Photolysis of Hydrogen Iodide Using Sensitized Layered Semiconductor Particles. *J. Am. Chem. Soc.* **1991**, *113*, 9561–9563.

[16] Ide, Y.; Komaguchi, K. A Photocatalytically Inactive Microporous Titanate Nanofiber as an Excellent and Versatile Additive to Enhance the TiO_2 Photocatalytic Activity. *J. Mater. Chem. A* **2015**, *3*, 2541–2546.

[17] Ide, Y.; Sadakane, M.; Sano, T.; Ogawa, M. Functionalization of Layered Titanates. *J. Nanosci. Nanotechnol.* **2014**, *14*, 2135–2147.

[18] Xiang, Q.; Yu, J.; Jaroniec, M. Graphene-Based Semiconductor Photocatalysts. *Chem. Soc. Rev.* **2012**, *41*, 782–796.

[19] Tada, H.; Kiyonaga, T.; Naya, S. Rational Design and Applications of Highly Efficient Reaction Systems Photocatalyzed by Noble Metal Nanoparticle-Loaded Titanium(iv) Dioxide. *Chem. Soc. Rev.* **2009**, *38*, 1849-1858.

[20] Ogawa, M.; Morita, M.; Igarashi, S.; Sato, S. A Green Synthesis of a Layered Titanate, Potassium Lithium Titanate; Lower Temperature Solid-State Reaction and Improved Materials Performance. *J. Solid State Chem.* **2013**, *206*, 9–13.

[21] Kominami, H.; Tanaka, A.; Hashimoto, K. Mineralization of Organic Acids in Aqueous Suspensions of Gold Nanoparticles Supported on cerium(IV) Oxide Powder under Visible Light Irradiation. *Chem. Commun.* **2010**, *46*, 1287–1289.

[22] Prieto-Mahaney, O.-O.; Murakami, N.; Abe, R.; Ohtani, B. Correlation between Photocatalytic Activities and Structural and Physical Properties of Titanium(IV)

Oxide Powders. *Chem. Lett.* **2009**, *38*, 238–239.

[23] Goto, H.; Hanada, Y.; Ohno, T.; Matsumura, M. Quantitative Analysis of Superoxide Ion and Hydrogen Peroxide Produced from Molecular Oxygen on Photoirradiated TiO_2 Particles. *J. Catal.* **2004**, *225*, 223–229.

[24] Ohno, T.; Sarukawa, K.; Matsumura, M. Crystal Faces of Rutile and Anatase TiO_2 particles and Their Roles in Photocatalytic Reactions. *New. J. Chem.* **2002**, *26*, 1167–1170.

[25] Amano, F.; Prieto-Mahaney, O. O.; Terada, Y.; Yasumoto, T.; Shibayama, T.; Ohtani, B. Decahedral Single-Crystalline Particles of Anatase titanium(IV) Oxide with High Photocatalytic Activity. *Chem. Mater.* **2009**, *21*, 2601–2603.

[26] Sasaki, T.; Kooli, F.; Iida, M.; Michiue, Y.; Takenouchi, S.; Yajima, Y.; Izumi, F.; Chakoumakos, B. C.; Watanabe, M. A Mixed Alkali Metal Titanate with the Lepidocrocite-like Layered Structure. Preparation, Crystal Structure, Protonic Form, and Acid−Base Intercalation Properties. *Chem. Mater.* **1998**, *10*, 4123–4128.

[27] Kominami, H.; Kato, J.; Takada, Y.; Doushi, Y.; Ohtani, B.; Nishimoto, S.; Inoue, M.; Inui, T.; Kera, Y. Novel Synthesis of Microcrystalline Titanium (IV) Oxide Having High Thermal Stability and Ultra-High Photocatalytic Activity: Thermal Decomposition of Titanium (IV) Alkoxide in Organic Solvents. *Catal. Letters* **1997**, *46*, 235–240.

[28] Ito, S.; Inoue, S.; Kawada, H.; Hara, M.; Iwasaki, M.; Tada, H. Low-Temperature Synthesis of Nanometer-Sized Crystalline TiO_2 Particles and Their Photoinduced Decomposition of Formic Acid. *J. Colloid Interface Sci.* **1999**, *216* , 59–64.

[29] Bian, Z.; Tachikawa, T.; Majima, T. Superstructure of TiO_2 Crystalline Nanoparticles Yields Effective Conduction Pathways for Photogenerated Charges. *J. Phys. Chem. Lett.* **2012**, *3*, 1422–1427.

[30] Ide, Y.; Inami, N.; Hattori, H.; Saito, K.; Sohmiya, M.; Tsunoji, N.; Komaguchi, K.; Sano, T.; Bando, Y.; Golberg, D.; Sugahara, Y. Remarkable Charge Separation and Photocatalytic Efficiency Enhancement through Interconnection of TiO_2 Nanoparticles by Hydrothermal Treatment. *Angew. Chem., Int. Ed.* **2016**, *55*, 3600-3605.

[31] Akatsuka, K.; Takanashi, G.; Ebina, Y.; Haga, M.; Sasaki, T. Electronic Band Structure of Exfoliated Titanium- and/or Niobium-Based Oxide Nanosheets

Probed by Electrochemical and Photoelectrochemical Measurements. *J. Phys. Chem. C* **2012**, *116*, 12426–12433.

[32]   Ohtani, B.; Nohara, Y.; Abe, R. Role of Molecular Oxygen in Photocatalytic Oxidative Decomposition of Acetic Acid by Metal Oxide Particulate Suspensions and Thin Film Electrodes. *Electrochemistry* **2008**, *76*, 147-149.

[33]   Sakai, N.; Ebina, Y.; Takada, K.; Sasaki, T. Electronic Band Structure of Titania Semiconductor Nanosheets Revealed by Electrochemical and Photoelectrochemical Studies. *J. Am. Chem. Soc.* **2004**, *126*, 5851–5858.

[34]   Scaife, D. E. Oxide Semiconductors in Photoelectrochemical Conversion of Solar Energy. *Solar Energy* **1980**, *25*, 41-54.

[35]   Kawahara, T.; Konishi, Y.; Tada, H.; Tohge, N.; Nishii, J.; Ito, S. A Patterned TiO_2 (Anatase)/TiO_2 (Rutile) Bilayer-Type Photocatalyst: Effect of the Anatase/Rutile Junction on the Photocatalytic Activity. *Angew. Chem., Int. Ed.* **2002**, *41*, 2811–2813.

[36]   Abe, R.; Takami, H.; Murakami, N.; Ohtani, B. Pristine Simple Oxides as Visible Light Driven Photocatalysts: Highly Efficient Decomposition of Organic Compounds over Platinum-Loaded Tungsten Oxide Photocatalysts under Visible Light Irradiation. *J. Am. Chem. Soc.* **2008**, *130*, 7780-7781.

CHAPTER 4

Room-temperature Rutile TiO$_2$ Nanoparticle

Formation on Protonated Layered Titanate for

High-performance Heterojunction Creation

4. Room-temperature Rutile TiO$_2$ Nanoparticle Formation on Protonated Layered Titanate for High-performance Heterojunction Creation

4-1. Introduction

Development of TiO$_2$ and TiO$_2$-based materials with better properties and performance is a crucial and as-yet challenging issue for various important applications, including dye-sensitized solar cells and photocatalysts.[1-5] Heterojunctions between different TiO$_2$ phases (*e.g.* anatase and rutile, the main polymorphs of TiO$_2$), including heterostructures of different TiO$_2$-based nanostructures, can create synergy effects, such as enhanced electron mobility[6-11] and charge separation efficiency[12-15] *via* intra-particle charge transfer, which are beneficial for the above-mentioned applications. Especially in the field of photocatalysts, state-of-the-art or benchmark TiO$_2$ heterojunctions were formed under rather strict conditions, such as calcination at high temperatures or hydrothermal reactions of TiO$_2$.[13-16] In contrast, layered titanate-based heterojunctions were formed *via* soft chemical routes, including exfoliation and restacking that enable intercalation of a variety of functional units, and have thus attracted increased attention.[17-20] Upon intercalation of different TiO$_2$ nanostructures,[21-25] for instance, layered titanate materials have shown remarkably enhanced photocatalytic performances, possibly because of a prompt charge transfer to the surface resulting from the extreme thinness of the nanosheets.[26-30] However, the photocatalytic activity of these layered titanate-based heterojunctions is often lower than that of conventional TiO$_2$ heterojunctions.

Layered potassium titanate with a lepidocrocite structure (*e.g.* K$_{0.8}$Ti$_{1.73}$Li$_{0.27}$O$_4$, referred to as "KTLO" hereafter) has been investigated for designing heterojunction photocatalysts. The interlayer potassium cations can be exchanged with protons by treatment with diluted HCl and the protonated forms (*e.g.* H$_{1.07}$Ti$_{1.73}$□$_{0.27}$O$_4$, referred to as "HTO", equivalent to H$_{1.07}$Ti$_{1.73}$O$_4$; □ denotes a defect)[31,32] are often used for further intercalation reactions.[18]

Here, a methodology for creating protonated layered titanate (HTO)-rutile heterojunctions with no intercalation reactions is reported. Rutile was formed from HTO on the outer particle surface of HTO to create heterojunctions *via* dilute HCl treatment and subsequent drying at room temperature under reduced pressure. Although room-temperature formation of rutile nanoparticles through a sol-gel reaction has

already been reported,[33-36] this is the first report on room-temperature rutile formation using layered potassium titanate as a starting material. After Pt-loading, the resulting protonated layered titanate/rutile composite with heterojunctions exhibited higher photocatalytic performance for H_2 evolution from water containing methanol as a sacrifice agent under simulated solar light compared to that of Pt-loaded P25, the standard photocatalyst for this reaction.

4-2. Experimental

Reagents and materials

K_2CO_3 (>99.95 %), Li_2CO_3 (>99.95 %), Na_2CO_3 (>99.5 %), α-Al_2O_3 (>99.0 %), HCl (35.0-37.0 %) and methanol (>99.5 %) were purchased from Kanto Chemical Co., Inc. $H_2PtCl_6 \cdot 6H_2O$ (99.9 %) was purchased from Wako Pure Chemical Industry, Ltd. P25 (>95.0 %) was supplied by Nippon Aerosil Co., Ltd. Anatase (JRC-TIO-1) and rutile (JRC-TIO-6) were supplied by the Catalysis Society of Japan. All reagents and materials were used as received.

Characterizations

X-ray diffraction (XRD) patterns of the solid products were collected using a powder X-ray diffractometer (Smart Lab, RIGAKU) with Cu Kα radiation at 40 kV and 30 mA. Raman spectra were obtained with a Renishaw in Via reflex spectrometer using a 532-nm laser. The morphology was observed with a field emission scanning electron microscope (FE-SEM) (JEOL JEM-6500F). High-resolution transmission electron microscopic (HRTEM) images were obtained with a JEOL JEM-6500F microscope. Inductivity coupled plasma atomic emission spectroscopy (ICP-AES) was performed on an Agilent 710-ES spectrometer. UV-vis spectra were obtained with a JASCO V-750 spectrophotometer equipped with an integrating sphere (ISV-722 attachment). The nitrogen adsorption/desorption isotherms were measured at 77 K with a BELSORP 28 instrument (BEL Japan, Inc) to determine the specific surface areas by the Brunauer-Emmett-Teller (BET) method.

Crystal structure analysis

Crystal structure analysis was revisited using X-ray pair distribution functions (PDFs).[37] The X-ray total scattering data were collected at the BL10XU beamline at SPring-8 (λ = 0.20133 Å) on a FPD detector (Perkin Elmer, XRD0822). The samples were sealed in 1 mmφ Lindemann glass capillaries. The raw data were converted to PDF format after data correction (background subtraction, etc.) and normalization with form factors as reported previously.[38] The PDFs were analyzed using the PDFgui program.[39]

Preparation of layered titanates

KTLO was prepared according to the method used in the previous report.[40] K_2CO_3, Li_2CO_3 and TiO_2 (at a molar ratio of 2.4:0.8:10.4) were mixed using a planetary ball mill (Planet M2-3, Gokin Planetaring), and the mixture was calcined in air at 600 °C for 30 min, and then was calcined for another 20 h after grinding. $Na_2Ti_3O_7$ and $K_2Ti_4O_9$ were prepared according to the method used in the previous report.[41] K_2CO_3 and TiO_2 (at molar ratios of 1:3) or Na_2CO_3 and TiO_2 (at molar ratios of 1:3.5) were mixed, and the mixture was heated in air at 800 °C for 20 h, and then was calcined for another 20 h after mixing.

Synthesis of R/HTO

KTLO was dispersed in dilute HCl (30 mL, 0.5 M) by ultrasonication, and the dispersion was stirred with a magnetic stirrer at room temperature under ambient pressure for 3 days. The cake was separated from the dispersion by centrifugation (3500 rpm, 20 min) and dried under reduced pressure at room temperature for 10 days, while the cake was washed repeatedly with water before drying to prepare protonated layered titanate (HTO).[42]

Preparation of Pt-loaded photocatalysts

Pt-loaded photocatalysts were prepared according to the method used in the previous report.[43] The sample was suspended in aqueous methanol solution (5 mL, 1/1 in V/V) in a Pyrex glass tube (34 mL), and $H_2PtCl_6 \cdot 6H_2O$ (Pt/sample = 0.5 wt%) was

added to the suspension. The resulting suspension was ultrasonicated for 1 min and then deaerated by argon bubbling. The glass tube was sealed with a rubber septum and irradiated with an ultra-high-pressure mercury lamp (350 W, Ushio Inc.) under stirring for 10 min. The solid was separated by centrifugation (3500 rpm, 20 min), washed with water, and dried under reduced pressure at room temperature.

Quantitative analysis of rutile in R/HTO

The amount of immobilized rutile in R/HTO was calculated using a calibration curve, which showed rutile/α-Al$_2$O$_3$ intensity ratios as a function of the rutile content in HTO/rutile binary mixtures prepared according to the method reported previously.[44] HTO and rutile with a particle size similar to that of rutile in R/HTO (JRC-TIO-6 supplied by the Catalysis Society of Japan) were mixed at different ratios by an agate mortar, and α-Al$_2$O$_3$ (20 wt%) was added to the mixture as an internal standard. The obtained mixtures with α-Al$_2$O$_3$ were analyzed by XRD, and the (111) plane of rutile/the (104) plane of α-Al$_2$O$_3$ intensity ratios were plotted against the rutile wt% in the mixtures to prepare the calibration curve.

Photocatalytic H$_2$ evolution

The sample (15 mg) was suspended in an aqueous methanol solution (5 mL, 1/1 in V/V) in a Pyrex glass tube (34 mL), ultrasonicated for 1 min and then deaerated by argon bubbling.[43] The glass tube was sealed with a rubber septum and irradiated with a solar simulator (San-Ei Electric, λ >300 nm, 1000 Wm^{-2}) under stirring. The gas in the glass tube was collected with a gas-tight syringe and quantified using a TCD gas chromatograph (Shimadzu GC-8A) equipped with a SHINCARBON-ST 50-80 column. For the apparent quantum yield (AQY) calculation, the glass tube was irradiated with a monochromated light for 3 h using a 500 W Xe lamp (Ushio) and SM-25 monochromator (Bunkoukeiki). The number of incident photons was determined using an S1337-1010BQ silicon photodiode (Bunkoukeiki). AQY was defined by the following equation according to the previous report[45]:

$$\text{AQY (\%)} = \frac{\text{Number of reacted electrons}}{\text{Number of incident photons}} \times 100$$

$$= \frac{\text{Number of evolved } H_2 \text{ molecules} \times 2}{\text{Number of incident photons}} \times 100$$

4-3. Results and Discussion

Formation of KTLO was confirmed by XRD (Figure 4-1). KTLO was reported to have an orthorhombic structure (*CmCm* space group)[42] as determined by XRD. The local structure determined by PDF analysis taking the K-sites disorders into consideration was $a = 3.816(12)$, $b = 15.60(7)$, $c = 8.90(3)$ Å in an orthorhombic structure, but its space group was found to be *Cm*11 (suggesting a monoclinic cell structure). For the room-temperature formation of rutile, KTLO was treated with dilute HCl (0.5 M) under ambient conditions as in other studies.[32,42] After centrifugation, a cake separated from the dispersion was dried at room temperature under reduced pressure for 10 days. Although no thermal treatment was conducted, this product (referred to as "R/HTO") contained rutile, as revealed by XRD (Figure 4-1) and Raman spectroscopy (Figure 4-2).[46,47] For comparison, the cake was washed repeatedly with water and then dried at room temperature under reduced pressure as in other studies, and then the protonated product, HTO was recovered.[42] The HTO structure was determined by PDF refinement to be in a monoclinic system of the *Pm* space group ($a = 18.40(7)$, $b = 3.776(9)$, $c = 2.990(9)$ Å, $\beta = 89.3(4)°$). HTO and KTLO did not contain rutile, as confirmed by XRD (Figure 4-1) and Raman spectroscopy (Figure 4-2).[46,47]
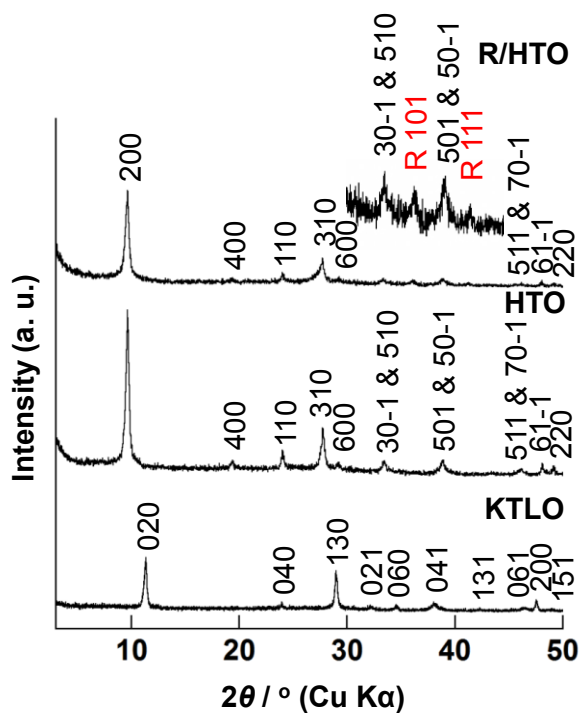
Figure 4-1. XRD patterns of KTLO, HTO and R/HTO.
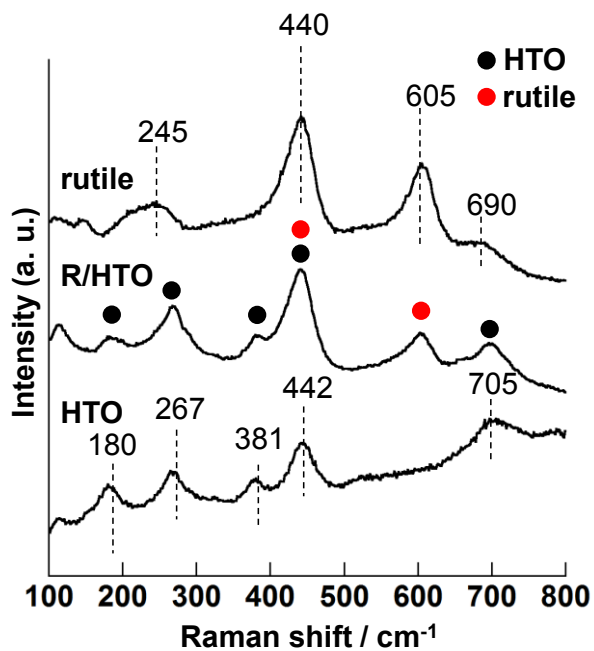
Figure 4-2. Raman spectra of KTLO, HTO and R/HTO.

The basal spacing of the HTO phase in R/HTO was almost identical to that of HTO (0.92 nm), suggesting that rutile was not intercalated into the HTO phase. The distribution of the rutile phase was analyzed by SEM and HRTEM as follows. Figure 4-3 shows SEM images of KTLO, HTO and R/HTO. KTLO consisted of rounded rectangular particles (70–100 nm) with smooth surfaces. The HTO appeared similar to KTLO, with some particle fragments on the edges of the particles. In contrast, the R/HTO surfaces were covered with large numbers of nanoparticles (10-20 nm), and the morphology of the HTO particles in R/HTO appeared similar to that of HTO.
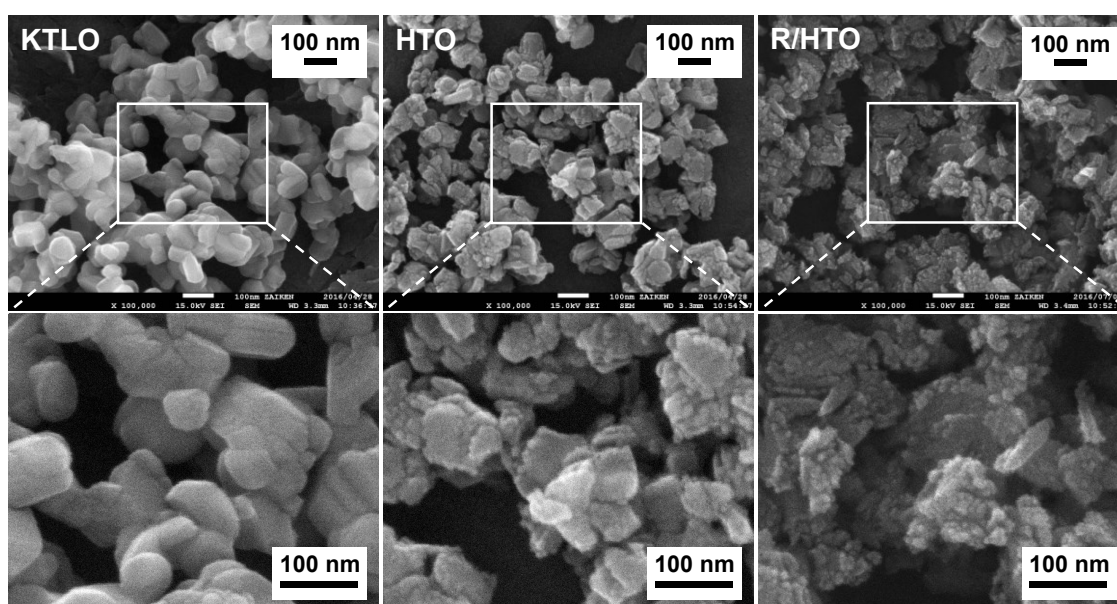
Figure 4-3. SEM images of KTLO, HTO and R/HTO.

The smaller particles were ascertained to be rutile by HRTEM observation (Figure 4-4), which further revealed that the rutile particles were not simply formed as isolated particles but were attached to HTO particles (Figure 4-4). The presence of a large interface strongly suggests that efficient charge transfer between HTO particles and rutile *via* the heterojunction is possible. The amount of the rutile in R/HTO was calculated to be 21 wt% by a reported method (Figure 4-5).[44] It should be noted that KTLO was completely transformed to rutile when treated with 1 M HCl at 60 °C (Figure 4-6) without subsequent drying.
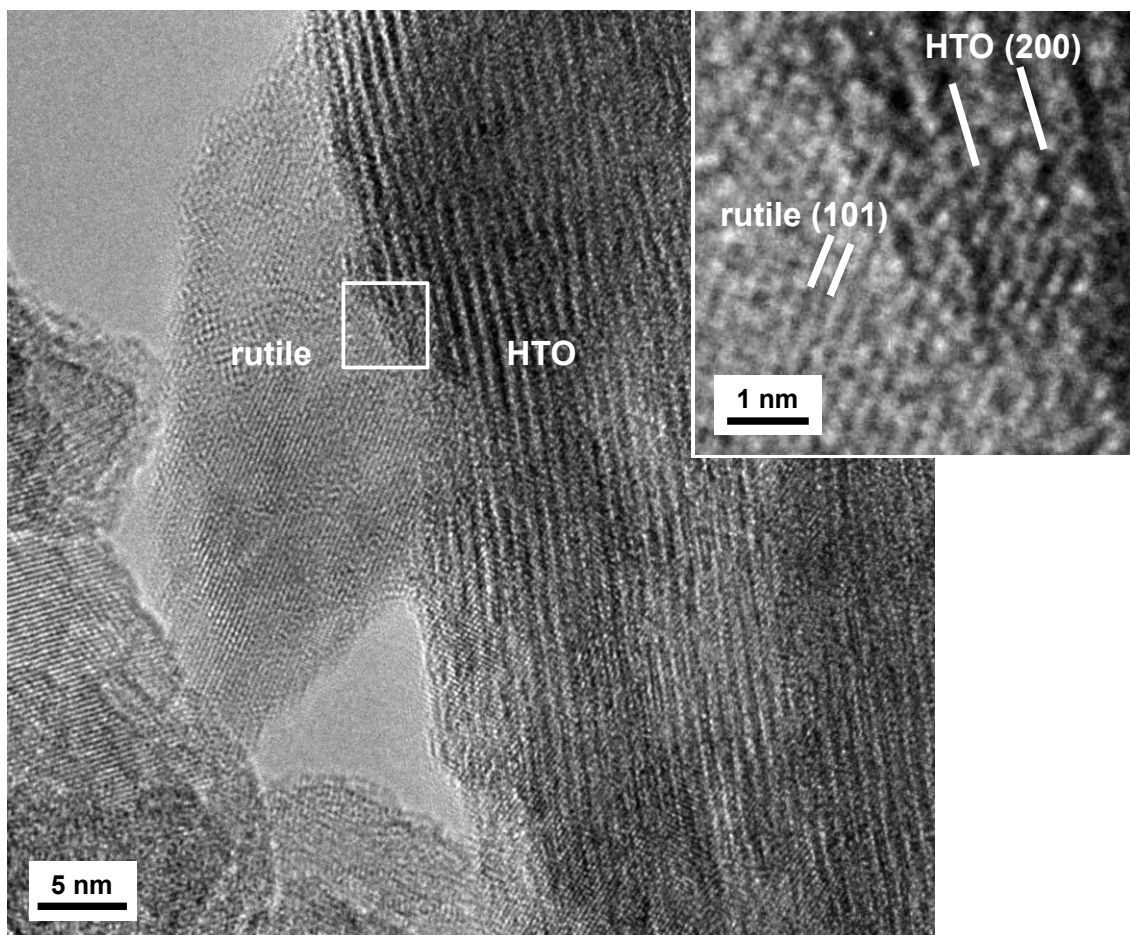
Figure 4-4. HRTEM image of R/HTO. Inset shows an expanded image of the area indicated by a white square.
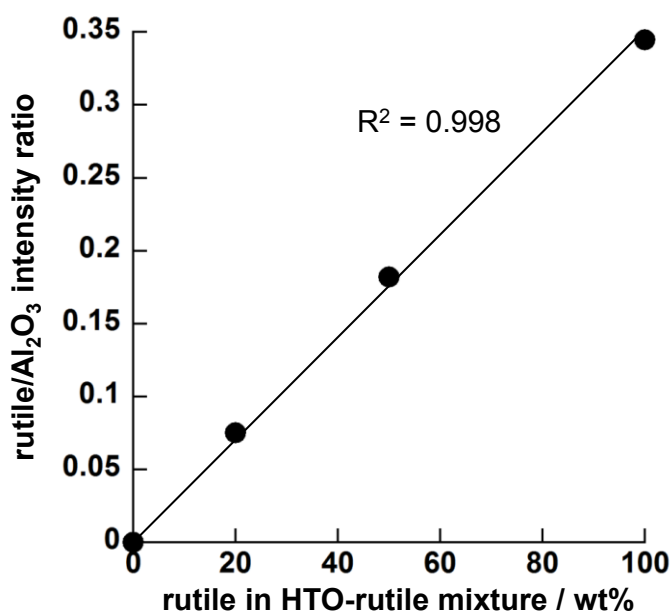
Figure 4-5. Calibration curve of rutile obtained using a mixture of HTO and rutile TiO_2 (JRC-TIO-6) with α-Al_2O_3 as an internal standard.
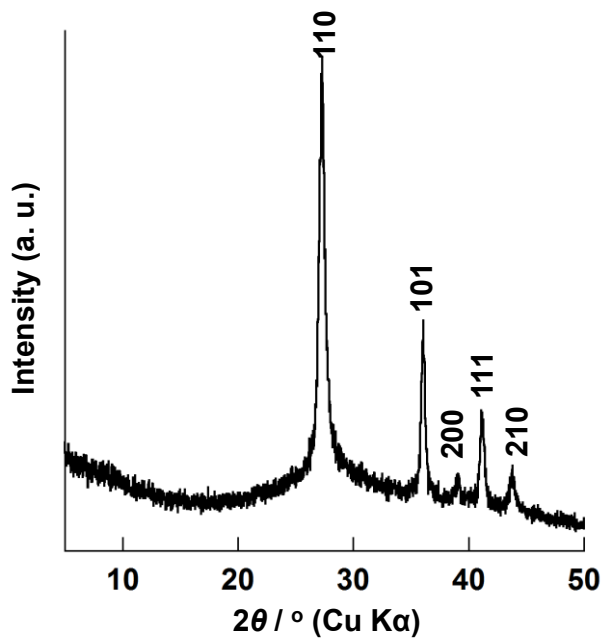
Figure 4-6. XRD pattern of rutile prepared from KTLO by treatment with 1 M HCl at 60 °C for one day.

As shown in synchrotron in-situ X-ray total scattering patterns of the cake (HCl-treated KTLO) at room temperature (Figure 4-7), three diffraction peaks at 2θ (CuKα) =36.1°, 41.2° and 69.0°, which are indexed to (101), (111) and (301) plane of rutile, respectively, appeared just after the start of the drying. Figure 4-8 A shows the result of PDF analysis of HTO, in which the experimental data (blue curve) was successfully fitted with the simulated data (red curve), further confirming the fact that rutile was not contained in HTO. On the other hand, as shown in Figure 4-8 B, the experimental data of the cake after 195 min from the start of the drying (blue curve) can be fitted with two phases of HTO and rutile (red curve), confirming the fact that rutile was formed during the drying process. As shown in Figure 4-9, phase fraction of rutile (wt%) increased slightly with time (e.g., 12.4 % at 35 min to 13.3 % at 195 min). It can be assumed that the phase fraction of rutile increases by up to *ca.* 20 % upon longer drying.

In order to acquire even clearer understanding of the mechanism, the compositions of a separated supernatant were studied. Upon acid treatment of KTLO, a large portion of the interlayer K ions and almost all the framework Li ions were extracted (Table 4-1). Such efficient Li extraction from the framework is ascribable to weakness of the solids.[48-50]

Table 4-1. Extraction of K, Li and Ti from different layered titanates and TiO_2. The amounts (wt%) of the extracted elements are based on the starting KTLO.

Samples	Amount extracted (wt%)		
	K	Li	Ti
KTLO	84.9	93.8	21.6
$K_2Ti_4O_9$	97.6	N. D.	3.5
$Na_2Ti_3O_7$	N. D.	N. D.	1.2
anatase (JRC-TIO-1)	N. D.	N. D.	0.1
P25	N. D.	N. D.	N. D.
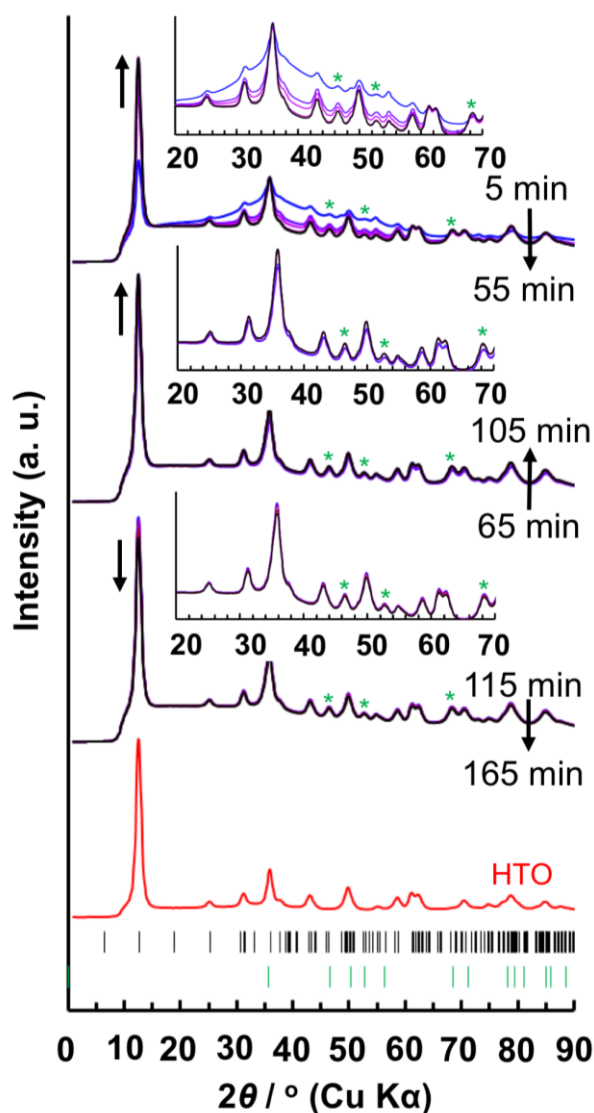
Figure 4-7. Change in synchrotron X-ray total scattering patterns of the cake coating a glass capillary. The data were collected every 5 min (5-min averaged data): top, start time of 5-55 min (from blue to black); 2nd, 65-105 min; 3rd, 115-165 min; and bottom, HTO sample packed in a glass capillary. Asterisks (*) mark in the patterns show the peaks assignable to the rutile structure. The black lines below show the Bragg peak positions of HTO, and the green lines show those of rutile. The arrows indicate the direction of peak growth.
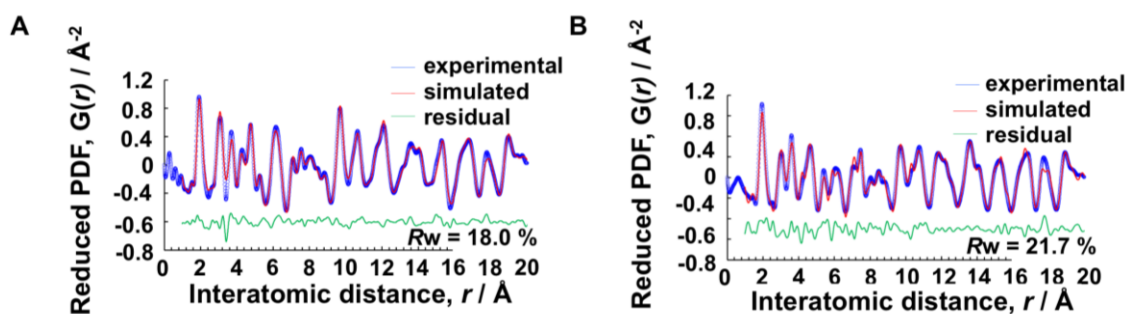
Figure 4-8. (A) PDF analysis of the HTO data. The $G(r)$ data were obtained for the structure function of Q_{max} = 20.3 Å^{-1}. The fitting range was 1-35 Å. (B) PDF analysis of the cake sample (start time 195 min). The $G(r)$ data were obtained for the structure function of Q_{max} = 21.0 Å^{-1}. The fitting range was carried out using two phases of HTO and rutile in the range of 1-20 Å.
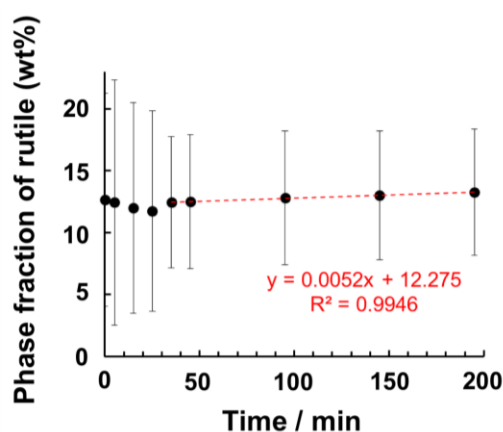
Figure 4-9. Phase fraction of rutile (wt%) obtained by PDF analysis.

In addition, a considerably larger number of Ti ions was extracted compared to other types of layered titanates such as $K_2Ti_4O_9$ and $Na_2Ti_3O_7$ (Figure 4-10), and titanias such as anatase TiO_2 (JRC-TIO-1) and mixed-phase TiO_2 (anatase and rutile, P25). This efficient Ti extraction from KTLO is ascribable to defects formed by Li extraction. Moreover, rutile was not formed from other types of layered tiatanates or titanias when

treated in the same manner as KTLO, which was revealed by Raman spectroscopy except for P25 (Figure 4-11). P25 contains rutile originally, thus the (101) plane of anatase/the (110) plane of rutile intensity ratio after the acid treatment was compared with that of before the acid treatment (Figure 4-12). The intensity ratio was constant, indicating the fact that rutile was not formed from anatase in P25 *via* the acid treatment. It should be noted that rutile was not formed when the supernatant, which contained dissolved Ti from KTLO, was dried up at room temperature for 10 days (mainly KCl was formed) as shown in Figure 4-13, suggesting that rutile was not formed *via* dissolution and precipitation process of KTLO cake during drying process.
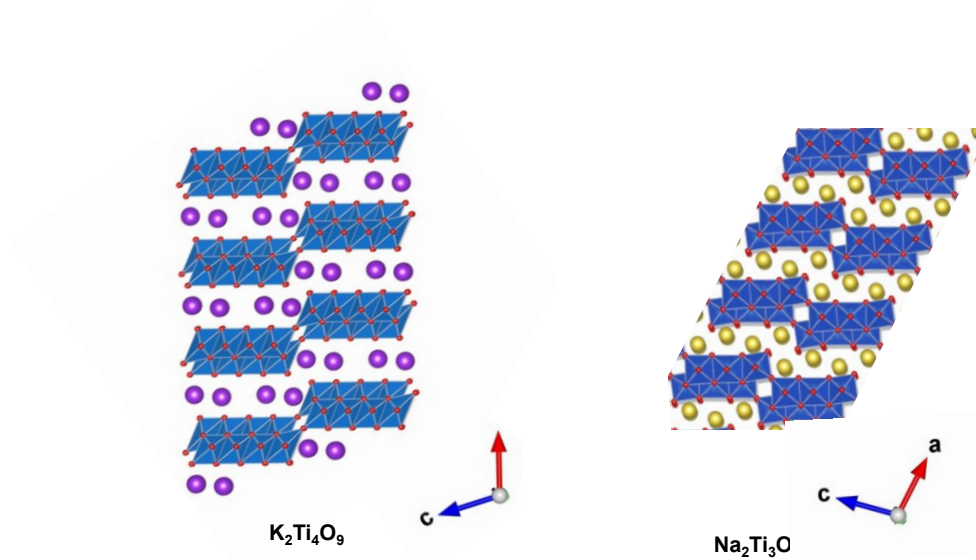
Figure 4-10. Crystal structures of $K_2Ti_4O_9$ and $Na_2Ti_3O_7$.
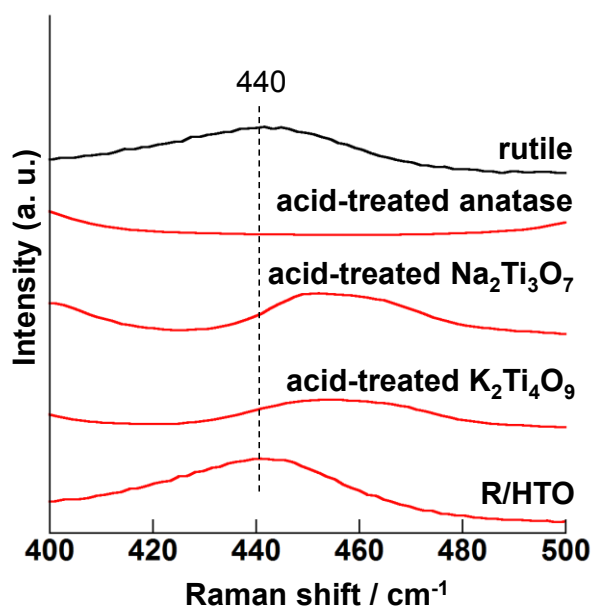
Figure 4-11. Raman spectra of different samples after dilute HCl treatment.
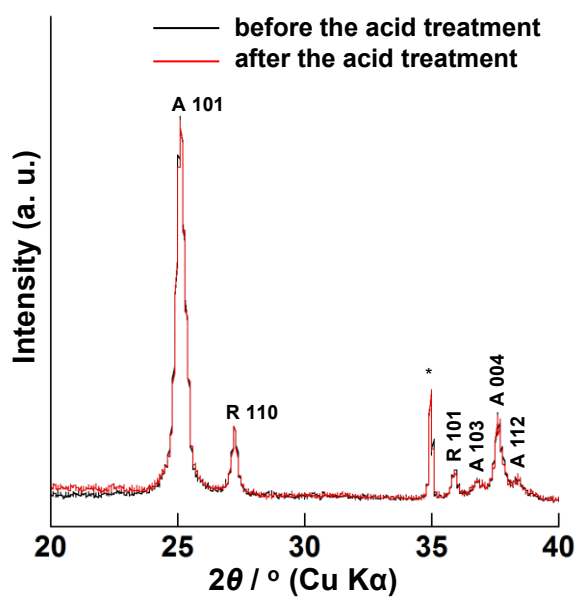
Figure 4-12. XRD patterns of P25 before and after acid treatment. The asterisk indicates a diffraction peak from Al_2O_3 used as a standard for normalizing the XRD pattern.
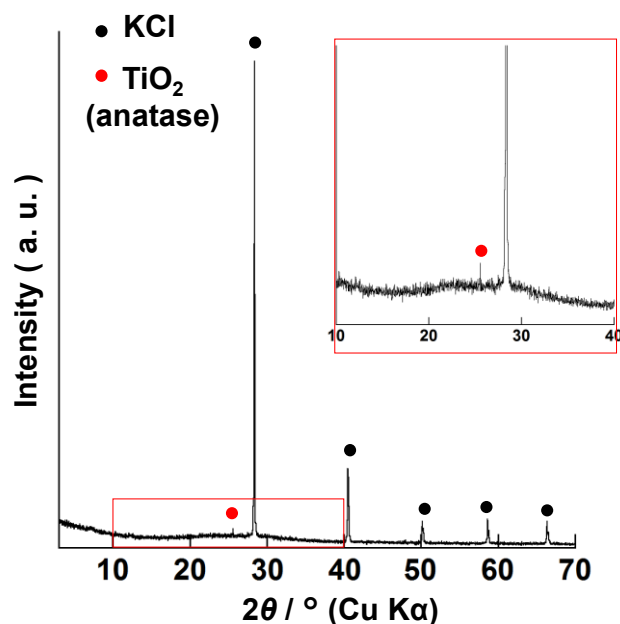
Figure 4-13. XRD pattern of powder obtained by drying supernatant at room temperature under reduced pressure after dilute HCl treatment of KTLO. The inset shows an expanded XRD pattern of the area indicated by a red square.

In light of the above facts, two possible mechanisms could be proposed for the room-temperature rutile formation from HTO. One is that the crystal structure of HTO was locally disordered as a result of considerable extraction of Li and Ti ions from the framework during dilute HCl treatment and then reconstructed into rutile during the drying process. According to the previous reports,[34,35] amorphous titania crystallized into rutile even with aging at room temperature. Considering the fact that Li and Ti ions were efficiently extracted from the framework, the surface structure of HCl-treated KTLO is likely to be amorphous, making this scenario possible. The fact that rutile was not formed from other types of layered titanates and titanias from which metal ions were not extracted is in good agreement with this scenario. Based on the fact that rutile formation was not observed when the cake was washed with water after the acid treatment, chloride ions, which catalyze crystallization of rutile in the sol-gel process at room temperature,[33] are likely to play an important role.

On the other hand, in the zeolite conversion process, one zeolite decomposed into locally ordered aluminosilicate species (referred to as "nanoparts"), whose structure was similar to the local structure of the original zeolite, and the nanoparts assembled into another zeolite.[51-53] As shown in Figure 4-14 A, HTO has 1D chains of edge-shared TiO_6 octahedra formed along the *c* axis (Ti-Ti distance 2.990 Å, determined by PDF analysis), which in turn forms a 2D structure through edge-sharing along the *b* axis (Ti-Ti distance 3.057 and 3.125 Å). Rutile also has such 1D chains along the *c* axis (Ti-Ti distance of 2.941 Å, rutile phase in Figure 4-8 B), which are similar to the 1D chains in HTO, though they form 3D structures through corner-sharing along the *a* axis as well as the *b* axis (Ti-Ti distance 3.578 Å) (Figure 4-14 B). Based on the experimental findings, another possible mechanism for the room-temperature rutile formation is that the HTO segments or "titania nanoparts," were formed during dilute HCl treatment, and those segments were adsorbed on to the outer particle surface of HTO particles and crystallized into rutile during the dying process. In this case, the fact that rutile was not formed when the cake was washed with water after acid treatment is assumed to be ascribable to removal of the nanoparts from the HTO surface during washing. There are two possible reasons for the absence of signals assignable to such Ti segments in the PDF spectra. One is that the dissolved Ti segments from HTO were larger than 20 Å, as the PDF for data within this range can be regarded as HTO and rutile. The other is that the amount of the Ti segments was below the detection limit judging from the fact that the amount of rutile formed remained almost constant during measurement.
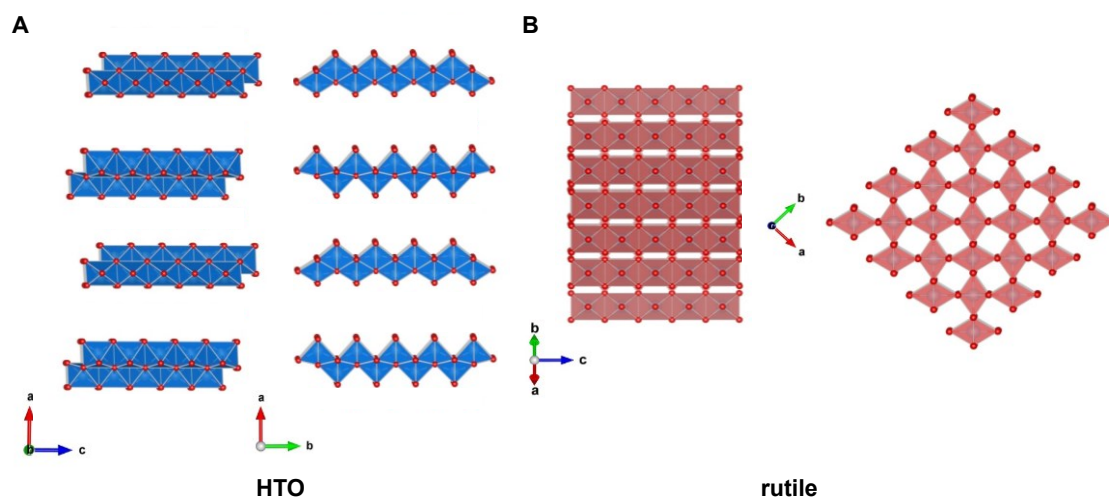
Figure 4-14. Crystal structures of (A) HTO and (B) rutile.

Figure 4-15 A shows the diffuse reflectance UV-Vis spectra of HTO, rutile and R/HTO. HTO absorbed only UV light with a wavelength shorter than 370 nm, while R/HTO absorbed light with a wavelength longer than 370 nm like sole rutile. The precise point of absorption onset was determined to be 408 nm (equivalent to a bandgap energy of 3.0 eV) by a Tauc plot[54] prepared from the diffuse reflectance UV-vis spectrum (Figure 4-15 B). The successful extension of light absorption of HTO to the longer wavelength region can be explained by the presence of attached rutile nanoparticles (20 wt%).
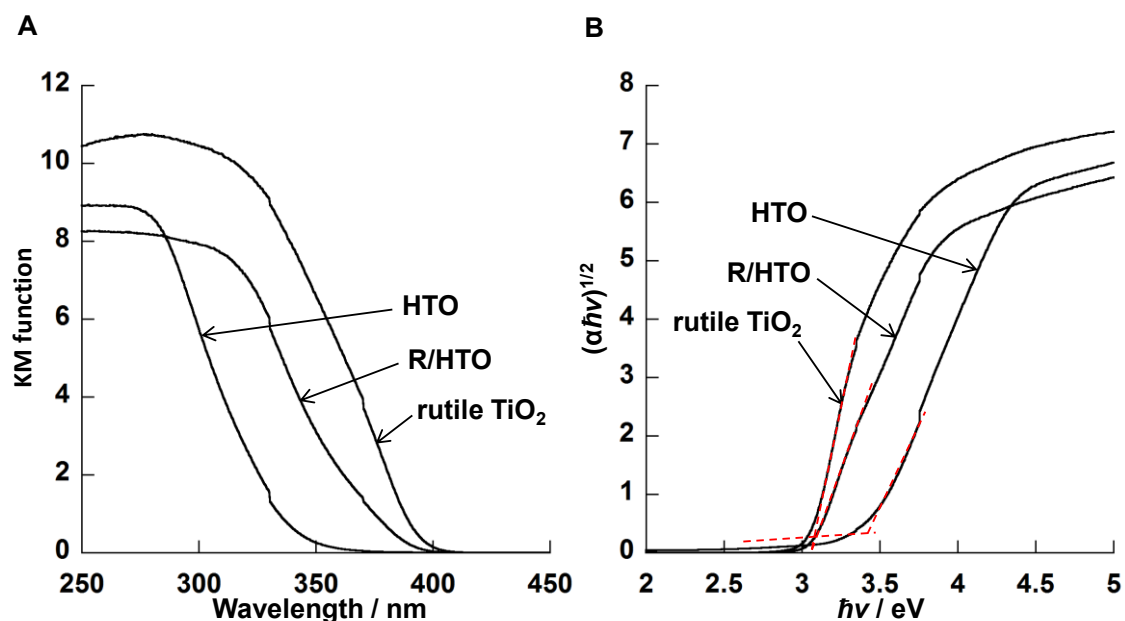
Figure 4-15. (A) Diffused-reflectance UV-vis spectra and (B) Tauc plots of HTO, rutile and R/HTO.

The photocatalytic activity of R/HTO was evaluated by H_2 evolution from an aqueous methanol solution[45] under simulated solar light (>300 nm). As shown in Figure 4-16, the photocatalytic activity of R/HTO was about four times higher than that of HTO, although rutile (JRC-TIO-6) was inactive under identical conditions. This indicates the synergy effects of the co-presence of HTO phase and surface rutile nanoparticles. As shown in Figure 4-17, AQY on R/HTO for H_2 evolution from an aqueous methanol solution correlates well with the photoabsorption of R/HTO, indicating that the photocatalytic activity of R/HTO in the >370 nm region (up to 408 nm), can be accounted for by the sensitization effect of rutile, since HTO cannot absorb light in this region. This is thermodynamically favorable, because the conduction band potentials (E_{CB}) of rutile and HTO are almost identical (the E_{CB} of rutile is 0.05 eV higher than that of HTO) according to the previous reports (Figure 4-18).[55,56] Considering that hole transfer from P25, whose main component is anatase, to HTO did not occur in our previous report,[57] hole transfer from rutile, whose valence band potential is more negative than that of anatase, to HTO and subsequent enhanced charge separation can be ruled out. As shown in Figure 4-19, H_2 was continuously evolved on

R/HTO even 24 h after the start of irradiation, a result further supportting the formation of HTO-rutile heterojunction.
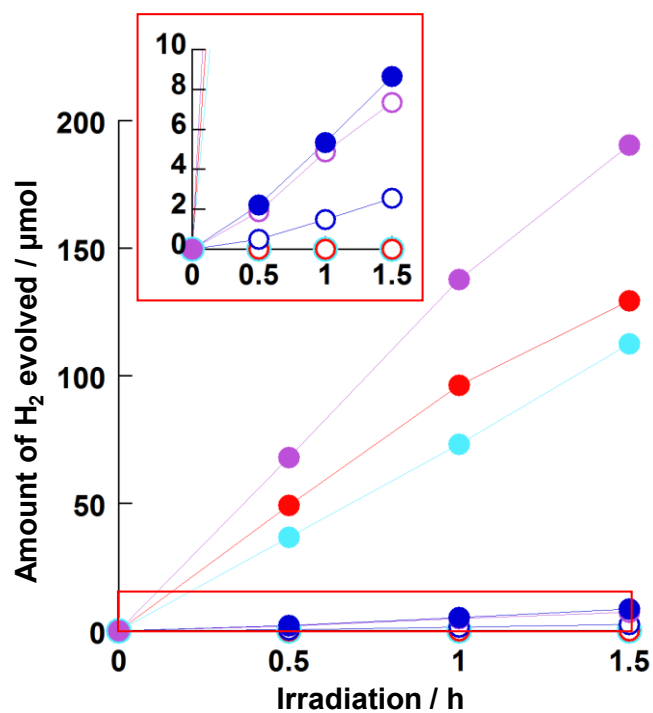
Figure 4-16. The time courses of H_2 evolution from an aqueous methanol solution on R/HTO (purple), HTO (blue), rutile (light blue) and P25 (red). Open and filled circles represent before and after Pt lording, respectively. Inset shows the expanded graph.
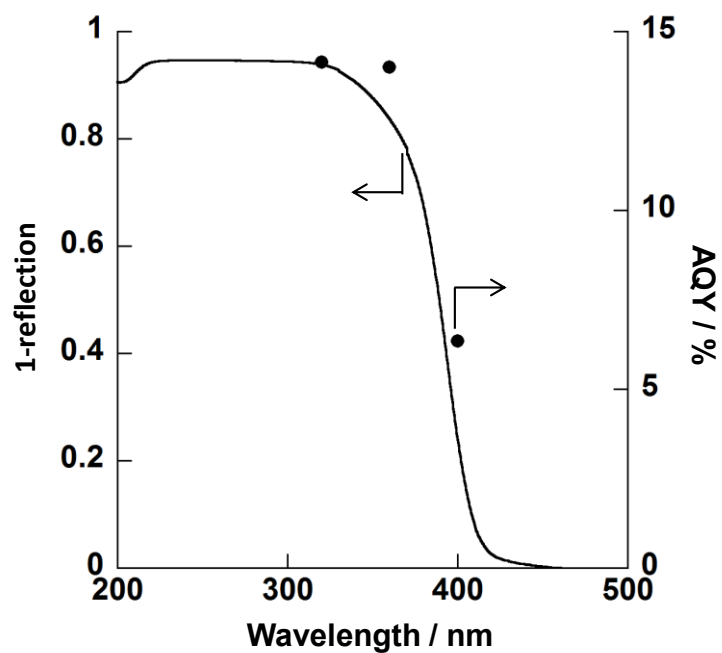
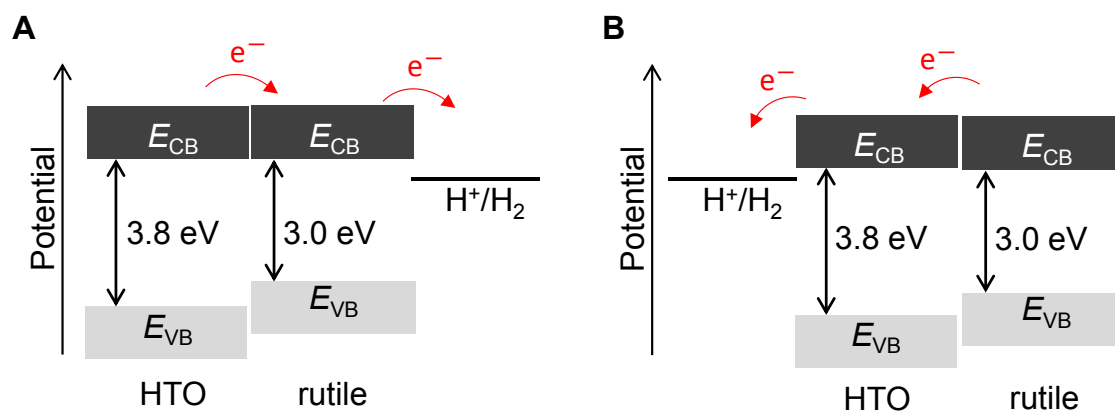**Figure 4-17.** The action spectrum in H_2 evolution from an aqueous methanol solution of R/HTO.

Figure 4-18. Energy diagrams and schemes for electron transfer between HTO phase and rutile in R/HTO under (A) λ < 370 nm and (B) λ > 370 nm light irradiation.
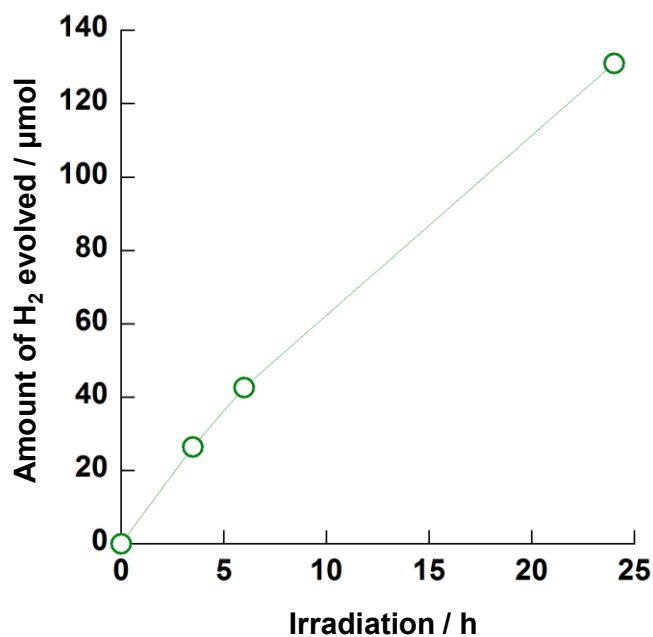
Figure 4-19. The time course of H_2 evolution from an aqueous methanol solution on R/HTO for long-term.

Given that the AQY of R/HTO at 320 nm was 14.1% (Figure 4-17) while those of HTO and rutile were 4.2% and 0% (data not shown), respectively, the possibility of enhanced photocatalytic activity of HTO phase in the < 370 nm region should be considered as another possible factor contributing to the high activity under simulated solar light. It is generally known that electron transfer from an excited TiO_2 particle to a neighboring one through their heterojunction can suppress charge recombination, enhancing the photocatalytic activity. Since electron transfer from HTO phase to rutile is also thermodynamically favorable, as mentioned above, enhanced charge separation at the HTO-rutile heterojunction can be a factor in the enhanced photocatalytic activity of HTO phase in the < 370 nm region.

Since the benchmark photocatalyst for this reaction is Pt-loaded P25 TiO_2 (Pt@P25),[43] Pt-loaded R/HTO (Pt@R/HTO) (0.5 wt% Pt loading) was prepared. The photocatalytic activity of Pt@R/HTO was considerably higher than that of Pt@HTO and Pt@rutile, indicating that the synergy effects of the co-presence of HTO phase and rutile were maintained after Pt-loading. The photocatalytic activity of Pt@R/HTO, which exhibits 5000 % activity of HTO, was 150 % of the benchmark Pt@P25.

Since the specific surface area of R/HTO (51 m^2 g^{-1}) was almost identical to that of P25 (50 m^2 g^{-1}) (Figure 4-20), the mechanism of the high photocatalytic activity of Pt@R/HTO is not attributable to the accessibility of a reactive substrate to the photocatalyst surface. The higher photocatalytic activity of Pt@R/HTO compared to that of Pt@P25 is ascribable to two factors: First, pure HTO shows higher photocatalytic activity than P25 (P25 shows hardly any photocatalytic H$_2$ evolution activity),[43] possibly due to the fact that the conduction band potential of HTO is more negative than that of anatase,[55,56] which is the main component of P25: and second, electron transfer between HTO phase and rutile in R/HTO is more effective than that between anatase and rutile in P25, possibly because of their similar conduction band potential. The photocatalytic activity of the present Pt@R/HTO was significantly higher than benchmark Pt@P25.[43]
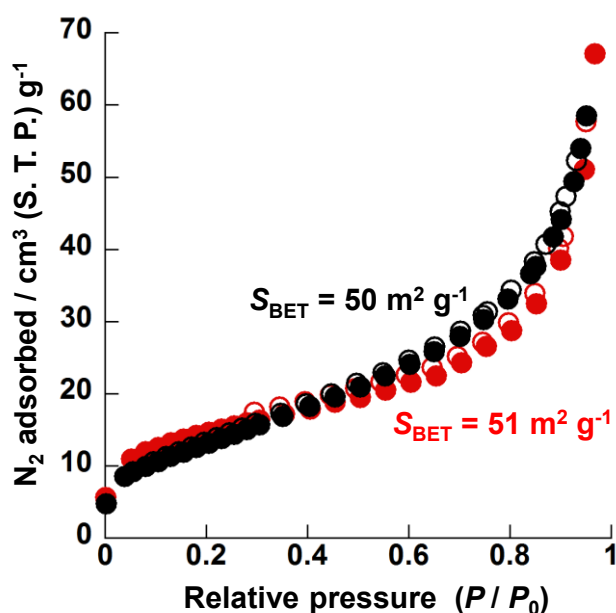
Figure 4-20. N$_2$ adsorption (open)/desorption (filled) isotherms of P25 (black) and R/HTO (red). Values in the graph are the BET surface areas of the samples.

4-4. Conclusions

A methodology for the creation of protonated layered titanate-rutile heterojunctions on the outer particle surface of protonated layered tiatanate by treating layered potassium titanate with HCl and drying it at room temperature under reduced pressure was proposed. The photocatalytic activity of this protonated layered

titanate/rutile composite with heterojunctions after Pt-loading for H_2 evolution from water containing methanol as a sacrifice agent under simulated solar light was 150 % of Pt-loaded P25 TiO_2, a benchmark photocatalyst. This unprecedentedly high activity resulted from the enhanced activity of the protonated layered titanate due to efficient charge separation at the protonated layered titanate-rutile heterojunction in addition to the sensitization effects of rutile, which absorbs light with longer wavelengths compared to protonated layered titanate. This methodology could be a breakthrough in the creation of high-performance heterojunctions under mild conditions by optimizing such experimental conditions as the acid solution concentration and temperature during acid treatment.

4-5. References

[1]   Fujishima, A.; Zhang, X.; Tryk, D. A. TiO_2 Photocatalysis and Related Surface Phenomena. *Surf. Sci. Rep.* **2008**, *63*, 515–582.

[2]   Chen, X.; Mao, S. S. Titanium Dioxide Nanomaterials : Synthesis , Properties , Modifications , and Applications. *Chem. Rev.* **2007**, *107*, 2891-2959.

[3]   Zhang, Y.; Tang, B.; Wu, Z.; Shi, H.; Zhang, Y.; Zhao, G. Glucose Oxidation over Ultrathin Carbon-Coated Perovskite Modified TiO_2 Nanotube Photonic Crystals with High-Efficiency Electron Generation and Transfer for Photoelectrocatalytic Hydrogen Production. *Green Chem.* **2016**, *3*, 2424–2434.

[4]   Qiu, J.; Zeng, G.; Ha, M.; Ge, M.; Lin, Y.; Hettick, M.; Hou, B.; Alexandrova, A. N.; Javey, A.; Cronin, S. B. Artificial Photosynthesis on TiO_2‑Passivated InP Nanopillars. *Nano Lett.* **2015**, *15*, 6177–6181.

[5]   Won, D.; Lee, J.-S.; Ji, J.-M.; Jung, W.-J.; Son, H.-J.; Pac, C.; Kang, S.-O. Highly Robust Hybrid Photocatalyst for Carbon Dioxide Reduction: Tuning and Optimization of Catalytic Activities of Dye/TiO_2/Re(I) Organic−Inorganic Ternary Systems. *J. Am. Chem. Soc.* **2015**, *137*, 13679-13690.

[6]   Li, G.; Richter, C. P.; Milot, R. L.; Cai, L.; Schmuttenmaer, C. A.; Crabtree, R. H.; Rrudvig, G. W.; Batista, V. S. Synergistic Effect between Anatase and Rutile TiO_2 Nanoparticles in Dye-synsitized Solar Cells. *Dalton Trans.* **2009**, *45*, 10078-10085.

[7]   Ye, M.; Zheng, D.; Lv, M.; Chen, C.; Lin, C.; Lin, Z. Hierarchically Structured Nanotubes for Highly Efficient Dye-Sensitized Solar Cells. *Adv. Mater.* **2013**, *25*, 3039–3044.

[8]   He, H.; Liu, C.; Dubois, K. D.; Jin, T.; Louis, M. E.; Li, G. Enhanced Charge Separation in Nanostructured TiO_2 Materials for Photocatalytic and Photovoltaic Applications. *Ind. Eng. Chem. Res.* **2012**, *51*, 11841−11849.

[9]   Mali, S. S.; Kim, H.; Shim, C. S.; Patil, P. S.; Kim, J. H.; Hong, C. K. Surfactant Free Most Probable TiO_2 Nanostructures via Hydrothermal and Its Dye Sensitized Solar Cell Properties. *Sci. Rep.* **2013**, *3*, 3004.

[10]   Zhang, J.; Bang, J. H.; Tang, C.; Kamat, P. V. Tailored TiO_2-$SrTiO_3$ Heterostructure Nanotube Arrays for Improved Photoelectrochemical Performance. *ACS Nano* **2010**, *4*, 387–395.

[11]   Zhu, F.; Dong, H.; Wang, Y.; Wu, D.; Li, J.; Pan, J.; Li, Q.; Ai, X.; Zhang, J.; Xu, D. Dual-Functional Hetero-Structured TiO_2 Nanotrees Composed of Rutile Trunks and Anatase Branches for Improved Performance of Quantum Dot-Sensitized Solar Cells. *Phys. Chem. Chem. Phys.* **2013**, *15*, 17798–17803.

[12]   Hurum, D. C.; Agrios, A. G.; Gray, K. A.; Rajh, T.; Thurnauer, M. C. Explaining the Enhanced Photocatalytic Activity of Degussa P25 Mixed-Phase TiO_2 Using EPR. *J. Phys. Chem. B* **2003**, *107*, 4545–4549.

[13]   Kawahara, T.; Konishi, Y.; Tada, H.; Tohge, N.; Nishii, J.; Ito, S. A Patterned TiO_2 (Anatase)/TiO_2 (Rutile) Bilayer-Type Photocatalyst: Effect of the Anatase/Rutile Junction on the Photocatalytic Activity. *Angew. Chem., Int. Ed.* **2002**, *41*, 2811–2813.

[14]   Zhang, J.; Xu, Q.; Feng, Z.; Li, M.; Li, C. Importance of the Relationship between Surface Phases and Photocatalytic Activity of TiO_2. *Angew. Chem., Int. Ed.* **2008**, *47*, 1766–1769.

[15]   Ide, Y.; Inami, N.; Hattori, H.; Saito, K.; Sohmiya, M.; Tsunoji, N.; Komaguchi, K.; Sano, T.; Bando, Y.; Golberg, D.; Sugahara, Y. Remarkable Charge Separation and Photocatalytic Efficiency Enhancement through Interconnection of TiO_2 Nanoparticles by Hydrothermal Treatment. *Angew. Chem., Int. Ed.* **2016**, *55*, 3600–3605.

[16] Bickmore, C. R.; Waldner, K. F.; Baranwal, R.; Hinklin, T.; Treadwell, D. R.; Laine, R. M. Ultrafine Titania by Flame Spray Pyrolysis of a Titanatrane Complex. *J. Eur. Ceram. Soc.* **1998**, *18*, 287–297.

[17] Choy, J. H. Intercalative Route to Heterostructured Nanohybrid. *J. Phys. Chem. Solids* **2004**, *65*, 373–383.

[18] Gunjakar, J. L.; Kim, I. Y.; Lee, J. M.; Jo, Y. K.; Hwang, S.-J. Exploration of Nanostructured Functional Materials Based on Hybridization of Inorganic 2D Nanosheets. *J. Phys. Chem. C* **2014**, *118*, 3847–3863.

[19] Ide, Y.; Sadakane, M.; Sano, T.; Ogawa, M. Functionalization of Layered Titanates. *J. Nanosci. Nanotechnol.* **2014**, *14*, 2135–2147.

[20] Okada, T.; Ide, Y.; Ogawa, M. Organic-Inorganic Hybrids Based on Ultrathin Oxide Layers: Designed Nanostructures for Molecular Recognition. *Asian J. Chem.* **2012**, *7*, 1980–1992.

[21] Ma, R.; Sasaki, T.; Bando, Y. Layer-by-Layer Assembled Multilayer Films of Titanate Nanotubes, Ag- or Au-Loaded Nanotubes, and Nanotubes/Nanosheets with Polycations. *J. Am. Chem. Soc.* **2004**, *126*, 10382–10388.

[22] Xiong, Z.; Zhao, X. S. Nitrogen-Doped Titanate-Anatase Core-Shell Nanobelts with Exposed {101} Anatase Facets and Enhanced Visible Light Photocatalytic Activity. *J. Am. Chem. Soc.* **2012**, *134*, 5754–5757.

[23] Xiong, Z.; Zhao, X. S. Titanate@TiO$_2$ Core-Shell Nanobelts with an Enhanced Photocatalytic Activity. *J. Mater. Chem. A* **2013**, *1*, 7738–7744.

[24] Choy, J.-H.; Lee, H.-C.; Jung, H.; Kim, H.; Boo, H. Exfoliation and Restacking Route to Anatase-Layered Titanate Nanohybrid with Enhanced Photocatalytic Activity. *Chem. Mater.* **2002**, *14*, 2486-2491.

[25] Paek, S. M.; Jung, H.; Lee, Y.-J.; Park, M.; Hwang, S.-J.; Choy, J.-H. Exfoliation and Reassembling Route to Mesoporous Titania Nanohybrids. *Chem. Mater.* **2006**, *18*, 1134–1140.

[26] Kudo, A.; Tanaka, A.; Domen, K.; Maruya, K.; Aika, K.; Onishi, T. Photocatalytic Decomposition of Water over NiO-K$_4$Nb$_6$O$_{17}$ Catalyst. *J. Catal.* **1988**, *111*, 67-76.

[27] Kim, Y. I.; Salim, S.; Huq, M. J.; Mallouk, T. E. Visible Light Photolysis of Hydrogen Iodide Using Sensitized Layered Semiconductor Particles. *J. Am. Chem. Soc.* **1991**, *113*, 9561-9563.

[28]   Ebina, Y.; Tanaka, A.; Kondo, J. N.; Domen, K. Preparation of Silica Pillared Ca$_2$Nb$_3$O$_{10}$ and Its Photocatalytic Activity. *Chem. Mater.* **1996**, *8*, 2534–2538.

[29]   Compton, O. C.; Carroll, E. C.; Kim, J. Y.; Larsen, D. S.; Osterloh, F. E. Calcium Niobate Semiconductor Nanosheets as Catalysts for Photochemical Hydrogen Evolution from Water. *J. Phys. Chem. C* **2007**, *111*, 14589–14592.

[30]   Okamoto, Y.; Ida, S.; Hyodo, J.; Hagiwara, H.; Ishihara, T. Synthesis and Photocatalytic Activity of Rhodium-Doped Calcium Niobate Nanosheets for Hydrogen Production from a Water/Methanol System without Cocatalyst Loading. *J. Am. Chem. Soc.* **2011**, *133*, 18034–18037.

[31]   Miyamoto, N.; Kuroda, K.; Ogawa, M. Visible Light Induced Electron Transfer and Long-Lived Charge Separated State in Cyanine Dye/Layered Titanate Intercalation Compounds. *J. Phys. Chem. B* **2004**, *108*, 4268–4274.

[32]   Sasaki, T.; Watanabe, M.; Michiue, Y.; Komatsu, Y.; Izumi, F.; Takenouchi, S. Preparation and Acid-Base Properties of a Protonated Titanate with the Lepidocrocite-like Layer Structure. *Chem. Mater.* **1995**, *7*, 1001–1007.

[33]   Li, Y.; Lee, N.-H.: Hwang, D.-S.; Song, J.-S.; Lee, E. G.; Kim, S.-J. Synthesis and Characterization of Nano Titania Powder with High Photoactivity for Gas-Phase Photo-Oxidation of Benzene from TiOCl$_2$ Aqueous Solution at Low Temperatures. *Langmuir* **2004**, *20*, 10838-10844.

[34]   Gopal, M.; Chan, W. J. M.; Jonghe, L. C. D. Room Temperature Synthesis of Crystalline Metal Oxides. *J. Mater. Sci.* **1997**, *32*, 6001-6008.

[35]   Yang, S.; Liu, Y.; Guo, Y.; Zhao, J.; Xu, H.; Wang, Z. Preparation of Rutile Titania Crystals by Liquid Method at Room Temperature. *Mater. Chem. Phys.* **2003**, *77*, 501-506.

[36]   Zhang, X.; Zheng, X.; Cheng, Y.; Li, G. H.; Chen, X. P.; Formation of Rutile Fasciculate Zone Induced by Sunlight Irradiation at Room Temperature and Its Hemocompatibility. *Mater. Sci. Eng. C* **2013**, *33*, 3289-3293.

[37]   Egami, T.; Billinge, S. J. L. Underneath the Bragg Peaks: Structural Analysis of Complex Materials, Elsevier, Oxford, UK, 2003.

[38]   Tominaka, S.; Yoshikawa, H.; Matsushita, Y.; Cheetham, A. K. Topotactic Reduction of Oxide Nanomaterials: Unique Structure and Electronic Properties of Reduced TiO$_2$ Nanoparticles. *Mater. Horiz.* **2014**, *1*, 106.

[39] Farrow, C. L.; Juhas, P.; Liu, J. W.; Bryndin, D.; Božin, E. S.; Bloch, J.; Proffen, T.; Billinge, S. J. L. PDFfit2 and PDFgui: Computer Programs for Studying Nanostructure in Crystals. *J. Phys. Condens. Matter.* **2007**, *19*, 335219.

[40] Ogawa, M.; Morita, M.; Igarashi, S.; Sato, S. A Green Synthesis of a Layered Titanate, Potassium Lithium Titanate; Lower Temperature Solid-State Reaction and Improved Materials Performance. *J. Solid State Chem.* **2013**, *206*, 9–13.

[41] Izawa, H.; Kikkawa, S.; Koizumi, M. Ion Exchange and Dehydration of Layered Titanate, $Na_2Ti_3O_7$ and $K_2Ti_4O_9$. *J. Phys. Chem.* **1982**, *86*, 5023–5026.

[42] Sasaki, T.; Kooli, F.; Iida, M.; Michiue, Y.; Takenouchi, S.; Yajima, Y.; Izumi, F.; Chakoumakos, B. C.; Watanabe, M. A Mixed Alkali Metal Titanate with the Lepidocrocite-like Layered Structure. Preparation, Crystal Structure, Protonic Form, and Acid-Base Intercalation Properties. *Chem. Mater.* **1998**, *10*, 4123–4128.

[43] Amano, F.; Prieto-Mahaney, O. O.; Terada, Y.; Yasumoto, T.; Shibayama, T.; Ohtani, B. Decahedral Single-Crystalline Particles of Anatase titanium(IV) Oxide with High Photocatalytic Activity. *Chem. Mater.* **2009**, *21*, 2601–2603.

[44] Ohtani, B.; Prieto-Mahaney, O. O.; Li, D.; Abe, R. What Is Degussa (Evonic) P25 ? Crystalline Composition Analysis, Reconstruction from Isolated Pure Particles and Photocatalytic Activity Test. *J. Photochem. Photobiol., A* **2010**, *216*, 179–182.

[45] Kudo, A.; Miseki, Y. Heterogeneous Photocatalyst Materials for Water Splitting. *Chem. Soc. Rev.* **2009**, *38*, 253–278.

[46] Gao, T.; Fjellvåg, H.; Norby, P. Raman Scattering Properties of a Protonic Titanate $H_xTi_{2-x/4}\square_{x/4}O_4.H_2O$ ($\square$, Vacancy; x=0.7) with Lepidocrocite-Type Layered Structure. *J. Phys. Chem. B* **2008**, *112*, 9400–9405.

[47] Zhang, J.; Li, M.; Feng, Z.; Chen, J.; Li, C. UV Raman Spectroscopic Study on TiO_2. I. Phase Transformation at the Surface and in the Bulk. *J. Phys. Chem. B* **2006**, *110*, 927–935.

[48] Morris, R. E.; Čejka, J. Exploiting Chemically Selective Weakness in Solids as a Route to New Porous Materials. *Nat. Chem.* **2015**, *7*, 381–388.

[49] Cundy, C. S.; Cox, P. A. The Hydrothermal Synthesis of Zeolites : History and Development from the Earliest Days to the Present Time. *Chem. Rev.* **2003**, *103*, 663–702.

[50] Roth, W. J.; Nachtigall, P.; Morris, R. E.; Wheatley, P. S.; Seymour, V. R.; Ashbrook, S. E.; Chlubná, P.; Grajciar, L.; Položij, M.; Zukal, A.; Shvets, O.; Čejka, J. A Family of Zeolites with Controlled Pore Size Prepared Using a Top-down Method. *Nat. Chem.* **2013**, *5*, 628–633.

[51] Subotic, B.; Skrtic, D.; Smit, I.; Sekovanic, L. Transformation of Zeolite A into Hydroxysodalite I. An Approach to the Mechanism of Transformation and Its Experimental Evaluation. *J. Cryst. Growth* **1980**, *50*, 498–508.

[52] Jon, H.; Ikawa, N.; Oumi, Y.; Sano, T. An Insight into the Process Involved in Hydrothermal Conversion of FAU to *BEA Zeolite. *Chem. Mater.* **2008**, *20*, 4135–4141.

[53] Honda, K.; Itakuma, M.; Matsuyama, Y.; Onda, A.; Ide, Y.; Sadakane, M.: Sano, T. Role of Structural Similarity Between Starting Zeolite and Product Zeolite in the Interzeolite Conversion Process. *J. Nanosci. Nanotechnol.* **2013**, 13, 3020-3026.

[54] Tauc, J.; Grigorovici, R.; Vancu, A. Optical Properties and Electronic Structure of Amorphous Germanium. *Phys. Status Solidi* **1966**, *15*, 627–637.

[55] Sakai, N.; Ebina, Y.; Takada, K.; Sasaki, T. Electronic Band Structure of Titania Semiconductor Nanosheets Revealed by Electrochemical and Photoelectrochemical Studies. *J. Am. Chem. Soc.* **2004**, *126*, 5851–5858.

[56] Scanlon, D. O.; Dunnill, C. W.; Buckeridge, J.; Shevlin, S. A.; Logsdail, A. J.; Woodley, S. M.; Catlow, C. R. A.; Powell, M. J.; Palgrave, R. G.; Parkin, I. P.; Watson, G. W.; Keal, T. W.; Sherwood, P.; Walsh, A.; Sokol, A. A. Band Alignment of Rutile and Anatase TiO_2. *Nat. Mater.* **2013**, *12*, 798–801.

[57] Saito, K.; Kozeni, M.; Sohmiya, M.; Komaguchi, K.; Ogawa, M.; Sugahara, Y.; Ide, Y. Unprecedentedly Enhanced Solar Photocatalytic Activity of a Layered Titanate Simply Integrated with TiO_2 Nanoparticles. *Phys. Chem. Chem. Phys.* **2016**, *18*, 30920–30925.

CHAPTER 5

Conclusions

5. Conclusions

Facile methodologies for preparing titania-based composites with controlled electronic structures are described in this thesis.

A methodology for preparing TiO_2 co-doped with Nb and N *via* synthesis of Nb-doped TiO_2 by liquid feed flame spray pyrolysis and subsequent NH_3 annealing is proposed. Creation of localized levels between band gap *via* NH_3 annealing was indicated by development of visible light absorption, and the absorbance of visible light increased with the Nb content. Precise control of visible-light absorption may be possible by optimizing the doped Nb content.

A protonated layered titanate-TiO_2 heterojunction was created simply by mixing protonated layered titanate and P25 TiO_2 in water to form a composite. The composite showed enhanced photocatalytic activity, which was ascribable to enhanced charge separation as a result of photoexcited electron transfer from the protonated layered titanate to P25 *via* the created heterojunction.

Rutile TiO_2 was formed from protonated layered titanate on the outer particle surfaces of the protonated layered tiatante to create a heterojunction by treating layered potassium titanate with diluted HCl at room temperature and drying it at room temperature under reduced pressure. As a result of photoexcited electron transfers from rutile to the protonated layered tiatanate and vice versa *via* the heterojunction, charge separation was enhanced, resulting in enhanced photocatalytic activity.

The electronic structures of TiO_2 were controlled by creating localized levels between band gaps *via* doping of TiO_2 nanoparticles with Nb and N to control the light absorption properties of TiO_2, or by creating heterojunctions between protonated layered titante and TiO_2 to enhance the charge-separation efficiency. The methodologies proposed in this thesis are facile compared to the conventional methodologies, and they are expected to be applied for synthesis of pigments or photocatalysts with better performances.

List of Publications

"Room-temperature rutile TiO$_2$ nanoparticle formation on protonated layered titanate for high-performance heterojunction creation.", *ACS Appl. Mater. Interfaces*, in press, <u>K. Saito</u>, S. Tominaka, S. Yoshihara, K. Ohara, Y. Sugahara and Y. Ide.*

"Unprecedentedly enhanced solar photocatalytic activity of a layered titanate simply integrated with TiO$_2$ nanoparticles", *Phys. Chem. Chem. Phys.*, **18**, 30920-30925 (2016)., <u>K. Saito</u>, M. Kozeni, M.Sohmiya, K. Komaguchi, M. Ogawa, Y. Sugahara and Y. Ide.*

"Remarkable charge separation and photocatalytic efficiency enhancement through interconnection of TiO$_2$ nanoparticles by hydrothermal treatment", *Angew. Chem. Int. Ed*, **55**, 3600-3605 (2016)., Y. Ide, N. Inami, H. Hattori, <u>K. Saito</u>, M.Sohmiya, N. Tsunoji, K. Komaguchi, T. Sano, Y. Bando, D. Goldberg and Y. Sugahara.

"h-BN nanosheets as simple and effwective additives to largely enhance the activity of Au/TiO$_2$ plasmonic photocatalysts", *Phys. Chem. Chem. Phys.*, **18**, 79-83 (2016)., Y. Ide, K.Nagao, <u>K. Saito</u>, K. Komaguchi, R. Fuji, A. Kogure, Y. Sugahara, Y. Bando and D. Goldberg.

"Host-guest chemistry of mesoporous silicas; Precise design of location and orientation of molecular guests in mesopore.", *Sci. Technol. Adv. Mater.,* **16**, 054201 (2015)., M. Sohmiya, <u>K. Saito</u> and M. Ogawa.

"Possible roles of the spatial distribution of organic guest species in mesoporous silicas to control the properties of the hybrids", *Eur. J. Inorg. Chem.*, 1126-1136 (2015)., M. Ogawa, <u>K. Saito</u> and M. Sohmiya.

"A controlled spatial distribution of functional units in the two dimensional nanospace of layered silicates and titanates", *Dalton Trans.*, **43**, 10340-10354 (2014)., M. Ogawa,

K. Saito and M. Sohmiya.

*Publication related to this thesis.

Acknowledgements